

Development of Dual Modality
Lanthanide-Doped Magnetite Nanoparticles
For Potential Biomedical Imaging

A Thesis

Presented to the Faculty of the Graduate School of
Western Carolina University in Partial Fulfillment of the
Requirements for the Degree of Master of Science of Chemistry

By

Mickey Lance Clark

Director: Dr. Channa R. De Silva

Assistant Professor, Bioinorganic Chemistry,

Dr. David D. Evanoff

Assistant Professor, Organic Chemistry

Dr. Brian D. Dinkelmeyer

Assistant Professor, Analytical Chemistry

Department of Chemistry and Physics

April 2014

ACKNOWLEDGMENT

I would like to thank the Department of Chemistry and Physics at Western Carolina University (WCU), Cullowhee, NC, 28723, USA for providing me the opportunity to complete my M.S degree thesis work. I am very grateful to my TRAC members Assistant Professor Channa R. De Silva, Assistant Professor David D. Evanoff, and Associate Professor Brain D. Dinklemyer, for their continuous involvement in the project. I realize that it would not be possible to accomplish this project without the efforts of my TRAC committee for their regular support and guidance which helped me to accomplish my M.S. degree successfully and on time. I would like to extend my gratitude to my research advisor, Assistant Professor Channa R. De Silva for his encouragement and willingness to answer my many questions. My thanks to Professor David Butcher, Associate Dean of the College of Arts and Sciences at WCU and Associate Professor Cynthia A. Atterholt, Head of the Department of Chemistry and Physics at WCU. I would like to respectfully thank all the faculty members in the Department of Chemistry and Physics at WCU and thank my friends and family members for their kind cooperation throughout my studies at Western Carolina University.

DEDICATIONS

I would like to dedicate this graduate thesis to my family. My parents, for supporting me and believing that I could accomplish anything I put my mind to. My sisters, for their continued support and helping me to see the project to completion. I would like to thank all of them for putting up with my dull chemistry stories and attitude when research took turns for the worse. I appreciate everything everyone helped me achieve and I love each one of you.

TABLE OF CONTENTS

LIST OF TABLES	iii
LIST OF FIGURES	iv
LIST OF ABBREVIATIONS	vii
ABSTRACT	viii
CHAPTER 1: INTRODUCTION	1
1.1 BACKGROUND	1
1.1.1 Previous Research Involving Magnetic Nanoparticles	1
1.1.2 Previous Research Involving Luminescent Nanoparticles	4
1.1.3 Introduction to Research	6
1.2 PROJECT DESIGN	11
1.2.1 High Temperature-Based Thermal Decomposition	11
1.2.2 Low Temperature-Based Co-Precipitation	14
1.2.3 Core-Shell Nanoparticle Project Design	15
1.2.4 Surface Coating with a Chromophore.....	16
CHAPTER 2: EXPERIMENTAL.....	19
2.1 ALL NANOPARTICLE SYNTHESIS.....	19
2.1.1 Low Temperature Synthesis of Eu(III)-Doped Fe ₃ O ₄ Nanoparticles	19
2.1.2 Synthesis of Eu(btfa) ₃ (H ₂ O) ₂ Precursor Complex	20
2.1.3 High Temperature Synthesis of Eu(III)-Doped Fe ₃ O ₄ Nanoparticles	20
2.1.4 Synthesis of Core-Shell Eu(III) Coated Fe ₃ O ₄ Nanoparticles	22
2.1.5 Surfactant Removal From Eu(III)-Doped Fe ₃ O ₄ Nanoparticles Prepared Using High Temperature Method	23
2.1.6 Surface Coating of Eu(III)-Incorporated Fe ₃ O ₄ Nanoparticles with TTA.....	24
2.2 MATERIALS CHARACTERIZATION	26
2.2.1 FTIR	26
2.2.2 TEM	27
2.2.3 UV-Visible Absorption Spectroscopy	27
2.2.4 Fluorescence Spectroscopy	27
2.2.5 XRD	28
2.2.6 ICP-OES.....	28
CHAPTER 3: RESULTS AND DISCUSSION.....	31
3.1 CO-PRECIPITATION Eu:Fe ₃ O ₄ NANOPARTICLES.....	31
3.1.1 Synthesis and Crystal Lattice Formation	31
3.1.2 Magnetic Behavior of Magnetite Nanoparticles Synthesized Using Co-Precipitation Method.....	33
3.1.3 XRD Studies	34
3.1.4 TEM Studies	37
3.1.5 FT-IR Studies of Co-Precipitation Nanoparticles.....	39
3.1.6 Determining Actual Concentrations of Europium Doping	45
3.2 THERMALLY DECOMPOSED Eu:Fe ₃ O ₄ NANOPARTICLES.....	47

3.2.1	Synthesis and Crystal Lattice Formation	47
3.2.2	X-ray Powder Diffraction Studies	48
3.2.3	TEM Studies	50
3.2.4	FT-IR Characterization of High Temperature Nanoparticles	54
3.2.5	Determining Actual Concentrations of Europium Doping for Thermal Decomposition	63
3.3	CORE-SHELL NANOPARTICLES STRUCTURE AND SYNTHESIS.....	64
3.3.1	Core and Shell Synthesis	64
3.3.2	XRD Characterization of Cores	65
3.3.3	ICP-OES Measurement of Cores	66
3.4	LUMINESCENCE IMPROVEMENT MEASUREMENTS OF ALL SYNTHESIZED NANOPARTICLES	67
3.4.1	UV-Vis Absorption for all Synthesized Nanoparticles.....	67
3.4.2	Fluorescence Spectroscopy for Co-Precipitation Nanoparticles.....	70
3.4.3	Quantum Yield Measurements of Co-Precipitation Nanoparticles	72
3.4.4	Fluorescence Spectroscopy for High Temperature and Core-Shell Nanoparticles	74
3.4.5	Quantum Yield Measurements for High Temperature and Core-Shell Nanoparticles	77
3.5	CONCLUSION.....	77
	REFERENCES	80
	SUPPLEMENTAL INFORMATION	84

LIST OF TABLES

TABLE	PAGE
CHAPTER 2:	
2.1 Varying amounts of TTA to nanoparticle by mass.....	25
2.2 Calibration curve solution concentrations for ICP-OES.....	29
2.3 Initial masses of nanoparticles for ICP-OES measurements	30
CHAPTER 3:	
3.1 Actual levels of europium and iron calculated by ICP-OES	46
3.2 Actual concentration of iron to europium in high temperature nanoparticles	64
3.3 ICP-OES measurements on cores and core-shell nanoparticles	66
3.4 Quantum yields of co-precipitation nanoparticles with various TTA coatings	74
3.5 Quantum yield results for high temperature and core-shell nanoparticles	77

LIST OF FIGURES

FIGURE	PAGE
CHAPTER 1:	
1.1 Schematic of magnetite nanoparticle with “Antenna” system	8
1.2 [A] Acetylacetonate [B] 4,4,4-trifluoro-1-phenyl-2,4-butanedione [C] Eu(btfa) ₃ (H ₂ O) ₂ [D] Fe(acac) ₃	12
1.3 Nanoparticle surface coated with surfactant oleic acid	13
1.4 Schematic illustrating the incoming light transferring from the chromophore to the lanthanide	16
1.5 [A] Structure of organic chromophore TTA [B] TTA surface coordinated To the synthesized nanoparticle	17
1.6 Electronic energy transitions diagram from the ground state of the TTA to europium excited state to the ground state through luminescence.....	18
CHAPTER 2:	
2.1 Reaction setup to remove residual water from reaction mixture.....	21
2.2 Reaction setup for reflux conditions.....	22
CHAPTER 3:	
3.1 TTA coordinated co-precipitation nanoparticles with 8 mg, 16 mg, 32 mg 40 mg, 48 mg, 64 mg, and 90 mg/ 75 mg nanoparticles in solution of 1:1 ethanol/water.....	33
3.2 XRD spectrum of co-precipitation method citric acid coated nanoparticles	35
3.3 XRD spectrum of co-precipitation NPs after recrystallization attempt	36
3.4 TEM image of 16:84 co-precipitation NPs surface coated with citric acid.....	37
3.5 Size distribution of 16:84 co-precipitation nanoparticles	38
3.6 TEM image of 20:80 co-precipitation NPs surface coated with citric acid.....	39
3.7 [A] FT-IR spectra of starting reagents and co-precipitation nanoparticles.....	40
3.7 [B] 600 cm ⁻¹ – 1800 cm ⁻¹ region of FT-IR spectrum of starting reagents and co-precipitated nanoparticles	41
3.7 [C] 1800 cm ⁻¹ – 4000 cm ⁻¹ region of FT-IR spectrum of starting reagents and co-precipitated nanoparticles	42
3.8 [A] FT-IR spectra of free TTA and TTA coordinated nanoparticles.....	43
3.8 [B] 600 cm ⁻¹ – 1800 cm ⁻¹ region of FT-IR spectra of free TTA and TTA coordinated nanoparticles	44
3.8 [C] 1800 cm ⁻¹ – 4000 cm ⁻¹ region of FT-IR spectra of free TTA and TTA coordinated nanoparticles	45
3.9 Bar graph of actual europium and iron concentrations versus theoretical doping percentage	46
3.10 XRD diffraction pattern for 16:84 high temperature nanoparticles.....	49
3.11 XRD diffraction pattern for 40:60 high temperature nanoparticles.....	50
3.12 TEM image of 16:84 high temperature nanoparticles	51
3.13 16:84 high temperature nanoparticle size distribution calculated from TEM image	51

3.14 16:84 high temperature nanoparticles crystal lattice lines	52
3.15 TEM image of 40:60 high temperature nanoparticles	53
3.16 40:60 high temperature nanoparticle size distribution.....	53
3.17 [A] FT-IR spectra of oleic acid, surfactant coated nanoparticles, and surfactant free nanoparticles	54
3.17 [B] 600 cm ⁻¹ – 1800 cm ⁻¹ region of FT-IR spectra of oleic acid, surfactant coated nanoparticles, and surfactant free nanoparticles.....	55
3.17 [C] 1800 cm ⁻¹ – 4000 cm ⁻¹ region of FT-IR spectra of oleic acid, surfactant coated nanoparticles, and surfactant free nanoparticles.....	56
3.18 [A] FT-IR spectrum of Eu(btfa) ₃ (H ₂ O) ₂	57
3.18 [B] 600 cm ⁻¹ – 1800 cm ⁻¹ region of FT-IR spectra of Eu(btfa) ₃ (H ₂ O) ₂	58
3.19 [A] FT-IR spectra of surfactant removal during acidic solution treatments	59
3.19 [B] FT-IR subtracted spectra of surfactant removal during acidic solution treatments	60
3.20 [A] FT-IR spectra of TTA and TTA coated high temperature nanoparticles	62
3.20 [B] 400 cm ⁻¹ – 1800 cm ⁻¹ region of FT-IR spectra of TTA and TTA coated high temperature nanoparticles	63
3.21 XRD diffraction pattern of magnetic cores.....	65
3.22 UV-Vis absorption for citric acid and TTA coated co-precipitation nanoparticles	67
3.23 UV-Vis absorption spectrum of TTA	69
3.24 UV-Vis absorption of oleic acid and TTA coated high temperature nanoparticles	69
3.25 UV-Vis absorption spectrum of core-shell nanoparticles coordinated with TTA.....	70
3.26 Luminescence spectrum of 40:60 co-precipitation nanoparticles.....	71
3.27 Luminescence spectra of all co-precipitated nanoparticles	72
3.28 Luminescent intensities as a comparison of TTA coating amounts and europium doping	73
3.29 Luminescent intensities of 16:84 and 40:60 high temperature nanoparticles	75
3.30 Luminescent spectrum of core-shell nanoparticles.....	76

SUPPLEMENTAL:

S1 A-B. XRD spectra of co-precipitated nanoparticles [A] 40:60 [B] 20:80.....	91
S2 A-D. TEM images of co-precipitated nanoparticles 16:84 [A] [B] and 20:80 [C] [D].....	91
S3 A-D. FT-IR spectra of co-precipitation nanoparticles coated with citric acid [A] 16:84 [B] 20:80 [C] 30:70 [D] 40:60.....	92
S4 A-C. FT-IR spectra of TTA coated co-precipitated nanoparticles [A] 16:84 [B] 20:80 [C] 30:70 [D] 40:60.....	92
S5 A-B. TEM images of high temperature 16:84 nanoparticles.....	93
S6 A-B. FT-IR spectra of TTA coated high temperature nanoparticles [A] 16:84 [B] 40:60	93

S7 A-B XRD spectra of high temperature nanoparticles [A] 16:84	
[B] 40:60	93
S8 XRD spectrum of second magnetite cores.....	94
S9 A-D. UV-Vis absorption spectra of co-precipitation nanoparticles [A] 16:84	
[B] 20:80 [C] 30:70 [D] 40:60	94
S10 A-B. UV-Vis absorption spectra of high temperature nanoparticles [A] 16:84	
[B] 40:60	95
S11 A-D. UV-Vis absorption spectra of co-precipitated nanoparticles [A] 16:84	
[B] 20:80 [C] 30:70 [D] 40:60	95
S12 A-B. UV-Vis absorption spectra of high temperature nanoparticles [A] 16:84	
[B] 40:60	96
S13 A-D. Luminescence spectra of co-precipitation nanoparticles [A] 40:60	
[B] 30:70 [C] 20:80 [D] 16:84	96

LIST OF ABBREVIATIONS

acac - acetylacetonate

TTA - thenoyltrifluoroacetone

btfa - 4,4,4-trifluoro-1-phenyl-1,3-butanedione

XRD - X-ray powder diffraction

TEM - transmission electron microscope

FT-IR - Fourier transmission infrared

ICP-OES - inductively coupled plasma – optical emission spectroscopy

ABSTRACT

DEVELOPMENT OF DUAL MODALITY LANTHANIDE-DOPED MAGNETITE NANOPARTICLES FOR POTENTIAL BIOMEDICAL IMAGING

Mickey Lance Clark, M.S.

Western Carolina University (April 2014)

Director: Dr. Channa R. De Silva

In recent years, the application of iron oxide nanoparticles for a myriad of research fields has opened many new avenues for possible biomedical applications. The potential to combine the paramagnetic property of iron oxide nanoparticles with the luminescence properties of a lanthanide metal would be an important development in the biomedical imaging of tumors. With the ability to intravenously administer dual functionality nanoparticles such as these, a medical team could have both a magnetic resonance image, (MRI), due to the T_2 relaxation of magnetite, along with a fluorescent image through the use of laparoscopic techniques. Both images could then be overlaid to give a more comprehensive and accurate understanding of the affected biological area during surgery or treatment.

The purpose of this research was to develop super-paramagnetic magnetite nanoparticles incorporated with a lanthanide metal ion to create dual functionality nanoparticles possessing both paramagnetic properties and monochromatic luminescent properties. The nanoparticles were synthesized using a high temperature-based thermal decomposition method or a low temperature-based co-precipitation method. Once the nanoparticles were synthesized, they were made available for coordination with an organic

chromophore to provide the means for luminescence. A chromophore's, or sensitizer's purpose is to perform ligand-to-metal energy transfer. For europium, coordinated with the chromophore chosen this light is a bright red, with a wavelength of 614 nm. To optimize the ratio of iron oxide to europium, various theoretical europium doping values for the magnetite nanoparticle were tested. The amount of surface coordination with the chromophore was also tested with each incorporation percentage to determine the optimal light emission for each variance.

A third method was developed for synthesizing magnetite nanoparticles. In this case, making core-shell, magnetite cores with a europium shell, nanoparticles. The purpose was to compare europium-doped iron oxide nanoparticles with those surface coated with europium. The same chromophore employed for the europium doped nanoparticles was again used to provide a means for luminescence.

Theoretical doping levels of europium to iron oxide for this project were 16:84, 20:80, 30:70, and 40:60 europium to iron oxide for each doped nanoparticle synthesis. The thermal decomposition method being the most efficient at doping with values for theoretical 40:60 europium to iron oxide, and actual doping was found to be 39.56:60.44. Varying amounts of TTA [thenoyltrifluoroactonate] for surface coordination will vary from 16 mg TTA/ 75 mg nanoparticles. This research found low quantum yields for all synthesized nanoparticles, with the highest quantum yield value of 1.8 ± 0.013 %.

CHAPTER 1

INTRODUCTION

1.1 BACKGROUND

1.1.1 Previous Research Involving Magnetic Nanoparticles

Nanoparticles have been a steady source of research and development for the last forty years or more. Long before this time, nanoparticles have found uses in such capacities as art. Even today, art galleries and events host displays of paramagnetic ferrofluids being used in free flowing sculpture and design, moving under the influence of electromagnetic control. In recent history however, the purpose of the nanoparticle has shifted to a more industrial, medical, or research driven field.

Iron oxide nanoparticles in particular have received much attention for their paramagnetic properties. In industry, magnetorheological fluids, or smart fluids, use micron sized ferrous materials in such items as dampers, brakes, and clutches¹. These micron particles, dispersed in oil, are subjected to a magnetic field to cause an increase in the viscosity of the substance to restrict the movement of the mechanical device. In a strong enough magnetic field the magnetorheological fluid might act as a solid to restrict movement entirely¹.

Another example of nanoparticles in industry come from their use in heat sinks. For certain electronic devices a means for removing heat from the electrical components is needed. Often the heat sink cannot be solid due to possibly interfering with the device's functions. Ferrofluids, which consist of ferrous nanoparticles, work well in this instance for electronic heat sinks. Non paramagnetic liquids could not work due to the risk of spilling out from the area in which they were in place to remove heat. Ferrofluids are held

in place with a strong magnet, removing heat without the risk of spilling or interfering with operations. One such practical example is with a loud speaker. The coil used in a speaker collects heat through continued use and the ferrofluid in place around the loud speaker coil helps to counter this effect, acting as the heat sink¹.

Moving from industrial uses with iron oxide nanoparticles to a more biomedical role is the work being done involving both MRI contrasting agents, and as a treatment course for hypothermia victims¹. Injecting iron oxide nanoparticles into a localized part of the body affected by hypothermia, the area can then be subjected to electromagnetic energy. Ferrofluids absorb electromagnetic energy at a different frequency than water, causing the iron oxide nanoparticles to vibrate and heat the surrounding area while having little effect on the rest of the body. This allows a medical team to heat the area of the body affected by hypothermia, warming the area and preventing further damage. This same technique has been employed to heat tumors in the body, and has been shown to be an effective method to treat cancerous tumors in human beings. The vibrational energy of the iron oxide nanoparticles is transferred to the body as heat and destroyed the tumor, leaving the patient unaffected otherwise¹.

As a diagnostic instrument, MRI is one of the most powerful tools used today in modern medicine. For use in MRI's, the iron oxide nanoparticles function as contrasting agents. The iron oxide nanoparticles, when biocompatible and absorbed by the affected or desired tissue, have different T_2 , weighted relaxation times in different materials. This T_2 signal is a spin-spin or transverse relaxation which involves transfer of energy among the precessing protons which creates an image. Different tissues also take up these nanoparticles in varying amounts, causing different images from various parts of the body.

Iron oxide nanoparticles can also be moved to the desired part of the body under the influence of the strong magnet employed by MRI.

Iron oxide nanoparticles serve a wide variety of roles today in both industry and the biomedical field as magnetic resonance imaging (MRI), solar cell, and heterogeneous catalytic agents². Examples of their uses can be seen on a daily basis. With a suitable biocompatible surface coating and consistent shape and size distribution, important for Förster energy transfer throughout by the chromophore, iron oxide nanoparticles can serve such functions as enhanced MRI contrasting agents. Through a synthesis process developed to control the dimensions of the nanoparticles, these iron oxide nanoparticles can be administered intravenously and used as biological labels or probes².

Magnetite nanoparticles are a form of iron oxide nanoparticle, and the most commonly used for research involving iron oxide nanoparticles. Magnetite forms a mixed valency complex of Fe_3O_4 , ($\text{Fe}^{2+}\text{Fe}_2^{3+}\text{O}_4$). Occurring naturally, this mineral forms based on iron content and partial pressure of oxygen in the environment during its crystallization. Depending on the amount of partial pressure due to oxygen and temperature, iron oxide can form three basic naturally occurring crystals, wüstite, magnetite, and hematite³. Magnetite forms an $\text{Fd}\bar{3}\text{m}$ crystal lattice structure, which is a face-centered cubic lattice system. For every cubic lattice formed there are 8 Fe_3O_4 units per unit cell, this results in 24 Fe and 32 O for each unit cell⁴. The unpaired electrons associated with these valencies of iron, and from unpaired electrons in oxygen, causes the paramagnetic properties associated with magnetite. In the presence of a strong magnetic field these unpaired electrons align with magnetic field of the magnet to create their own magnetic moment. This event is desirable for their use in industry and research. The formation of hematite,

Fe_2O_3 , is not favorable as it lacks this mixed valency present in magnetite and is less paramagnetic than magnetite. At room temperature, magnetite is in a state of oxidation equilibrium with a logarithmic partial pressure of oxygen between negative eighty and negative seventy⁴. Anything above this partial pressure of oxygen promotes the oxidation state of hematite. It is important during synthesis and storage of magnetite nanoparticles to keep them in an inert, reduced oxygen environment.

1.1.2 Previous Research Involving Luminescent Nanoparticles

Luminescent nanoparticles have applications as a means of bio-detection in fluorescence immunoassays, DNA detection, and bio-imaging. The use of a luminescent lanthanide complex is ideal for bio-imaging due to their long luminescence lifetimes, large Stokes shifts, and narrow-line emission⁵. Lanthanide containing nanoparticles are well suited for bio-detection due to their biocompatibility, photostability, and high sensitivity. Typically, they have larger quantum yields and possess a greater tolerance for photobleaching than organic dyes⁶. Another advantage of using lanthanide complexes as bio-imaging probes is that the interference of short-lived background fluorescence from biological tissue, along with light scattering from the instrument on the luminescence imaging is so small that an enhanced signal-to-noise ratio is obtained⁵.

A disadvantage of using lanthanide complexes as luminescent complexes is that they often are excited by ultraviolet light, which can damage biological samples and has a short penetration depth. To avoid this problem it is important to synthesize a lanthanide complex that responds to longer wavelengths of light, preferably within the visible spectrum of light. Developing lanthanide complexes for use in bio-detection relies on a long excitation wavelength⁵.

In an article published by Richard Tang and Xuli Feng the advantages are discussed of luminescent water soluble polymer nanoparticles for bio-imaging and drug delivery⁶. In their study, they found that initial research involving quantum dots to be a source of cytotoxicity due to metal ion leakage. Synthesizing core-shell nanoparticles retained the advantages of quantum dots used as imaging probes while removing the risks. Through encapsulating the nanoparticles in a silica shell, nanoparticles retain high quantum yields and become water soluble. Photobleaching does not occur, even after prolonged exposure to irradiation, as there was no reportable loss in fluorescence. Core-shell nanoparticles using various dyes and lanthanide complexes were compared, with a trend observed. As more dye or complex was incorporated into the nanoparticle quantum yields increased from 44% to 60%. Nanoparticles synthesized in this manner displayed excellent cell uptake and cell viability.

In a publication by Fu-Min Xue and colleges, luminescent nanoparticles were synthesized using europium complexes⁵. A co-precipitation-condensation method in which PFOTS, [2H-perfluorooctyltrimethoxysilane] and P(ST-co-MMA), [poly(styrene-co-methacrylate)] were used as matrix materials, was developed to prepare core-shell $\text{Eu}(\text{tta})_3 \cdot \text{btp}$, [TTA = thenoyltrifluoroacetate, BPT = 2-(N,N-di-ethylanilin-4-yl)-4,6-bis(pyrazol-1-yl)-1,3,5-triazine] nanoparticle cores with a silica shell. The work showed the lanthanide complex was excited by visible light, 425 nm, with a quantum yield of 22%. The synthesized complex addresses some of the issues involving luminescent lanthanide complexes such as ultraviolet excitation, but is not ideal for biomedical use. The complex reported, $\text{Eu}(\text{tta})_3 \cdot \text{btp}$, is not dispersible in water and is unstable in polar solvents such as DMF, [DMF = dimethylformamide] THF, [THF = tetrahydrofuran] and alcohols. The

purpose of their work was to improve the solubility of this lanthanide complex to apply them for biomedical use. The results show that the nanoparticles were dispersible in water and maintained a high quantum yield with the silica shell encapsulating them

1.1.3 Introduction to Research

Dual modality nanoparticles are a growing field of special interest. Creating dual modality nanoparticles involves combining two chemical or physical properties into one nanoparticle. For biomedical imaging, combining a paramagnetic property with a luminescent one creates a nanoparticle capable of dual images. The magnetite nanoparticles, using the T_2 weight, can produce MRI images as seen in previous research, while the luminescent property can add another spectrum. The nanoparticles, when coordinated with a tumor via a biocompatible linker, can be exposed to a laser using a laparoscopic technique. A detector can be merged with the device to count incoming photons from the luminescing nanoparticles. The image could show a clear indication of where the nanoparticles have coordinated, and thus the location of the tumor. These two images could then be overlaid on top on one another giving the medical team a more accurate image for use in surgery. Combining magnetite with a lanthanide is a common way to achieve both of these desired properties. Due to their structure, size, emission, and magnetic properties these nanoparticles are believed to have great potential as dual functional probes for highly sensitive imaging applications⁷. Obtaining monodispersed nanoparticles of the correct size and shape, while maintaining paramagnetic properties and producing sharp emission bands, could have great potential in future medical endeavors. Only one of the literature sources found at this time for dual modality nanoparticles are using lanthanide doped iron oxide as a core for their nanoparticles, although there are

examples of dual modality nanoparticles processing both paramagnetic and luminescent properties.

Most of the examples of dual modality nanoparticles use an “antenna” system with lanthanide complexes. In a publication by Wang and coworkers, the nanoparticles consisted of iron oxide cores to provide the paramagnetic properties, while a lanthanide complex acts as the luminescent probe⁸. The chromophore is a quinolone-based dye which transfers energy to the lanthanide metal ion, in this case terbium. Binding the antenna to the nanoparticle was accomplished through the use of polyethylene glycol 3,4-dihydroxybenzylamine for both binding affinity and water solubility. While the publication discusses the long fluorescent lifetimes and their dispersibility in water, it fails to discuss the event of dissociation of the sensitizer and the toxic effects of lanthanide complexes free in the body.

Another instance of using an “antenna” system is seen in a publication by Xi and coworkers in which a magnetite core is conjugated with tris(dibenzoylmethane)-5-amino-1,10-phenanthroline, (BMAP), europium complex⁷. The results show strong luminescent intensities with a quantum yield of 5.8%. Cell viability studies show that under physiological conditions the nanoparticles are non-toxic. However, in the supplemental section, at more acidic conditions the complex begins to dissociate and cause free metal ions in solution. For acidic conditions, the probability of protonation of the antenna and free metals ions in the body, namely europium, increases. The study also showed the cell imaging possible with these nanoparticles using Her2-positive breast cancer SK-BR-3 cells in a petri dish. This study does not show selectivity on the part of the nanoparticle, as they were the only cells present in the petri dish. While “antenna” models show promising

results in luminescence, they display potential shortcomings in matters such as possible free metal ions from dissociation and with selectivity. For the nanoparticles to be good biomedical probes or labels they must have an affinity for only the cells wished to be targeted. Nanoparticles must have a biocompatible linker to coordinate with only the cells of interest. If the nanoparticle is already surface coated with a sterically hindering antenna then coordination with only cells of interest will be difficult. In Figure 1.1 the structure of the “antenna” system employed in this paper is shown. This is a large molecule and could experience steric hindrance if attempting to coordinate with a cell of interest after a second linker is added.

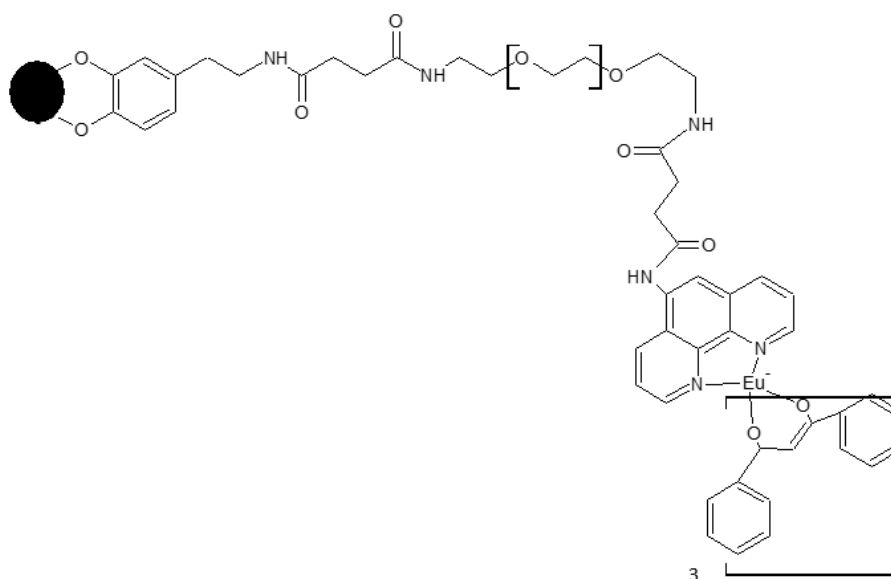


Figure 1.1. Schematic of magnetite nanoparticle with “Antenna” system.

To circumvent these problems, while still synthesizing dual modality nanoparticles, attempts have been made for lanthanide-doped nanoparticles. Typically, doping refers to

intentionally adding impurities to a system, usually done for semiconductors to provide a path for electron travel. For dual imaging nanoparticles, doping involves the actual coordination of the lanthanide into the crystal structure of the nanoparticle. For the nanoparticles in this research, this comprises europium doped into the crystal lattice of magnetite. Doping can take place by displacing iron in the magnetite unit cell. Europium has an ionic radius of 107 pm, while iron has an ionic radius of 55 pm. Europium has a larger ionic radius but could potentially dislodge an iron atom and take its place in the crystal. Another possible method of doping involves the europium atom coordinating within the unit cell of magnetite. The volume of a unit cell of magnetite is $5.905 \times 10^8 \text{ pm}^3$, a big enough volume to accommodate a europium metal ion³. Either of these examples of doping removes the need for an “antenna” to chelate a lanthanide complex.

An example of doping is found in a paper by Li and Zhang, in which an iron oxide core is coated in silica and then doped with a pentetic acid derivative, a conjugated ligand with a high affinity for metal cations, to provide numerous coordination sites with another lanthanide complex using terbium and gadolinium⁹. This lanthanide complex however is still an antenna with a sensitizer chelated with the Tb or Gb. These nanoparticles exhibit sharp, intense fluorescent peaks and paramagnetic properties but are quite large for nanoparticles, between 80 and 100 nm. As with the previous example of lanthanide complexes, the issue of dissociation of the lanthanide complex and the resulting, possibly toxic, free lanthanide ions in the body could result from using an antenna chelator system. A nanoparticle in which the lanthanide is doped straight into the magnetite nanoparticle is the basis for the research of this thesis.

By doping the iron oxide nanoparticles with europium ions, instead of using a chelator complex, the europium will be tightly bound within the crystal structure and will be unlikely to dissociate. This prevents the possibility of dissociation and free metal ions in the body. The nanoparticles would also not have the long “antenna” system used for most dual modality nanoparticles and therefore not be hindered by steric effects. The europium doped magnetite nanoparticles would still retain paramagnetic properties typical of magnetite while adding the luminescent properties associated with europium.

Core-shell nanoparticles are also an area drawing research attention. Many examples of core-shell nanoparticles involve a core coated with silica, as discussed previously⁵. Coating commonly involves using silica as either the shell or an intermediate step between the core and shell. Coating the core with a lanthanide such as europium would be another method for developing dual modality nanoparticles. A case involving core-shell nanoparticles, magnetite cores with a lanthanide shell, is seen in the work of Zhong and Yang¹⁰. The method uses thermal decomposition to synthesize iron oxide nanoparticles coated in oleic acid as a surfactant. Once the magnetite core, surface coated in oleic acid, is synthesized the surfactant is not removed to grow the lanthanide shell. Instead, the lanthanide is grown onto the shell of the iron oxide core in the presence of 1-octadecene and oleic acid. This crystal lattice structure should be similar to that of the core, of which the lanthanides chosen in this procedure are, and will grow on the surface of the nanoparticle even with a surface coating of oleic acid. Oleic acid is then removed and a sensitizer added to the surface coating to facilitate the energy transfer necessary for the luminescence. For core-shell nanoparticles the hypothesis is that the resulting nanoparticles should be larger than the magnetite core alone, but should have more intense luminescent

peaks while still having paramagnetic properties associated with magnetite. The more intense luminescent peak is due to the lanthanide coating the nanoparticle rather than doping, with the surface coating grown over the core of iron oxide and eliminating the quenching due to surface defects. Also, there will have be a greater percentage of europium on the nanoparticle with a surface coating rather than with doping.

For the purpose of this research both europium-doped magnetite nanoparticles and core-shell nanoparticles will be synthesized to optimize magnetic and luminescent properties. The theory is that doping nanoparticles will display dual characteristics while maintaining a small monodisperse size distribution. The nanoparticles will be thermally decomposed to allow for doping to occur and tested with a chromophore to calculate quantum yields. Core-shell nanoparticles were also synthesized as a comparison to those doped with europium. Retaining the europium inside the magnetite core lowers the possibility of dissociation into the body while allowing for future coordination with a biocompatible linker for increased selectivity. This work is done in continuing research for dual modality nanoparticles for biomedical imaging applications.

1.2 PROJECT DESIGN

1.2.1 High Temperature-Based Thermal Decomposition

The basis for the design of this project was the synthesis of dual modality nanoparticles with both paramagnetic and luminescent properties. Three different synthesis methods were used, high temperature-based thermal decomposition, low temperature-based co-precipitation, and core-shell nanoparticle synthesis. The high temperature nanoparticles will be synthesized using the thermal decomposition of $\text{Fe}(\text{acac})_3$, $\text{Eu}(\text{btfa})_3(\text{H}_2\text{O})_2$ [acac = acetylacetonate, btfa = 4,4,4-trifluoro-1-phenyl-2,4-butanedione],

and 1,2-hexacanediol precursors in the presence of oleic acid, oleylamine, and diphenyl ether. (Figure 1.2) $\text{Eu}(\text{btfa})_3(\text{H}_2\text{O})_2$ is a novel starting material for the purposes of doping. $\text{Fe}(\text{acac})_3$ is to be the iron source while 1,2-hexacandiol is a reducing agent to acquire both the Fe^{2+} and Fe^{3+} needed to form magnetite.

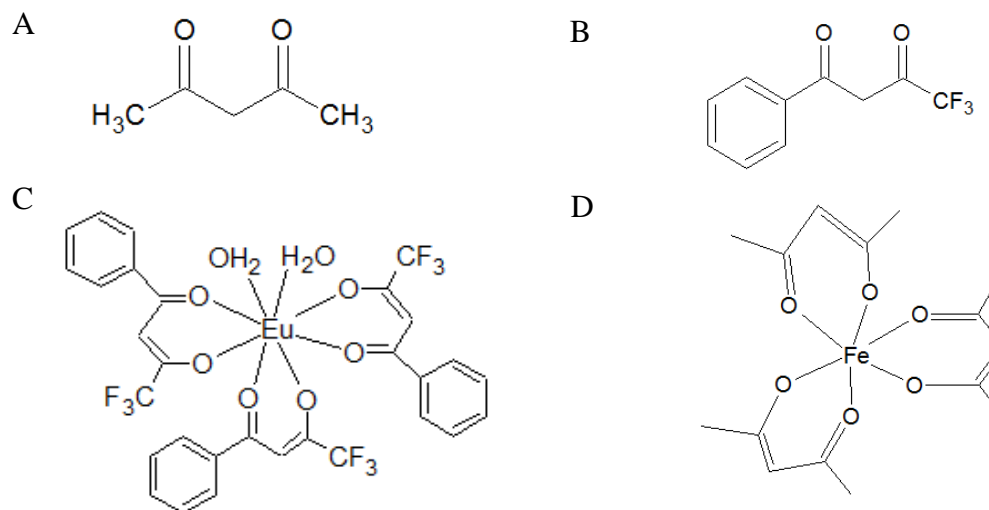


Figure 1.2. [A] Acetylacetonate [B] 4,4,4-trifluoro-1-phenyl-2,4-butanedione [C] $\text{Eu}(\text{btfa})_3(\text{H}_2\text{O})_2$ [D] $\text{Fe}(\text{acac})_3$.

Since this is a high temperature thermal decomposition, a solvent and surfactant which could withstand high temperatures were needed to promote the decomposition, which occurs at a higher temperature. The surfactants chosen are oleic acid and oleylamine, both long chain fatty acids capable of withstanding higher temperatures. The surfactants act as a capping ligand to stop the aggregation of atoms and produce nanoparticles. During synthesis, the reactants are thermally decomposed and begin to form the face centered cubic crystal lattice typical of magnetite. Argon is needed to displace oxygen and create an inert environment to avoid oxidation of iron oxide from magnetite to hematite. This crystal

lattice structure should also now be doped with the lanthanide, europium. Due to the high temperature synthesis method the nanoparticles also should be smaller than those synthesized through a lower temperature method.

To be surface coated with a chromophore and to become hydrophilic the surfactants coating the surface of the high temperature nanoparticles have to be removed. Oleic acid and oleylamine are hydrophobic. For the nanoparticles to be effective as biomedical imaging agents they have to be readily dispersed in water. To remove the surfactants, the nanoparticles were to be treated with an acidic solution. This acidic condition promotes the removal of the surfactant by protonating the carboxylic group at the coordination site of the magnetite nanoparticle. (Figure 1.3)

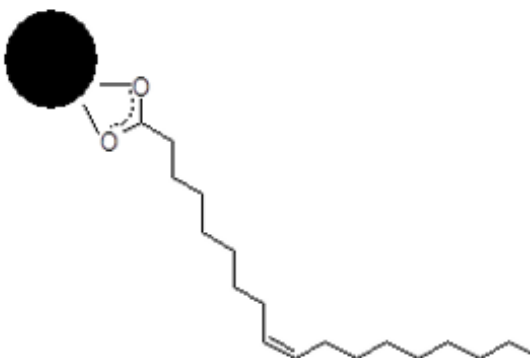


Figure 1.3. Nanoparticle surface coated with surfactant oleic acid.

After complete removal of the surfactant, the nanoparticles are readily dispersible in water. This allows for continuing on to the next step, involving surface coating the nanoparticles in the chromophore.

1.2.2 Low Temperature-Based Co-Precipitation

Low temperature-based co-precipitation of europium doped nanoparticles were synthesized using $\text{FeCl}_3 \cdot 6\text{H}_2\text{O}$, $\text{FeCl}_2 \cdot 4\text{H}_2\text{O}$, and $\text{EuCl}_3 \cdot 6\text{H}_2\text{O}$. The two iron sources used will compose the mixed valency needed to form magnetite, (Fe^{2+} and Fe^{3+}). $\text{EuCl}_3 \cdot 6\text{H}_2\text{O}$ was used as the lanthanide source, with water as the solvent. This is to be a much lower synthesis temperature with a heating temperature of 80 - 90°C. Again argon was used to displace oxygen and create an inert environment in which to synthesize nanoparticles. Citric acid acted as the surfactant. This was done due to the low temperature method of co-precipitation as citric acid has a low melting point. Citric acid also dissolves readily in water making the nanoparticles dispersible in water immediately after synthesis. NH_4OH was added during synthesis to maintain a proper neutral pH and later during synthesis to precipitate nanoparticles from solution. Using citric acid as a surfactant also eliminated the step involved with surfactant removal as citric acid coated nanoparticles disperse easily in water.

To determine optimal ratios between the paramagnetic properties of iron oxide and the luminescent properties of europium various doping percentages of europium were performed. Initial doping ratios were 16:84 europium to iron oxide but three more doping ratios were to be tried to determine an ideal ratio of these two metals. The remaining three doping ratios were 20:80, 30:70, and 40:60. This is a linear doping progression. Along with finding the optimal ratio of europium to iron oxide, the amount of chromophore needed to surface coat the nanoparticles to produce the greatest luminescence for each doping ratio was also tested. The low temperature nanoparticles were synthesized as a way to gather data during testing of variables such as europium doping amounts and a chromophore

surface coating. During synthesis of high temperature nanoparticles very low yields were observed. As a way of improving yields a low temperature method, which produced a greater quantity of nanoparticles with a shorter synthesis time, was used to test such variables. The data gathered from quantum yield was used to determine optimal doping percentages and chromophore surface coating amounts. This data was then transferred to the high temperature nanoparticles to test if this trend was seen with the high temperature as well. With these nanoparticles it was possible to test all variables necessary involving doping and a chromophore.

1.2.3 Core-shell Nanoparticle Project Design

Synthesis of magnetite cores was done in the same manner as with the high temperature method of thermal decomposition with the exception of $\text{Eu}(\text{btfa})_3(\text{H}_2\text{O})_2$. This was done to ensure that any europium ions that coordinated with the magnetite core did so on the surface of the nanoparticle as the shell. For the synthesis of the europium shell a literature source procedure was not employed. The surfactant coated cores were dispersed in toluene and then an acidic solution will be added to the nanoparticle solution. A solution containing EuCl_3 dissolved in water was also added, forming two distinct layers. The theory for shell formation was that as the H^+ ions protonate the surfactant, the nanoparticle would become hydrophilic and move into to the aqueous layer. Here the O^{2-} of the magnetite crystal lattice structure, (Fe_3O_4) , would allow a coordination site with the europium metal ion. This will be a simple synthesis method that would create core-shell nanoparticles that were water soluble immediately after formation. The concept for core-shell dual modality nanoparticles is to have a larger europium coordination site than is possible through doping alone. With the surface area of the core-shell nanoparticles coated

in europium metal ions, a chromophore will be coordinated directly to the europium and will produce a more intense luminescence due to more europium, and direct chromophore coordination. This should result in nanoparticles with paramagnetic properties associated with magnetite along with greater luminescence intensities than with europium doped magnetite nanoparticles.

1.2.4 Surface Coating with a Chromophore

Once the nanoparticles were made available for coordination with a chromophore, an appropriate sensitizer had to be selected. Since f to f transitions are Laporte forbidden, a chromophore or sensitizer must be used to transfer the energy of the photon from the ligand to the lanthanide metal ion to allow luminescence. Using a europium metal ion, the chromophore has to use Förster energy for the intermolecular energy transfer. Förster energy transfer refers to a nonradiative electronic energy transfer from a donor to an acceptor. Förster energy transfer has a limited range of interaction, typically 1 – 10 nm.

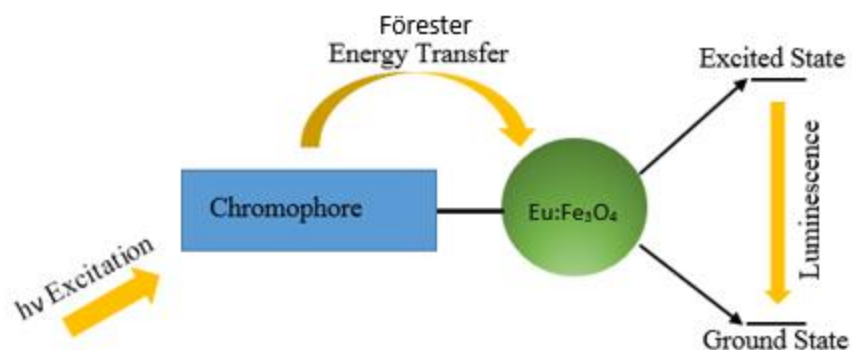


Figure 1.4. Schematic illustrating the incoming light transferring from the chromophore to the lanthanide.

To calculate energy transfer distances the equation $1/R^6$ is used which predicts distance dependence of the energy transfer rate.

This is another reason keeping the size of the nanoparticle small is important. If the nanoparticle is too large then the chromophore will not be able to transfer energy to all of the europium doped within the nanoparticle and this europium will be unused. Figure 1.4 shows an illustration of the actions performed by the chromophore and europium doped magnetite nanoparticle. The sensitizer chosen for this project is TTA. (Figure 1.5)

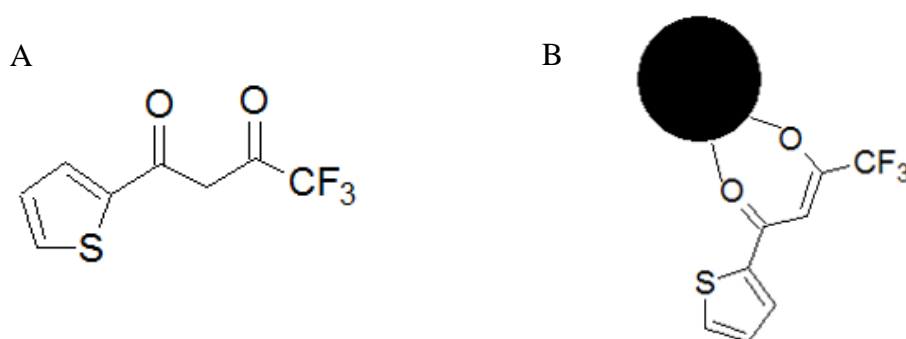


Figure 1.5 A-B. [A] Structure of organic chromophore TTA. [B] TTA surface coordinated to the synthesized nanoparticle.

TTA has an excited triplet energy level comparable to that of the f^* levels of the europium ion. The electronic energy difference between the triplet level of the chromophore and the 5D_0 level of the europium metal ion is crucial for the ligand-to-metal electronic energy transfer. This allows for an intramolecular energy transfer of the photons energy to the excited state of the chromophore, then to the triplet state of the chromophore

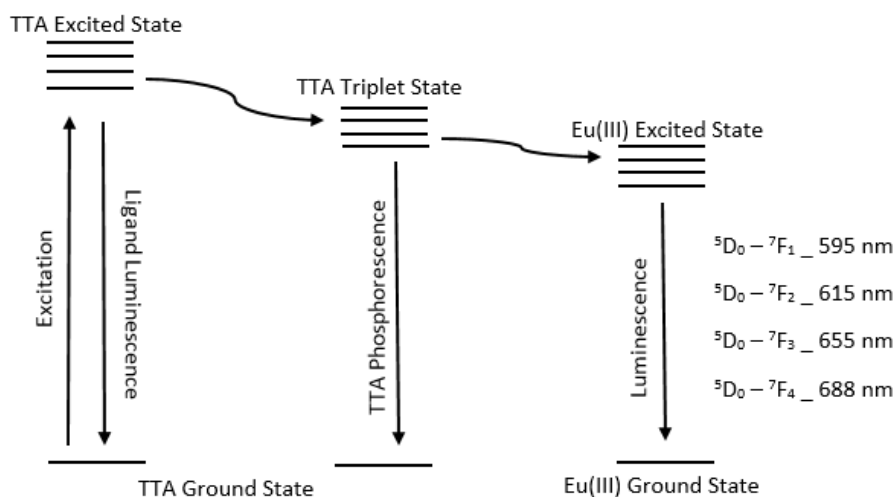


Figure 1.6. Electronic energy transitions diagram from the ground state of the TTA to europium excited state to the ground state through luminescence.

through intersystem crossing, and then to the lanthanide by Förster energy transfer, where relaxation to the ground state in the europium takes place through luminescence. (Figure 1.6) TTA is an ideal choice for a sensitizer due to the ability of this electron transfer through similar energy levels between the excited sensitizer electron and the europium metal ion.

The purpose of this research is to improve the luminescent qualities of magnetite nanoparticles through doping or surface coating with europium and a chromophore. Through improving the luminescent qualities it is believed that the magnetic properties of magnetite will remain to create dual modality nanoparticles for MRI and luminescent biomedical imaging.

CHAPTER 2

EXPERIMENTAL

2.1 ALL NANOPARTICLE SYNTHESSES

All the reagents were purchased from Aldrich or Fisher Scientific. The reagents were used without further purification. Nanopure water with a resistivity of 18.2M Ω was obtained from a Barnstead NANOpure Diamond system with a 0.2 μ m hollow fiber filter.

2.1.1 Low Temperature Synthesis of Eu(III)-Doped Fe₃O₄ Nanoparticles

Low temperature Eu(III)-doped Fe₃O₄ nanoparticles were synthesized by using FeCl₃·6H₂O and FeCl₂·4H₂O as the iron sources and EuCl₃·6H₂O as the lanthanide source. The nanoparticles were synthesized using a modified literature procedure¹³. FeCl₃·6H₂O (2.1925g, 0.00811 mol), FeCl₂·4H₂O (0.8735g, 0.00439 mol), and EuCl₃·6H₂O (0.584g, 0.00159 mol), were placed in a 100 mL round bottom flask with argon-purged nanopure water (90 mL). Citric acid (1.25g, 0.00651 mol) was dissolved in nanopure water (10 mL) in a separate 50 mL round bottom flask. The citric acid solution was then added to the solution containing iron and europium chloride while flushing with argon. After the solution was mixed, pH of the solution was adjusted to 7.0 using NH₄OH solution (29%, 3 mL). After adding the 29% NH₄OH, the reaction changed color from a light brown transparent color to a black opaque. This solution was then heated to 80°C for two hours while stirring and flushing with argon. A condenser tube was set into the round bottom flask to establish a path for argon flush. At the end of two hours, 29% NH₄OH (10 mL) was added and the solution was heated to 90°C for one half hour. The nanoparticles were then precipitated using 95% ethanol (250 mL) and collected in 50 mL conical centrifuge tubes. The precipitated nanoparticles were centrifuged for 30 minutes at 3,720 g at 20° C.

After centrifugation, the nanoparticles were dispersed in water and precipitated again using 95% ethanol to be centrifuged. This was done a total of three times to remove any excess reactants and surfactant.

Nanoparticles were then placed into a separated 50 mL round bottom flask for drying. A Brandtech Vucubrand Vap 5 vacuum dryer with a liquid nitrogen cold neck was used to remove any excess solution. The nanoparticles were placed on the vacuum dryer for a total of 5-7 hours or until a dry powder was obtained. The dried nanoparticles were then collected in a glass sample vial, flushed with argon, capped and sealed with parafilm for later use.

2.1.2 Synthesis of $\text{Eu}(\text{btfa})_3(\text{H}_2\text{O})_2$ Precursor Complex

$\text{Eu}(\text{btfa})_3(\text{H}_2\text{O})_2$ complex was synthesized using a literature source¹⁴. 4,4,4-trifluoro-1-phenyl-2,4-butanedione (Hbtfac) (0.64848 g, 0.003 mol) and NaOH (0.119994 g, 0.003 mol) were placed in a 50 mL round bottom flask with distilled water (10 mL) and mixed until dissolved. $\text{EuCl}_3 \cdot 6\text{H}_2\text{O}$ (0.336 g, 0.001 mol) was mixed with distilled water (5 mL) until dissolved in a separate 10 mL round bottom flask. The two solutions were then combined into the 50 mL flask and a white precipitate was observed. The solution was heated to 60° C while stirring for 30 minutes. At the end of heating, the solution was stirred at room temperature for an additional 3 hours. The white precipitate was collected through vacuum filtration and washed with distilled water (100 mL) and hexane (3 mL). The product was air dried to obtain a dry powder.

2.1.3 High Temperature Synthesis of Eu(III)-Doped Fe_3O_4 Nanoparticles

High temperature Eu(III)-doped Fe_3O_4 nanoparticles were synthesized by using $\text{Fe}(\text{acac})_3$ and a $\text{Eu}(\text{btfa})_3(\text{H}_2\text{O})_2$ coordinated complex prepared from a literature source¹⁴.

The nanoparticles were synthesized using a literature procedure with slight modifications¹⁵. $\text{Eu}(\text{btfa})_3(\text{H}_2\text{O})_2$ (0.0621 g, 0.07439 mmol), $\text{Fe}(\text{acac})_3$ (0.13279 g, 0.376 mmol), 1,2-hexadecandiol (0.22097 g, 0.855 mmol) and diphenyl ether (15mL) were placed in a round bottom flask and heated to approximately 170°C while pushing argon gas into the top of the condenser with stirring. Vacuum was applied to facilitate the complete removal of residual water in the reaction mixture. Heat was then removed to allow solution to cool to room temperature. Vacuum was continuously applied to the solution until the solution came to room temperature to ensure complete removal of water. Before heating, the solution was a light brown/orange color. During heating, the solution became a dark black color.

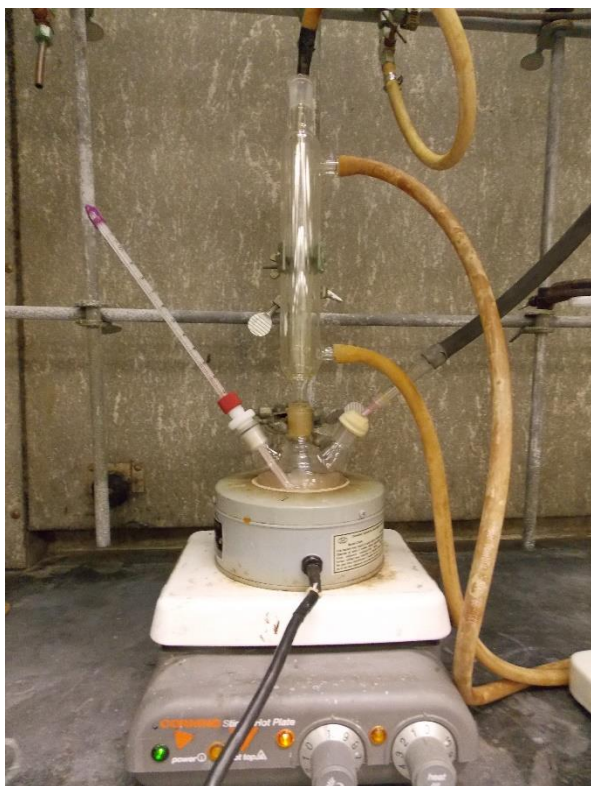


Figure 2.1. Reaction setup to remove residual water from reaction mixture.

After removal of residual water, oleic acid (600 μL) and oleylamine (560 μL) were added and the solution was refluxed at 260°C for 6 hours under argon. The nanoparticles

were precipitated by adding a solution of 95% ethanol (100 mL). The precipitated nanoparticles were placed in 50 mL conical tubes. The nanoparticles were then centrifuged for 30 minutes at 3,720 g at 20° C. Excess solution was decanted and the nanoparticles were suspended in toluene (3 mL). The nanoparticles were then precipitated again using 95% ethanol and centrifuged. The purification of nanoparticles was done three times. After the final wash the nanoparticles were dispersed in toluene and placed in a glass sample vial. The nanoparticles were flushed with argon, capped, and sealed with parafilm before storing for later use.



Figure 2.2. Reaction setup for reflux conditions.

2.1.4 Synthesis of Core-Shell Eu(III) Coated Fe₃O₄ Nanoparticles

Cores for the core-shell nanoparticles were synthesized with the same procedure as high temperature thermal decomposition nanoparticles with the exception of excluding

$\text{Eu}(\text{btfa})_3(\text{H}_2\text{O})_2$ ¹⁵. The exclusion of $\text{Eu}(\text{btfa})_3(\text{H}_2\text{O})_2$ during the synthesis of the cores helped to ensure that europium was only available for surface coordination. Starting materials were $\text{Fe}(\text{acac})_3$ complex (0.13279 g, 0.376 mmol), 1,2-hexadecandiol (0.22097 g, 0.855 mmol), oleic acid (600 μL), oleyl amine (560 μL) and diphenyl ether (15mL). After the nanoparticles were purified and dispersed in toluene a portion was dried with argon to determine the weight of dried nanoparticles. $\text{EuCl}_3 \cdot 6\text{H}_2\text{O}$ (100 mg, .27292 mol) was added to dry Fe_3O_4 nanoparticles (60 mg, .0003 mol). The dried nanoparticles were then redispersed in toluene. $\text{EuCl}_3 \cdot 6\text{H}_2\text{O}$ was dissolved in nanopure water (1 mL). An HCl solution, pH 3.5-3.6, was prepared using 1.0 M HCl and distilled water. The HCl and EuCl_3 solutions were added to the nanoparticle solution in a glass sample vial. The solution was then stirred for two hours on a Burrell Wrist Action shaker, model 75, at a speed setting of 10 at room temperature.

After mixing, the nanoparticle solution was treated with a series of separations using anhydrous ether and nanopure water. The aqueous layers were collected, containing the core-shell nanoparticles and separated again using ether. The nanoparticles were collected using a neodymium magnet and washed with nanopure water (10 mL) three times.

2.1.5 Surfactant Removal From Eu(III)-Doped Fe_3O_4 Nanoparticles Prepared Using High Temperature Method

The surfactant was removed to produce hydrophilic nanoparticles that could be readily dispersed in water. The surfactant removal also facilitates the addition of a chromophore for the purpose of lanthanide based luminescence. Surfactant removal for high temperature nanoparticles was done in two steps to ensure complete removal. First,

the nanoparticles suspended in toluene were dried with argon to remove the solvent. A citric acid buffer was prepared using citric acid (0.9618 g, 0.50 mol) dissolved in nanopure water (50 mL). A 1.0M NaOH solution was added dropwise to reach the desired pH of 3.5-3.6. The citric acid buffer solution (10 mL) was added to the dried nanoparticles and mixed for two hours at room temperature in a vortex mixer at a speed setting of 4.

After the two hour mixing at room temperature the nanoparticle solution was treated with a series of separations using anhydrous ether and nanopure water. At each separation the aqueous layer, containing the surfactant free nanoparticles, was retained and further separated using ether. The collected nanoparticles were retained with a neodymium magnet and washed with nanopure water to ensure a neutral pH. A second treatment involving an HCl solution was then performed. The HCl solution was mixed using 1.0 M HCl and distilled water to attain a pH of 3.5-3.6. The nanoparticles treated with the citric acid buffer solution were held with a magnet in the sample vial to decant neutral pH water solution and an HCl solution (10 mL) was added into the sample vial. The nanoparticles in solution were then mixed in a vortex mixer at speed setting of 4 for two hours at room temperature. After mixing, the nanoparticle solution was treated again with a separation involving anhydrous ether and nanopure water as mentioned above. The aqueous layers were retained and washed with nanopure water to ensure neutral pH for storage.

2.1.6 Surface Coating of Eu(III)-Doped Fe₃O₄ Nanoparticles With TTA

The citric acid coated, surfactant free, or core-shell nanoparticles were dispersed in nanopure water (1 mL) in a glass sample vial. Using a solution of TTA (0.0135 g, 0.0607 mmol), Eu(III)-doped Fe₃O₄ nanoparticles (63.29 mg) and N,N-diisopropylethylamine, (15 μ L) in nanopure water (2 mL). This ratio of TTA to europium doped iron oxide

nanoparticles is for 32 mg TTA: 75 mg nanoparticles, for complete ratios of TTA to nanoparticle mass see Table 2.1. The solution was added to the nanoparticles and mixed in a Burrell Wrist Action shaker (model 75) at a speed setting of 10 for two hours at room temperature. For the high temperature and core-shell nanoparticles, when mixing is complete, the TTA surface coated nanoparticles were held in place with a neodymium magnet while the additional solution was decanted off. The nanoparticles were washed three times with nanopure water.

Table 2.1. Varying amounts of TTA to nanoparticle by mass.

TTA (mg)/Nanoparticle (mg)	TTA (mg)	Nanoparticle (mg)
8/75	6.751	63.29
16/75	13.50	63.29
32/75	27.00	63.29
40/75	33.75	63.29
48/75	40.51	63.29
64/75	54.01	63.29
90/75	75.95	63.29

The solution of nanoparticles was then concentrated in 1:1 95% ethanol/nanopure water (1 mL) in a glass sample vial. For low temperature nanoparticles the TTA surface coated nanoparticles were collected in 1:1 95% ethanol/nanopure water (15 mL) and centrifuged for 30 minutes at 1,163 g. After centrifugation the excess solution was decanted and the nanoparticles were collected in 1:1 95% ethanol/nanopure water (1 mL) in a glass

sample vial. High temperature method and core-shell nanoparticles were collected with a neodymium magnet and dispersed in 1:1 ethanol/nanopure water (1 mL).

2.2 MATERIALS CHARACTERIZATION

Synthesized nanoparticles were characterized using Fourier-transform infrared spectroscopy (FT-IR), transmission electron microscopy (TEM), UV-visible and fluorescence spectroscopic techniques, X-ray powder diffraction (XRD), and inductively coupled plasma optical emission spectroscopy (ICP-OES). The methods used for characterization will be discussed in this section along with all instrument specifications.

2.2.1 FTIR

FT-IR spectra were obtained using a Perkin Elmer Spectrum One or a Thermo Scientific Nicolet iS10. All measurements were performed at room temperature. The Perkin Elmer instrument spectra was performed using a diamond/ ZnSe crystal. A scan speed of 0.2 cm/s and a resolution of 4 cm⁻¹ with a total of 16 scans per spectrum was used. The scanning range used was from 4000 cm⁻¹ – 600 cm⁻¹. For the Thermo Scientific instrument, the crystal used was a diamond with a HeNe laser. A scanning range of 4000 cm⁻¹ – 525 cm⁻¹ and an optical velocity of 0.4747 cm/s were used with a resolution of 4 cm⁻¹. Spectra were obtained with 32 scans per spectrum. Most materials were measured in the solvent used during the reaction, such as citric acid in water or nanoparticles in either 1:1 95% ethanol/water or toluene. For these, a background was first collected using the solvent. For materials measured as a solid powder, such as TTA, or as a pure liquid, such as oleic acid or oleylamine, the background performed was of atmosphere. The instrument was cleaned with a lint free Kim Wipe and acetone in between each measurement and the spectra were saved on the Neon drive.

2.2.2 TEM

Size and shape of Eu-doped iron oxide nanoparticles was determined using a TEM 9500 microscope with an operating voltage of 300 kV. Samples were prepared by making a dispersion of nanoparticles (1mg nanoparticles / 1 mL solvent) and adding a drop (200 μ L) of the sample on a carbon coated grid (300 mesh). Samples were dried in air at room temperature for 4 hours.

2.2.3 UV-Visible Absorption Spectroscopy

UV-Vis spectra were collected using an Alignment 8453 UV-Vis spectrometer at room temperature. This instrument uses a deuterium lamp for UV measurements, and a tungsten lamp for visible measurements. Wavelength range was measured from 190 nm – 1100 nm at a 1 nm interval and an integration time of 0.5 seconds. Measurements were taken using a quartz cuvette with a path length of 1 cm. Blanks were obtained in the solvent used to suspend the sample. For untreated nanoparticles, this was either water or toluene. For nanoparticles surface coated with TTA the nanoparticles were dispersed in 1:1 95% ethanol/ water and a blank of the solvent was taken first. During quantum yield measurements cresyl violet was used as a reference. The cresyl violet was dissolved in methanol, a blank containing methanol was used during these measurements. While performing quantum yield measurements, the absorbance values of 0.2 -0.6 were used. Cresyl violet used during the quantum yield measurements was measured with an absorbance intensity less than 0.1. All spectra were saved to the Neon drive.

2.2.4 Fluorescence Spectroscopy

Fluorescence spectra were acquired using a Perkin Elmer LS-55 Luminescence Spectrometer at room temperature. For nanoparticles, the solvent used was 1:1 95%

ethanol/water, and for cresyl violet the solvent was methanol. A quartz cuvette was used for all measurements. A scanning range of 570 nm – 670 nm with a scan speed of 200 nm/min was used, with an excitation and emission slit of 5.0 nm. For nanoparticles, the excitation wavelength was 338 nm, while for cresyl violet the excitation wavelength was 594 nm. All spectra were saved to the Neon drive.

2.2.5 XRD

A Rigaku Miniflex was employed to perform X-ray powder diffraction full spectrum scans from 2θ 3° - 90° degrees. A scan speed of 0.5 scans/minute with a scattering slit of 4.2 degrees and a receiving slit of 0.3 mm was used. A cobalt $K\alpha_1$ (0.57789 Å) X-ray source was used for all measurements¹⁶. The spectra were processed using Jade 7 XRD pattern processing and identification software installed in the instrument. This software was used to calculate FWHM for later processing. Further programming was developed in Octave-3.6.4 to load a spectrum from the Rigaku Miniflex onto Octave for calculating the FWHM and the average crystal size using the Scherrer equation. The program written for this purpose can be found in Supplemental Information. All spectra were saved on the C drive of the instrument operating system.

2.2.6 ICP-OES

ICP-OES data was collected using a Perkin Elmer Optical Emission Spectrometer Optima 4100 DV. Pump flow rate for water cooling was 1.5 mL/min. Gas flow of argon to plasma was 15 L/min. Argon gas flow to the nebulizer was 0.8 L/min, with an auxiliary gas flow rate of 0.2 L/min. There were five analytical wavelengths in total chosen for determining iron and europium concentrations. Three for iron at 238.204 nm, 239.566 nm,

and 259.939 nm. Two wavelengths were selected for europium at 381.967 nm and 393.048 nm.

Standards used for calibration curves were made in the following manner. For iron standard $\text{Fe}(\text{NO}_3)_3$ (0.18 g, 0.7442 mmol) was dissolved in nanopure water and diluted to 500 mL in volumetric flask. Europium standard was made by dissolving $\text{Eu}(\text{NO}_3)_3$ (0.0734 g, 0.1645 mmol) in nanopure water and diluting to 500 mL in volumetric flask. A blank standard of 10% nitric acid was made by diluting 69.5% HNO_3 (72 mL) with nanopure water to 500 mL in volumetric flask. These standards were used for all calibration curves or dilutions. A calibration curve was developed to ensure concentrations of iron and europium were in range. (Table 2.2)

Table 2.2. Calibration curve solution concentrations for ICP-OES.

	Fe Stock Solution (50 ppm)	Eu Stock Solution (50 ppm)	10% HNO_3 Solution
500 ppb	50 μL	50 μL	24.9 mL
1 ppm	1.0 mL	1.0 mL	23.0 mL
3 ppm	3.0 mL	3.0 mL	19.0 mL
5 ppm	5.0 mL	5.0 mL	15.0 mL
7 ppm	7.0 mL	7.0 mL	11.0 mL

Concentrations for ICP-OES were kept within the range of calibration curve to ensure accuracy of measurements. Initial samples were made with concentrations of

approximately 2.5 - .006 mg/mL for ease of weighing. These samples were then further diluted to obtain correct concentrations. 15 μ L of the initial 2.5 mg/mL concentrated samples were further diluted to 10 mL in 10% HNO₃. All sample dilutions were to approximately 4 ppm. Initial masses of nanoparticles used for sample dilutions are provided in Table 2.3.

Table 2.3. Initial masses of nanoparticles for ICP-OES measurements.

Nanoparticle	Low Temp (g)	High Temp (g)	Core-Shell (g)
16:84	0.0235	.00688	
20:80	0.0285		
30:70	0.0244		
40:60	0.0256	.00586	
Cores			.0064
Core-shell			.0065

Each sample was ran three times with ICP-OES to determine the average concentrations of iron to europium for each nanoparticle ratio.

CHAPTER 3

RESULTS AND DISCUSSION

3.1 CO-PRECIPITATION Eu:Fe₃O₄ NANOPARTICLES

3.1.1 Synthesis and Crystal Lattice Formation

Eu(III)-doped magnetite nanoparticles synthesized using a low temperature-based co-precipitation method. Magnetite nanoparticles can be synthesized in various methods, including ultrasound irradiation, sol-gel, thermal decomposition, and co-precipitation. Of the various techniques employed to synthesize magnetite, co-precipitation is the most common, as it is the simplest of the synthetic methods and it produces the highest yields. Co-precipitations are based on the hydrolysis of a mixture of Fe²⁺ and Fe³⁺ ions, which are then used to fix the molar ratios in the inverse spinel structure¹⁷. Magnetite is usually prepared in this method by a stoichiometric mixture of ferrous and ferric salts in an aqueous alkaline solution¹⁸. The reaction is generally performed under an inert gas such as nitrogen or argon to avoid oxidation of Fe²⁺ ions preventing the formation of hematite. In most of the literature co-precipitation reactions take place between 70-80° C. The chemical equation for the reaction is shown in Equation 1.



During formation of magnetite, water is a byproduct, as a result of the hydroxides present in the alkaline solution used for precipitation. The disadvantages to the use of the co-precipitation method is that the control of size distribution is limited¹⁸. Often nanoparticles synthesized in this method are larger, and not of a uniform shape, than those

prepared using other methods. Using a chelating ion, such as citric acid or oleic acid during synthesis of magnetite, can limit this size distribution. If the ions chelating to the iron oxide nanoparticles deter nucleation then the nanoparticles formed will be larger. Nucleation is the beginning step involved with the formation of a crystal solid. The nucleation site is the initial site on which further particles deposit as the crystal grows. If the ions act as capping ligands and limit the growth of the nanoparticle, then smaller nanoparticles will form.

For the synthesis of low temperature-based Eu(III)-doped magnetite nanoparticles, a co-precipitation method was used for the advantages given. A method to quickly and simply produce large quantities of nanoparticles was needed to test all the variables involved for this research. The chelating ligand chosen for the co-precipitation synthesis was citric acid. This was also advantageous due to citric acid coated nanoparticles being readily dispersible in water. This saved the steps involved with removing the surfactant in order to surface coat the nanoparticle in TTA. The nanoparticles were known from initial production that they were not the ideal europium doped magnetite nanoparticle for the research project due to their tendency for large particle size and non-uniform size distribution. They were, however, ideal for testing across a range of optimizing variables.

For low temperature co-precipitation Eu(III)-doped magnetite nanoparticles, there were higher concentrations of nanoparticles available for surface coordination with TTA. After surface coordination, the nanoparticles in solution changed colors from black initially, to yellow, white, pink, and red. The amount of TTA coordinated determined the final color of the nanoparticles. For low amounts of TTA surface coordinated the nanoparticles were white in appearance. For the highest amount surface coordinated the

nanoparticle solutions were red. (Figure 3.1) Higher concentrations above 32 mg TTA/75 mg nanoparticles had a pink to red color in solution.

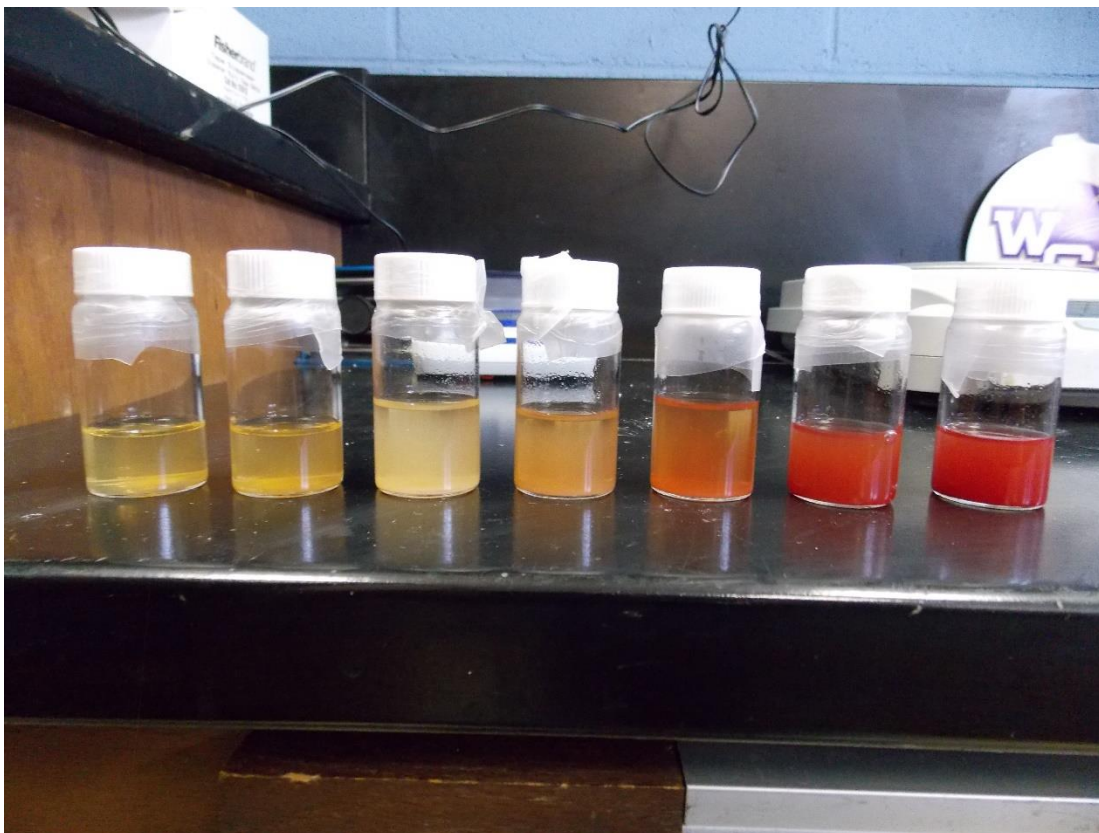


Figure 3.1. TTA coordinated co-precipitation nanoparticles with 8 mg, 16 mg, 32 mg, 40 mg, 48 mg, 64 mg, and 90 mg/75 mg nanoparticles in solution of 1:1 ethanol/water.

3.1.2 Magnetic Behavior of Magnetite Nanoparticles Synthesized Using Co-Precipitation Method

The low temperature-based europium doped nanoparticles upon completion of synthesis were a very dark black color when dispersed in water. A neodymium magnet was used to test paramagnetic properties of the nanoparticles dispersed in water. The nanoparticles did not display any significant magnetic properties, although the solution was dark and opaque making it difficult to observe nanoparticle movement. Later when the

nanoparticles were surface coated with TTA and the solution was clear, a neodymium magnet was left by the sample vial for approximately one half hour and a small amount of nanoparticles had begun to form a slight ring around the magnet. This suggests that the nanoparticles may not be highly paramagnetic. This made separation during synthesis more difficult as the nanoparticles could not be held in place with a magnet to decant off excess solution. Centrifugation had to be used for every separation and isolation of the nanoparticles.

Magnetic properties of magnetite nanoparticles are strongly dependent on the synthesis route involved. Factors that affect the paramagnetic properties involve particle size, spin disorder layer, incomplete crystallization of magnetite, and irregular morphologies of magnetite particles¹⁷. The low temperature nanoparticles exhibit one or more of these issues causing the lack of paramagnetic properties. During characterization with XRD the amorphous crystal structure of these nanoparticles strongly implies that the crystallization of magnetite did not completely form. This helps to explain why the low temperature nanoparticles were weakly paramagnetic.

3.1.3 XRD Studies

The nanoparticles were characterized using XRD to determine if the crystal structure of magnetite had formed, and to help calculate nanoparticle size using the Scherrer equation, an equation which utilizes the diffraction pattern of XRD to calculate average nanoparticle size. XRD spectra of the various doping percentages were obtained and all showed an amorphous crystal structure. The XRD spectra displayed broad peaks which could not be used to determine magnetite structure. Figure 3.2 shows the XRD spectrum nanoparticles surface coated in citric acid.

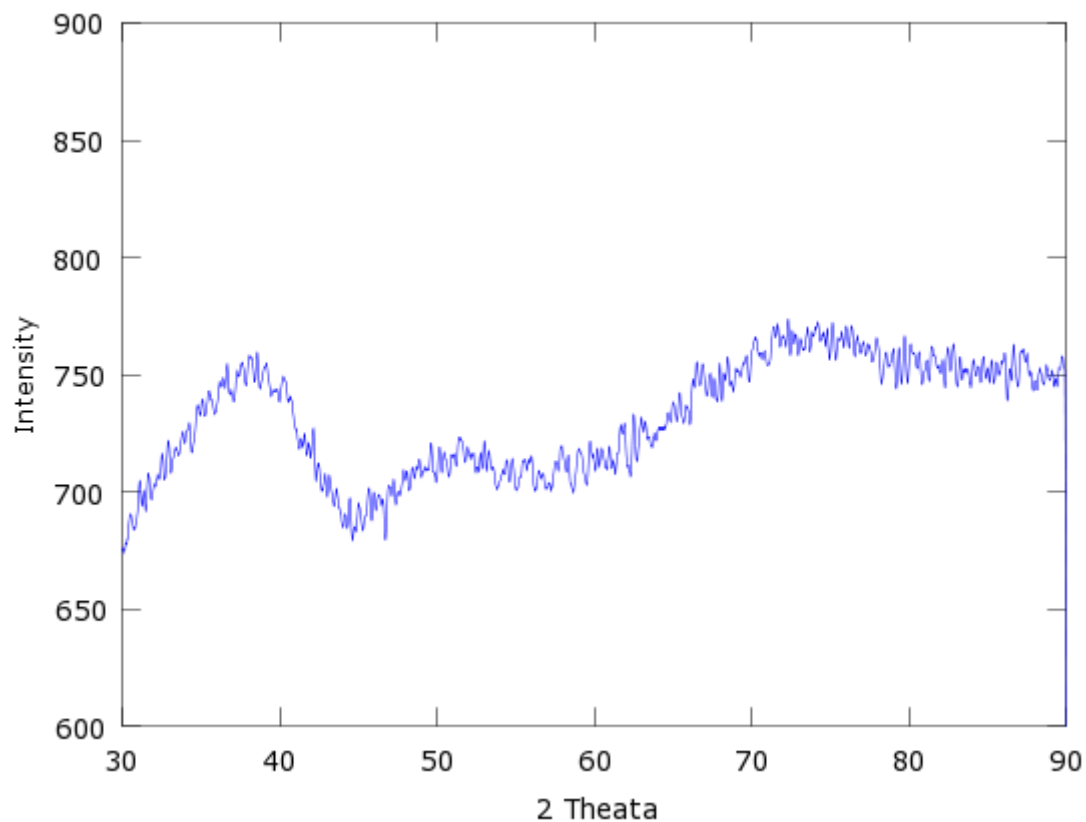


Figure 3.2. XRD spectrum of co-precipitation method citric acid coated nanoparticles.

Attempts to recrystallize the nanoparticle were made in order to try to improve the X-ray diffraction pattern. (Figure 3.3) The theory was by heating the citric acid coated nanoparticles in diphenyl ether to 270°C the magnetite would realign itself and form the desired Fd3m crystal lattice. This would cause the XRD pattern to display a better diffraction pattern to verify magnetite formation. Adding oleic acid and oleylamine to replace the citric acid which would melt at high temperatures allowed a surfactant to be present to prevent aggregation and formation of larger particles.

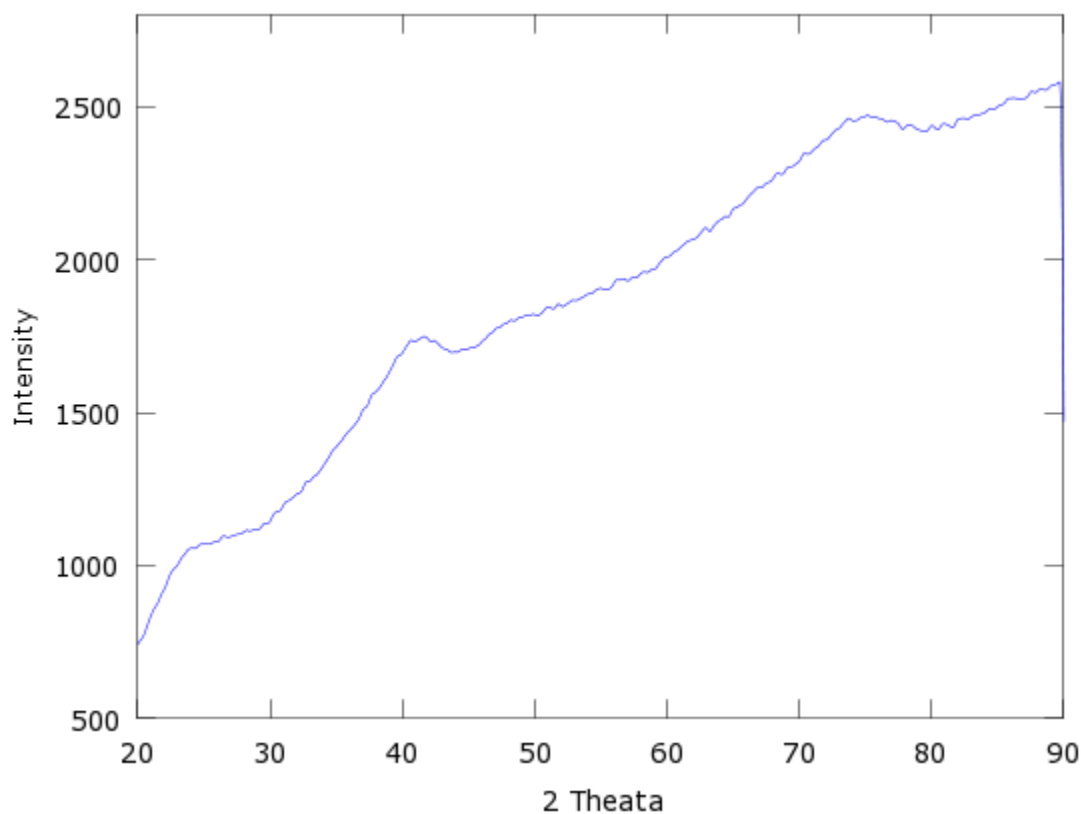


Figure 3.3. XRD spectrum of co-precipitation NPs after recrystallization attempt.

The XRD spectrum of the co-precipitated nanoparticles without recrystallization attempts has few peaks from diffraction. The spectrum resembles background noise. For the XRD spectrum for recrystallization three “humps” begin to form. These show a potential crystal formation of magnetite but the diffraction peaks are too broad to characterize the nanoparticles using XRD. Both of these spectra do show the amorphous nature of the nanoparticles and validate the non-paramagnetic properties associated with these nanoparticles. If the magnetite has not formed its expected $Fd3m$ cubic lattice then the unpaired electrons will not align under an external magnetic force to create their own magnetic moment.

3.1.4 TEM Studies

Transmission electron microscopy images were the only method available during this research project to calculate nanoparticle size for co-precipitation nanoparticles. Co-precipitation nanoparticles often vary in size and shape. This was observed in the TEM images, but not to the extent expected. 16:84 europium doped iron oxide nanoparticles displayed a generally spherical shape and narrower size distribution than anticipated. (Figure 3.4)

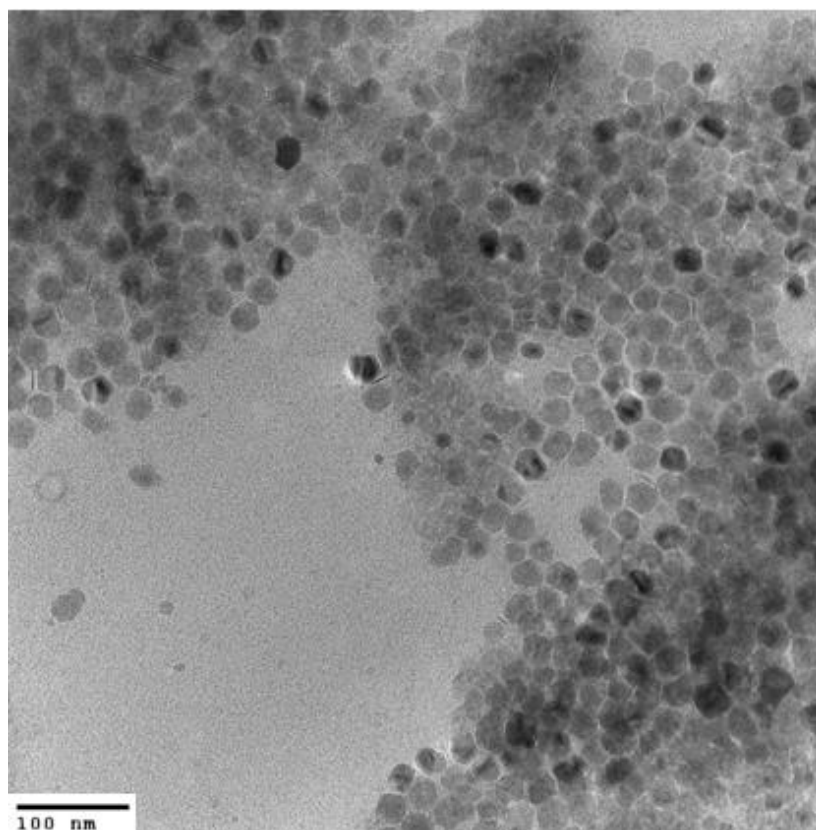


Figure 3.4. TEM image of 16:84 co-precipitation NPs surface coated with citric acid.

Measuring the average nanoparticle size from the TEM image, an average nanoparticle size of 29 ± 5 nm was obtained. Sizes seen in the images ranged from just a

few nanometers, small fragments, to as large as 36 nm. A size distribution graph shows the range and frequency of measured nanoparticles from the images. (Figure 3.5) These nanoparticles were surfaced coated with TTA.

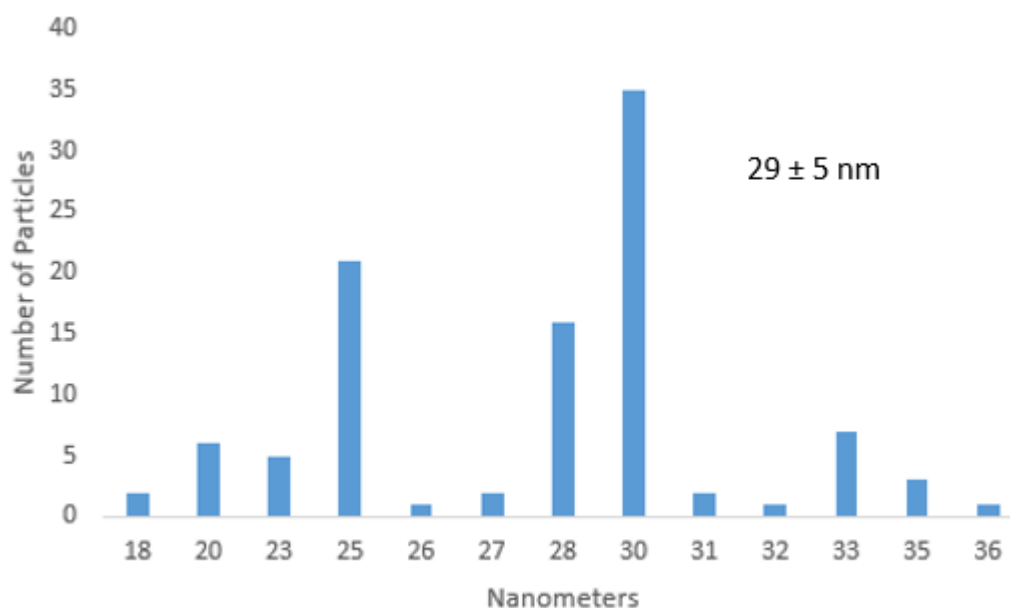


Figure 3.5. Size distribution of 16:84 co-precipitation NPs.

TEM images of citric acid coated nanoparticles were acquired for 20:80 molar doping as well. The images show a similar size distribution, although differences are to be expected with the nature of the co-precipitation method. (Figure 3.6) An average size of approximately 13 -15 nm was seen for these nanoparticles with a generally spherical shape as seen with 16:84 doping ratio.

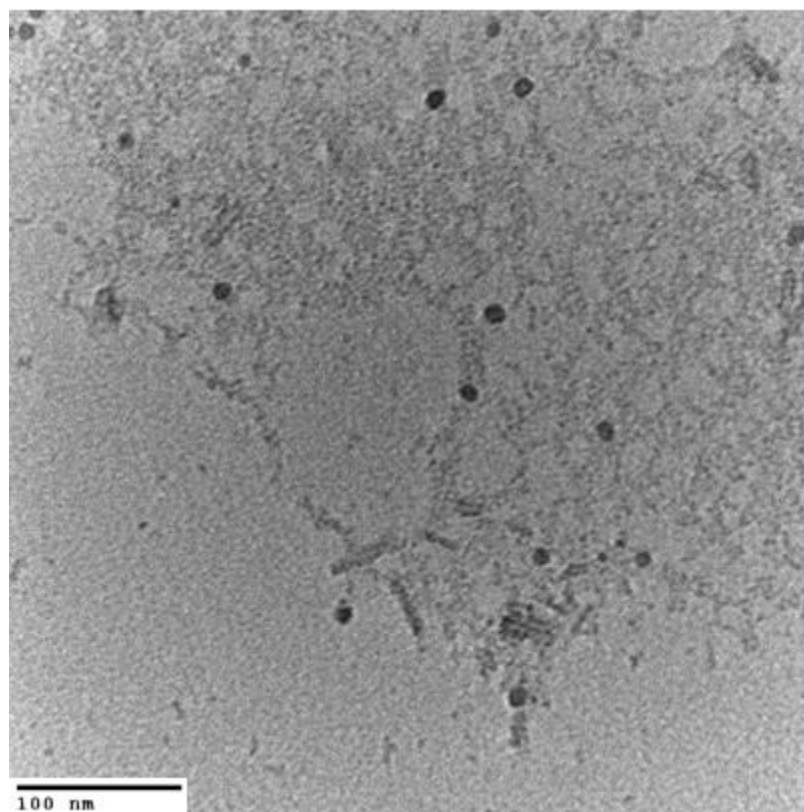


Figure 3.6. TEM image of 20:80 co-precipitation NPs surface coated with citric acid.

3.1.5 FT-IR Studies of Co-Precipitation Nanoparticles

FT-IR spectroscopy was used to verify nanoparticle formation during various stages of synthesis. Since XRD could not be used to determine if iron oxide nanoparticles had formed, other methods such as FT-IR and UV-Vis were used to characterize nanoparticle formation. FT-IR was used mainly to observe the surface coatings of the nanoparticles. FT-IR was performed on citric acid coated nanoparticles as well as TTA-coated nanoparticles to ensure that the ligand exchange had occurred. FT-IR spectra of dried powder reactants were compared. (Figure 3.7A)

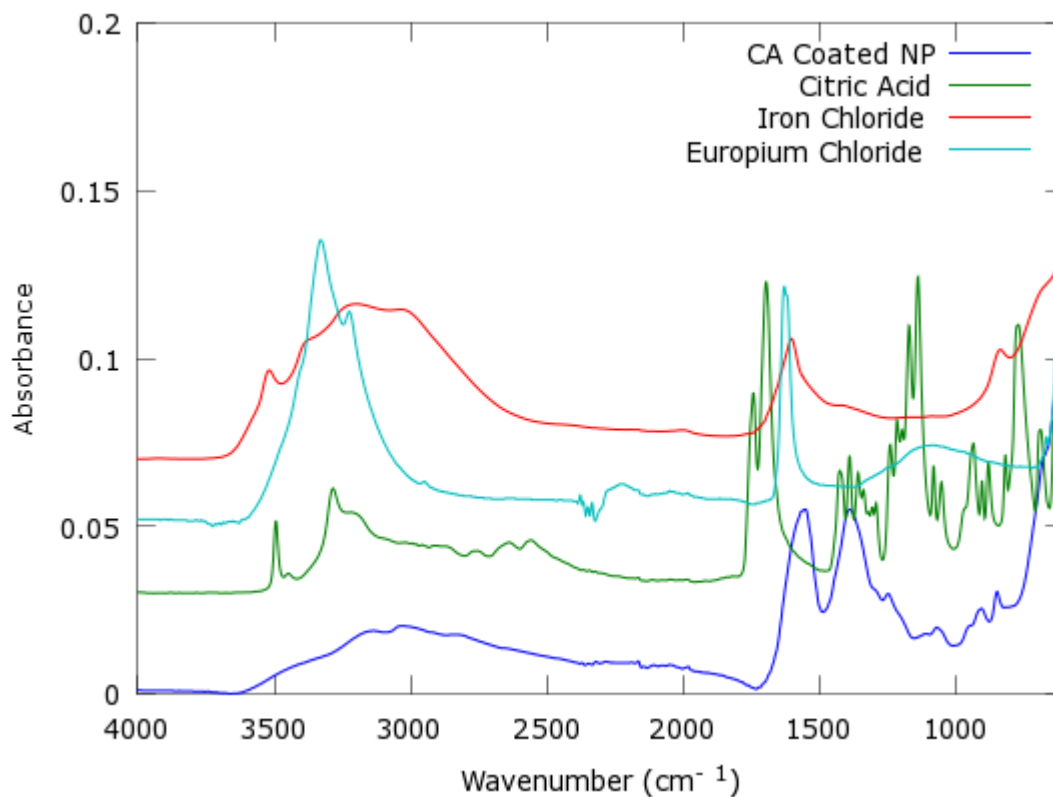


Figure 3.7 [A] FT-IR spectra of starting reagents and co-precipitated NPs.

These spectra confirm the surface coating of the nanoparticles with citric acid. Only those peaks associated with citric acid remain after synthesis of the nanoparticle. Characterizing the nanoparticle with FT-IR to confirm the presence of citric acid is possible through confirming the presence of the carbonyls (C=O) at the peaks 1742 cm⁻¹ and 1697 cm⁻¹ for free citric acid. These peaks become one broader peak when coordinated with the magnetite nanoparticle and shift to 1560 cm⁻¹. (Figure 3.7B)

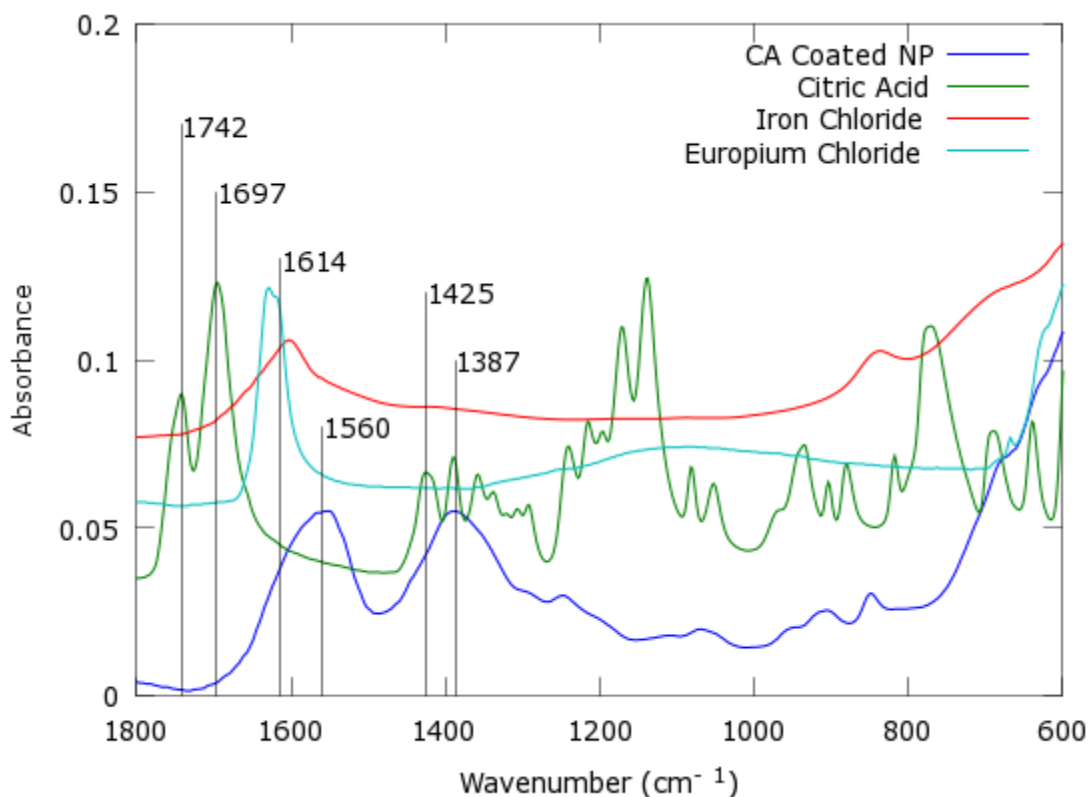


Figure 3.7 [B] $600\text{ cm}^{-1} - 1800\text{ cm}^{-1}$ region of FT-IR spectrum of starting reagents and co-precipitated nanoparticles.

This shift is due to the reduced bond strength of the carboxylate ion after coordination with the nanoparticle. The split peaks in citric acid is due to the mechanical interaction between the stretching modes of the carbonyl groups¹⁹. Stretching due to C-O interaction and C-O-H in plane bending is seen in free citric acid as two peaks, 1425 cm^{-1} and 1387 cm^{-1} , and in the citric acid coated nanoparticles, 1387 cm^{-1} . This also has become one broad peak for the citric acid coordinated with the nanoparticle due to weakening the bond through loss of resonance with coordination. Frequency shifts observed confirm co-precipitation nanoparticles are surface coated with the surfactant citric acid. For the

reactants, iron and europium chloride, there is a peak at 1614 cm^{-1} due to O-H bending. The sharper peak associated with europium chloride is due to its more crystalline nature.

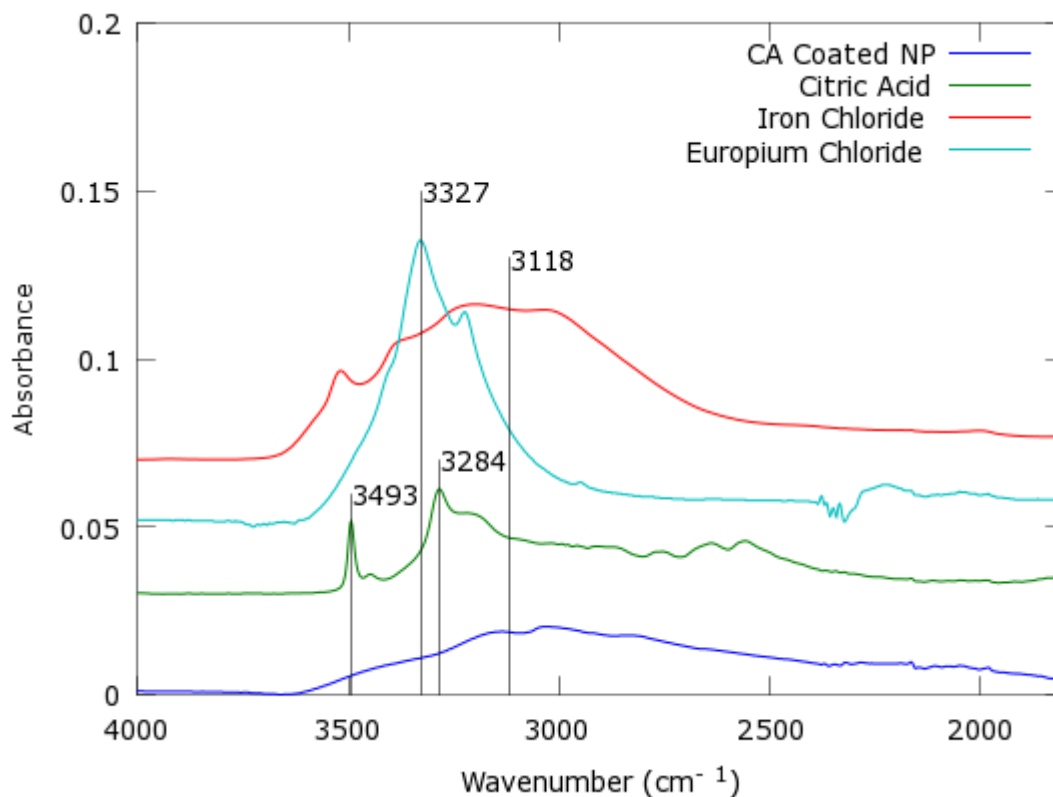


Figure 3.7 [C] $1800\text{ cm}^{-1} - 4000\text{ cm}^{-1}$ region of FT-IR spectrum of starting reagents and co-precipitated nanoparticles.

Above 1800 cm^{-1} in the FT-IR spectrum there are broad O-H stretching peaks due to water at 3318 cm^{-1} and 3327 cm^{-1} which is coordinated with iron and europium respectively in the starting materials. (Figure 3.7 C) The O-H peak of iron chloride is broad due to the amorphous nature of iron chloride. Europium chloride is more crystalline and has a narrower O-H peak. There are also alcohol peaks seen in free citric acid at 3493 cm^{-1} for the carboxylic acid groups O-H stretching. The second O-H frequency for citric acid

is seen at 3284 cm^{-1} . This is from the alcohol group not a part of a carboxylic acid. The co-precipitated nanoparticles there is a broad weak absorption due to O-H stretching.

The next step of the procedure was the ligand exchange process in which citric acid is exchanged for TTA. Dried powders of free TTA and TTA surface coated nanoparticles FT-IR spectra were compared to ensure proper TTA coordination. (Figure 3.8 A)

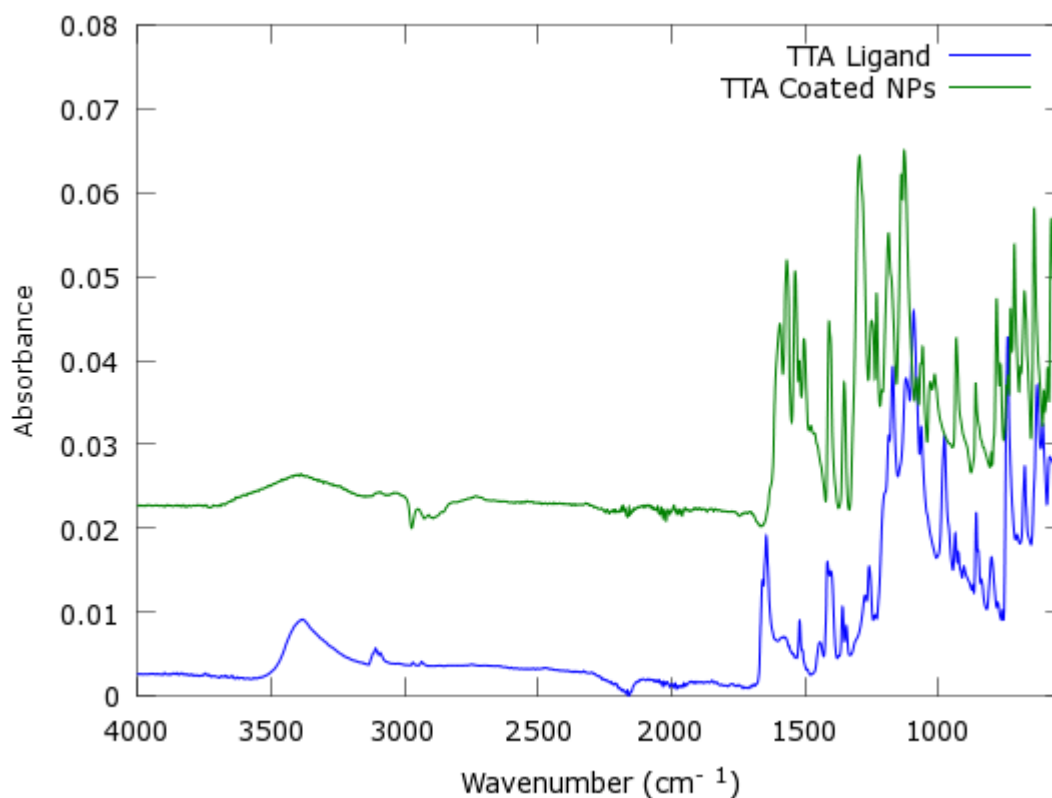


Figure 3.8 [A] FT-IR spectra of free TTA and TTA coordinated nanoparticles.

In the $600\text{ cm}^{-1} - 1800\text{ cm}^{-1}$ region of the spectra there are peaks due to the ring structure of TTA. (Figure 3.8 B) A splitting pattern for the rings causes multiple peaks. For free TTA the peak at 1647 cm^{-1} is due to this carbonyl (C=O) stretching. This peak shifts when coordinated with the nanoparticle, to 1547 cm^{-1} . The halogen species trifluorene has

a frequency at 1091 cm^{-1} in free TTA. When bound to iron oxide this peak does shift up field to 1121 cm^{-1} . A splitting pattern for both spectra can be seen from 1420 cm^{-1} to 1200 cm^{-1} due to the sulfur containing ring. Monosubstituted aromatic rings display a band pattern of this nature dependent on the substituents¹⁹. The frequency of these peaks confirm the presence of TTA surface coating the nanoparticle and replacing citric acid in the ligand exchange program.

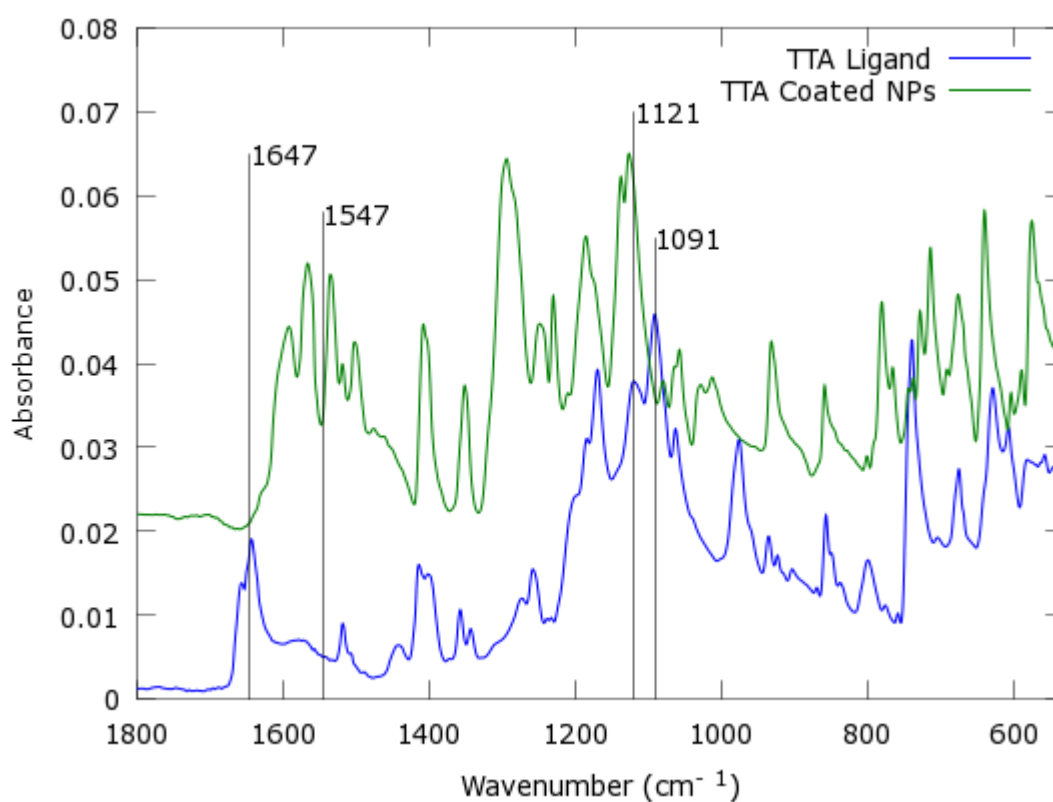


Figure 3.8 [B] $600\text{ cm}^{-1} - 1800\text{ cm}^{-1}$ region of FT-IR spectra of free TTA and TTA coordinated nanoparticles.

From 1800 cm^{-1} to 4000 cm^{-1} wavenumbers there are few peaks present. A weak peak at 3110 cm^{-1} due to C-H stretching from the sulfur containing ring structure is seen in

both spectra. C-H stretching at the carbonyl in both spectra has a frequency of 3394 cm^{-1} . (Figure 3.8 C)

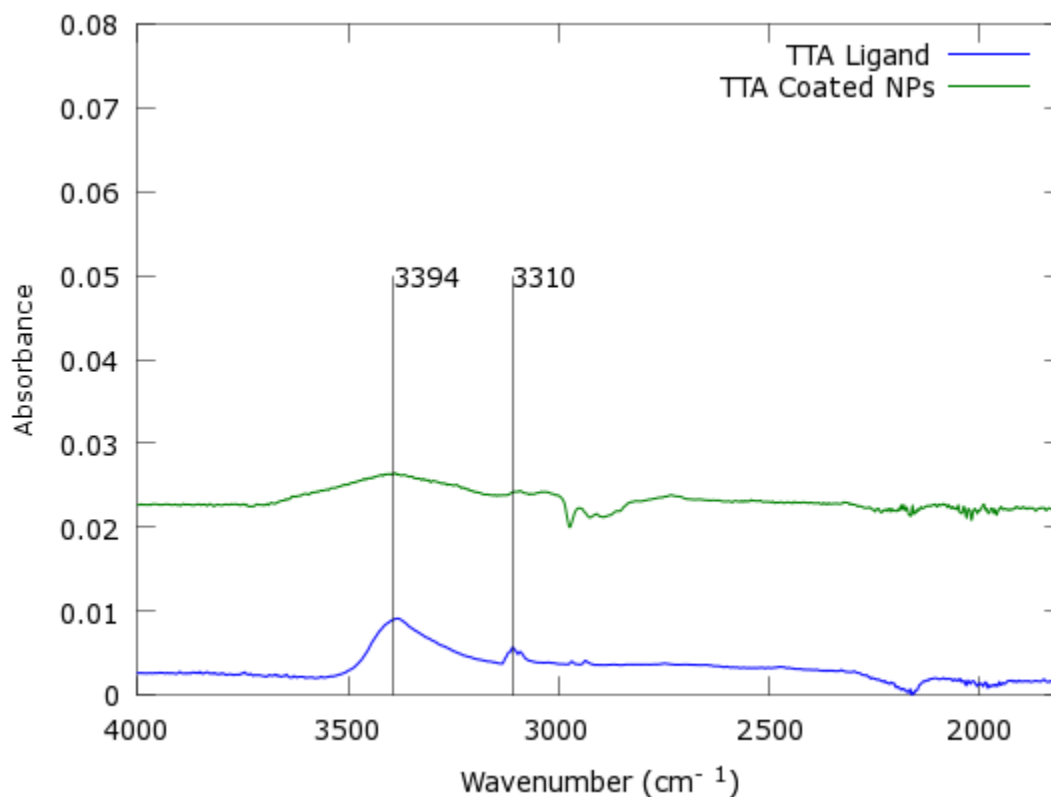


Figure 3.8 [C] $1800\text{ cm}^{-1} - 4000\text{ cm}^{-1}$ region of FT-IR spectra of free TTA and TTA coordinated nanoparticles.

3.1.6 Determining Actual Concentrations of Europium Doping

Inductively coupled plasma – optical emission spectroscopy was used to determine the amount of europium actually doped into the crystal lattice of magnetite. Theoretical levels of doping were 16, 20, 30, and 40 percent europium as part of the nanoparticle structure. Actual levels of doping were approximately half of theoretical. For 16:84

europium to iron there was an actual doping ratio of 8.32:91.68 europium to iron respectively. The same trend was seen for the remaining doping ratios. (Table 3.1)

Table 3.1. Actual levels of europium and iron calculated by ICP-OES

Theoretical Doping	Actual Europium Conc. (%)	Actual Iron Conc. (%)
16:84	8.32 ± 0.52	91.68 ± 0.52
20:80	8.92 ± 0.40	91.18 ± 0.40
30:70	13.97 ± 0.37	86.03 ± 0.37
40:60	18.32 ± 0.19	81.98 ± 0.19

Performing ICP-OES proved that europium had become incorporated into the nanoparticle and that europium was present. It also proved that varying the synthesis molar ratios of iron chloride and europium chloride increased the percentage of europium present in the nanoparticle structure. (Figure 3.9)

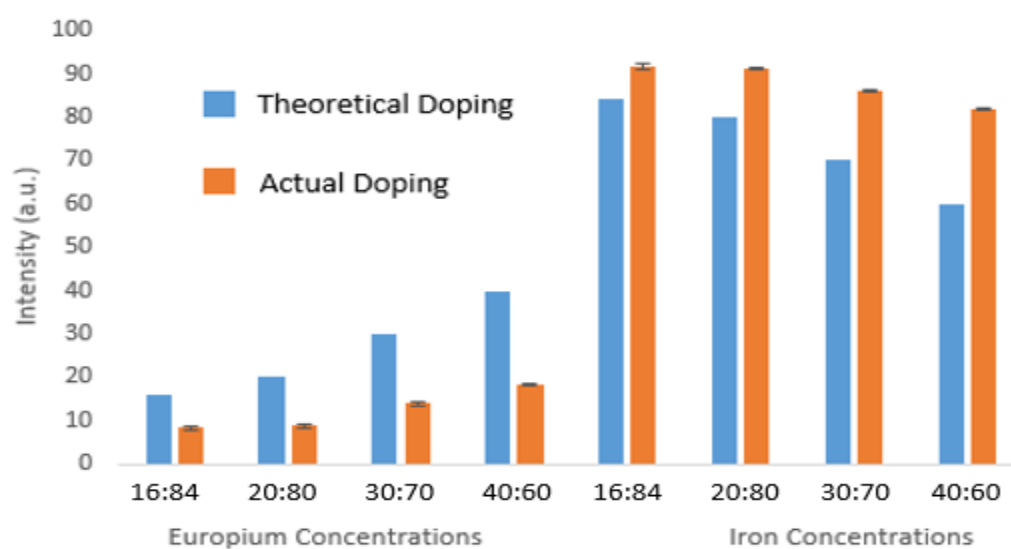


Figure 3.9. Bar graph of actual europium and iron concentrations versus theoretical doping percentage.

3.2 THERMALLY DECOMPOSED Eu:Fe₃O₄ NANOPARTICLES

3.2.1 *Synthesis and Crystal Lattice Formation*

Generally, thermal decomposition methods involve an iron precursor decomposing in a high temperature solvent in the presence of a stabilizing surfactant such as trioctylamine, oleic acid, or oleylamine²⁰. A reducing agent must be added to create the correct stoichiometric ratio of 2:1 Fe²⁺:Fe³⁺ for magnetite formation. Thermal decomposition of iron precursors in air creates hematite, Fe₂O₃. In an inert environment, such as argon or nitrogen, magnetite forms. Decomposition in a gas atmosphere dominated by their own conversion gases have been shown to proceed via magnetite and cementite, to wüstite and metallic iron with a continuing increase in temperature. Magnetite crystallizes in the spinel structure with ferrous and ferric ions on the octahedral sites of the spinel lattice. The crystal lattice formed is a space group Fd3m with a lattice constant of 8.39 Å²¹. Magnetite crystal lattices form octahedral and tetrahedral sites within their structure. Eight Fe³⁺ ions in the tetrahedral sites and eight Fe²⁺ and Fe³⁺ in octahedral sites within the unit cell²². This mixed valency in different sites within the unit cells, along with the unpaired electrons in oxygen, create the paramagnetic properties associated with magnetite. The high temperature thermally decomposed nanoparticles synthesized for this research appear to be highly magnetic when checked against a neodymium magnet. Increased doping with europium to forty percent did decrease the nanoparticles magnetic properties however, though only slightly.

During synthesis, with the non-polar solvent selected for this synthesis, the water present in $\text{Eu}(\text{btfa})_3(\text{H}_2\text{O})_2$ acted as an azeotropic mixture while initially refluxing the nanoparticles during thermal decomposition. Due to this effect during refluxing, the water had to be removed in a separate step through a vacuum line in an initial heating step. The amount of nanoparticles synthesized in this method was very small. During each step of surfactant removal fewer nanoparticles were recovered for procession to the next step. The same change in color during coordination with TTA was not seen as with the low temperature co-precipitation nanoparticles, possibly due to the low concentration of nanoparticles available for surface coordination.

3.2.2 X-ray Powder Diffraction Studies

The europium doped magnetite nanoparticles were characterized using XRD to determine the crystal lattice structure of magnetite had formed. XRD spectra showed a crystal lattice structure similar to that of magnetite with slight shifts in 2θ values. This may be caused by the europium doping into the crystal lattice resulting in slight deformations in the $\text{Fd}3\text{m}$ crystal structure. Diffraction peaks at 2θ values of 29, 32, 41, 54, and 65 correspond to hkl values of (220), (311), (400), (511), and (440) respectively. (Figure 3.10) This XRD spectra is for 16:84 doped nanoparticles. Using a modified version of the Scherer equation an average crystalline length of 8 nm was calculated²⁰. Normally the Scherer equation focuses on the prominent diffraction peak in a spectrum to calculate crystalline length. With the modified version all diffraction peaks are compared to give a more accurate average length. This calculation can be used to calculate average nanoparticle size as well. The modified version of the Scherer equation is given in Equation 2.

$$e^{\ln(K\lambda/L)} = K\lambda/L \quad \text{Eqn. 2}$$

For the equation K is taken to be a constant. This constant has values ranging from 0.62 – 2.082. For spherical nanoparticles the K constant is typically 0.89. That was the value used for crystalline length calculations. Lambda is the wavelength of the x-ray source being used, which is a $K\alpha_1$ wavelength.

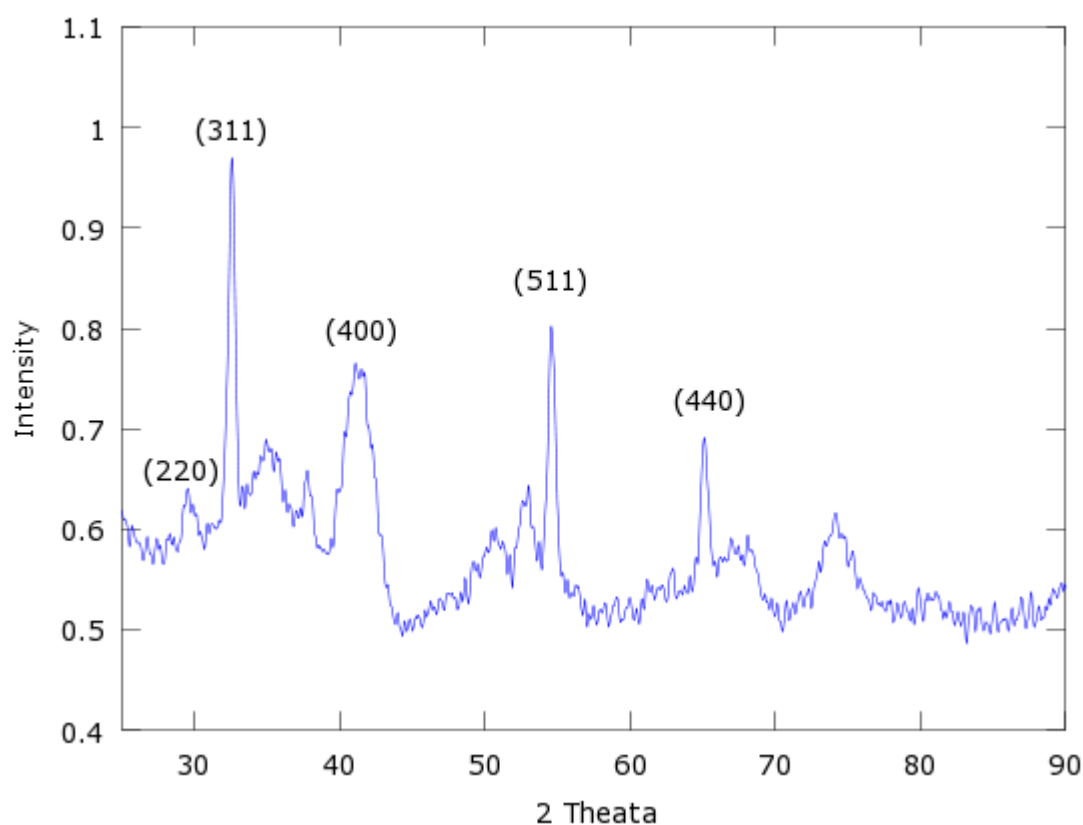


Figure 3.10. XRD diffraction pattern for 16:84 high temperature nanoparticles.

With increased doping of europium to 40:60 nanoparticles the magnetite crystal structure diffraction pattern was still present in the XRD spectrum. (Figure 3.11) The values shifted slightly more than with the 16:84 doped nanoparticles. This again may be

due to increased doping levels. The modified Scherrer equation was again used to calculate the average crystalline length. This was determined to be 36 nm.

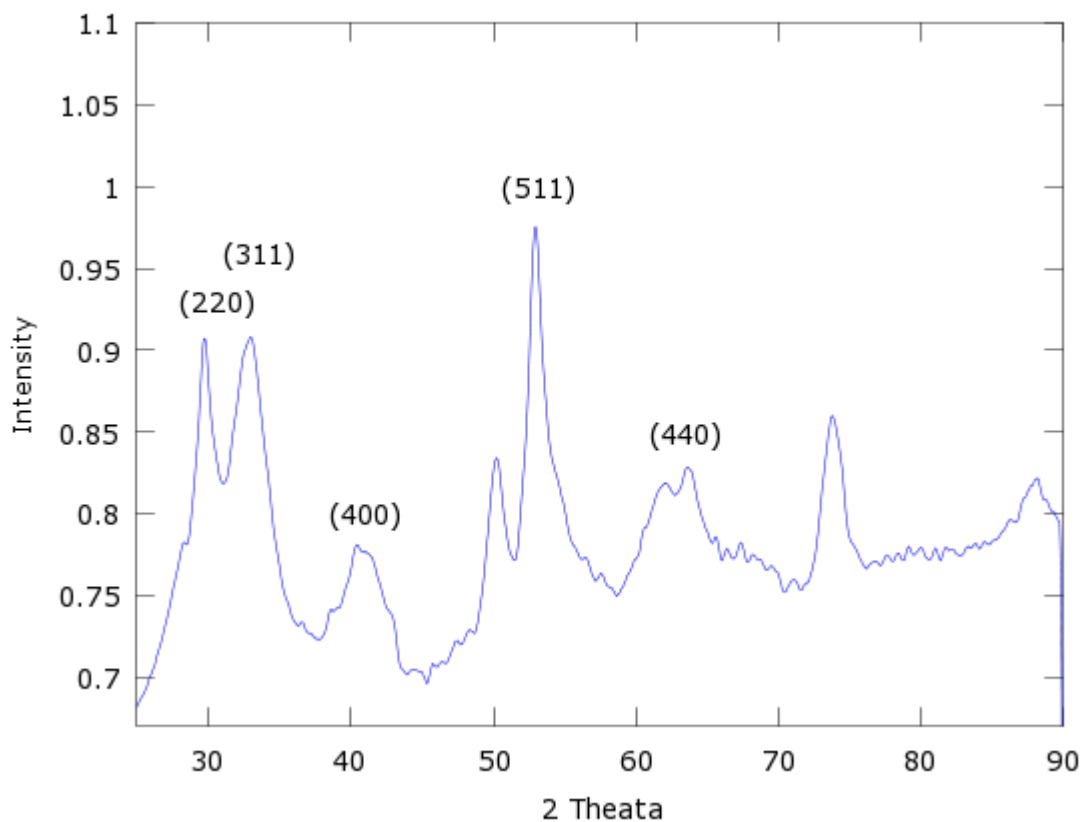


Figure 3.11. XRD diffraction pattern for 40:60 high temperature nanoparticles.

3.2.3 TEM Studies

Transmission electron microscopy images show a uniform size and shape distribution for the thermally decomposed nanoparticles. For 16:84 nanoparticles the average nanoparticle size was calculated to be 8 ± 3 nm with the TEM image. (Figure 3.12) This is in close agreement with the Scherrer equation calculation of 8 nm. In comparison to the co-precipitation nanoparticle average size of 29 ± 5 nm this is not as great a difference

as expected. There were fewer fragments and a narrower size distribution with the high temperature nanoparticles.

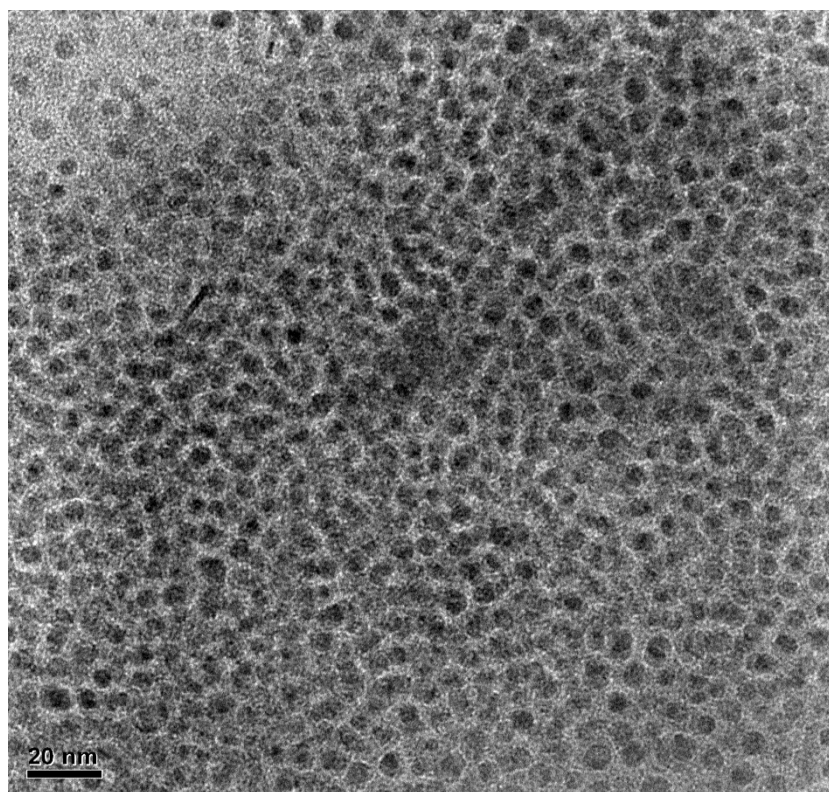


Figure 3.12. TEM image of 16:84 high temperature nanoparticles.

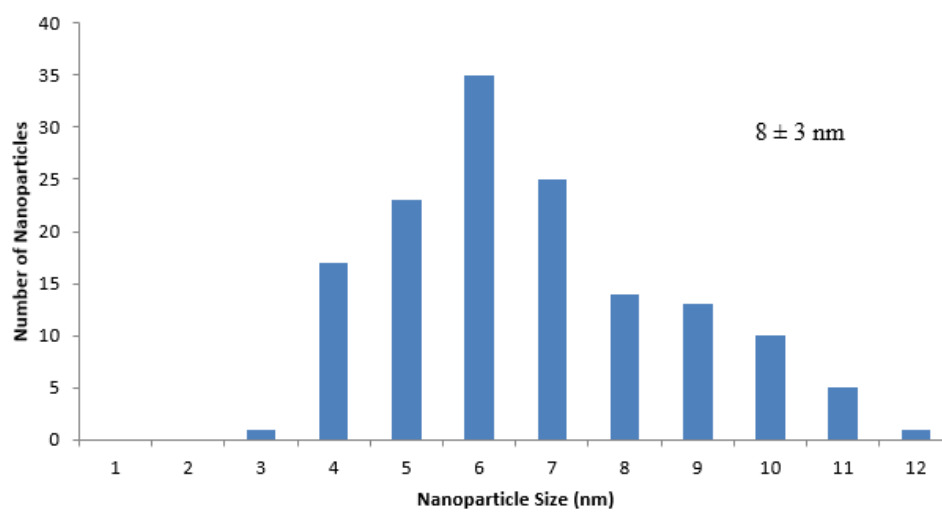


Figure 3.13. 16:84 high temperature nanoparticle size distribution calculated from TEM image.

Sizes ranged from 3 nm to 12 nm as shown in the TEM. (Figure 3.13) Another element shown in TEM is the presence of crystal lattice lines. (Figure 3.14) These crystal lattices were not visible in the low temperature method due to the amorphous nature of the nanoparticles. The occurrence of these crystal lattice lines and the XRD diffraction pattern prove that magnetite is formed during synthesis. The faint lines in the TEM image are the crystal lattices of magnetite.

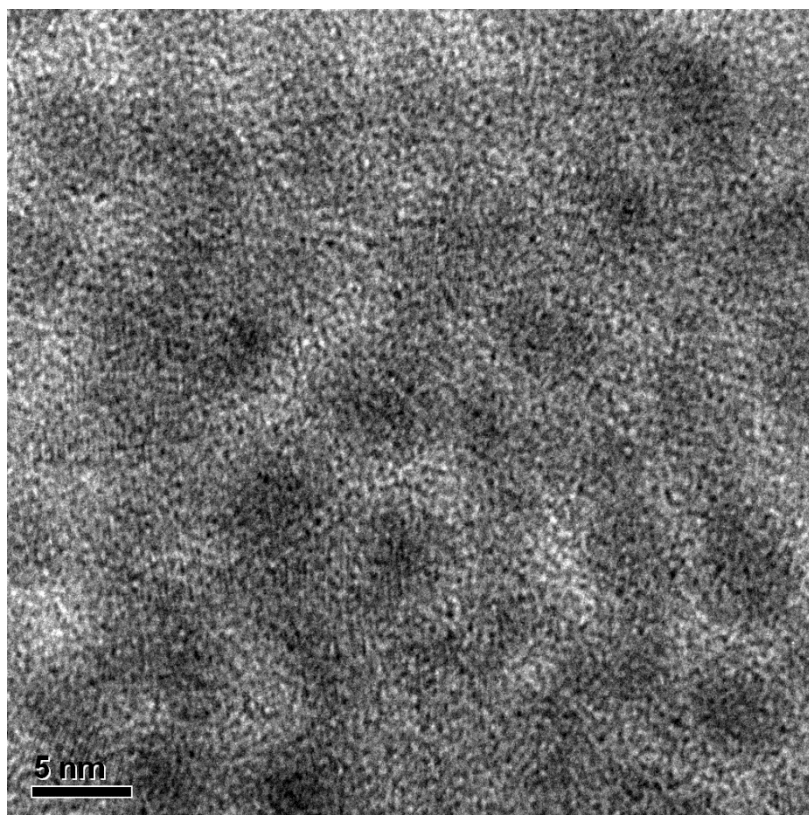


Figure 3.14. 16:84 high temperature nanoparticles crystal lattice lines.

For the 40:60 doped nanoparticles a similar uniformity in size and shape is observed. For both doping values the nanoparticles appear to be fairly spherical. The

average nanoparticle size was calculated to be 17 ± 4 nm with the TEM image. (Figure 3.15) This is not within close agreement to the Scherrer equation calculation of 36 nm. This may in part be due to the low amount of sample used for XRD.

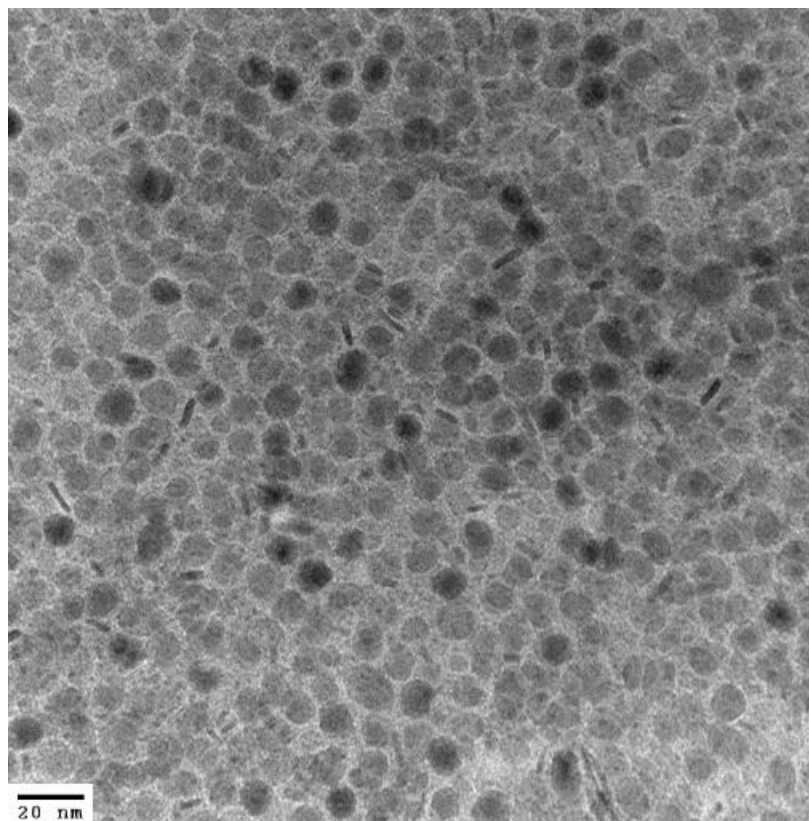


Figure 3.15. TEM image of 40:60 high temperature nanoparticles.

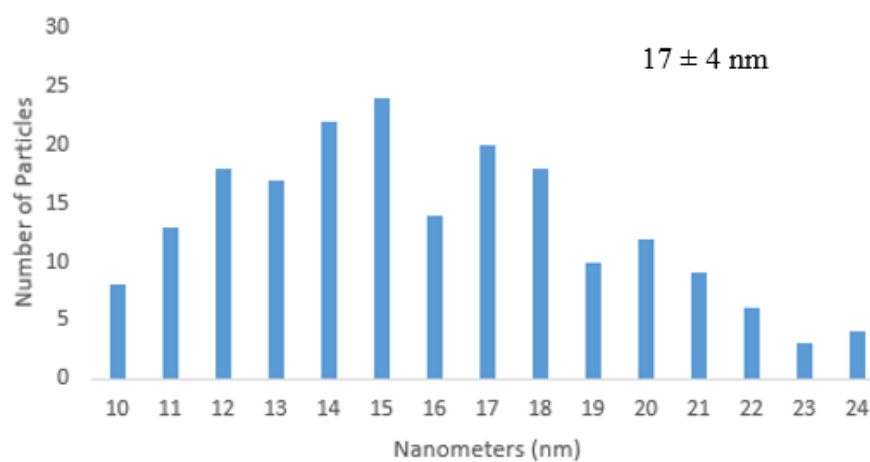


Figure 3.16. 40:60 high temperature nanoparticle size distribution.

3.2.4 FT-IR Characterization of High Temperature Nanoparticles

High temperature thermally decomposed nanoparticles were characterized using FT-IR to confirm the surfactant coating and removal. (Figure 3.17A) Comparing the FT-IR spectra of the surfactant, surfactant coated nanoparticles, and surfactant free nanoparticles the removal of the surfactant can be observed.

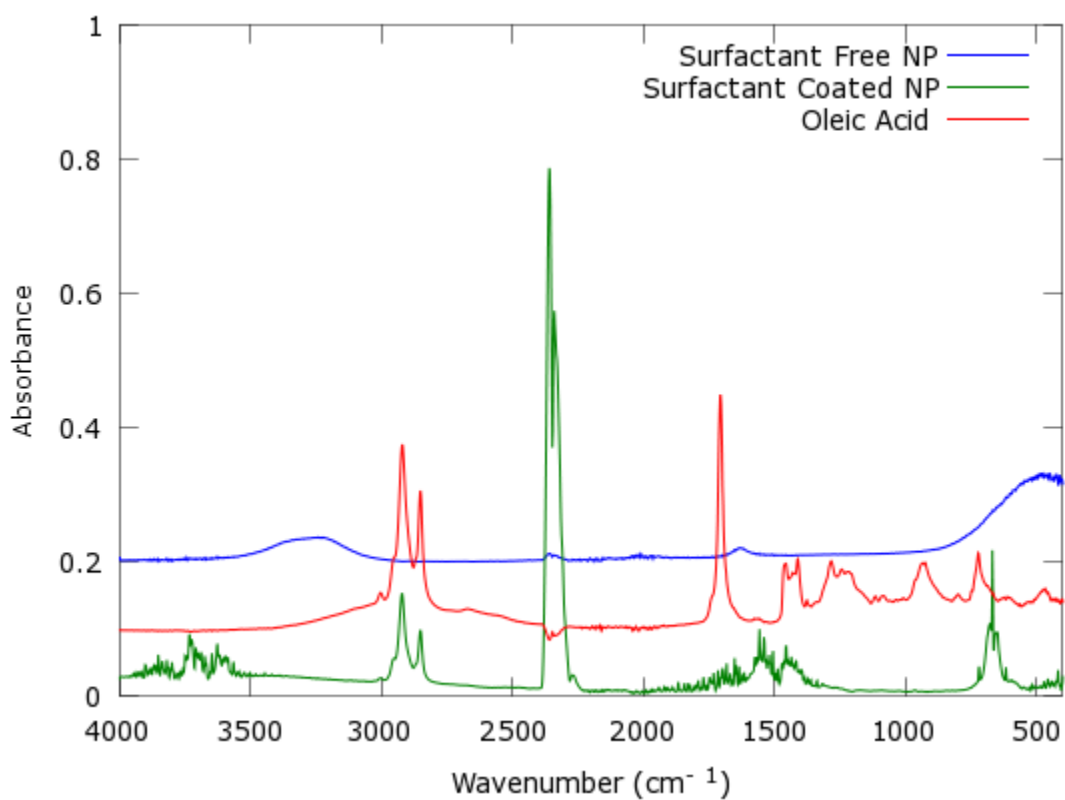


Figure 3.17 [A] FT-IR spectra of oleic acid, surfactant coated nanoparticles, and surfactant free nanoparticles.

With the surfactant coated nanoparticles, peaks associated with in plane rocking (C-H) 724 cm⁻¹ and bending (C-H) 937 cm⁻¹ is seen for oleic acid in the FT-IR spectra. At

1441 cm^{-1} asymmetrical bending of the methyl group (CH_3) is observed, along with a peak for the C-C-O-C stretching mode of the carboxylic acid in the oleic acid at 1258 cm^{-1} . A carbonyl peak (C=O) at 1701 cm^{-1} for carboxylic acid. This carboxylic acid has shifted up field to 1548 cm^{-1} when coordinated with the nanoparticle. There is also a peak with the surfactant coated nanoparticles at 670 cm^{-1} associated with the trifluoro group ($-\text{CF}_3$) from thermally decomposing $\text{Eu}(\text{btfa})_3(\text{H}_2\text{O})_2$. (Figure 3.17B)

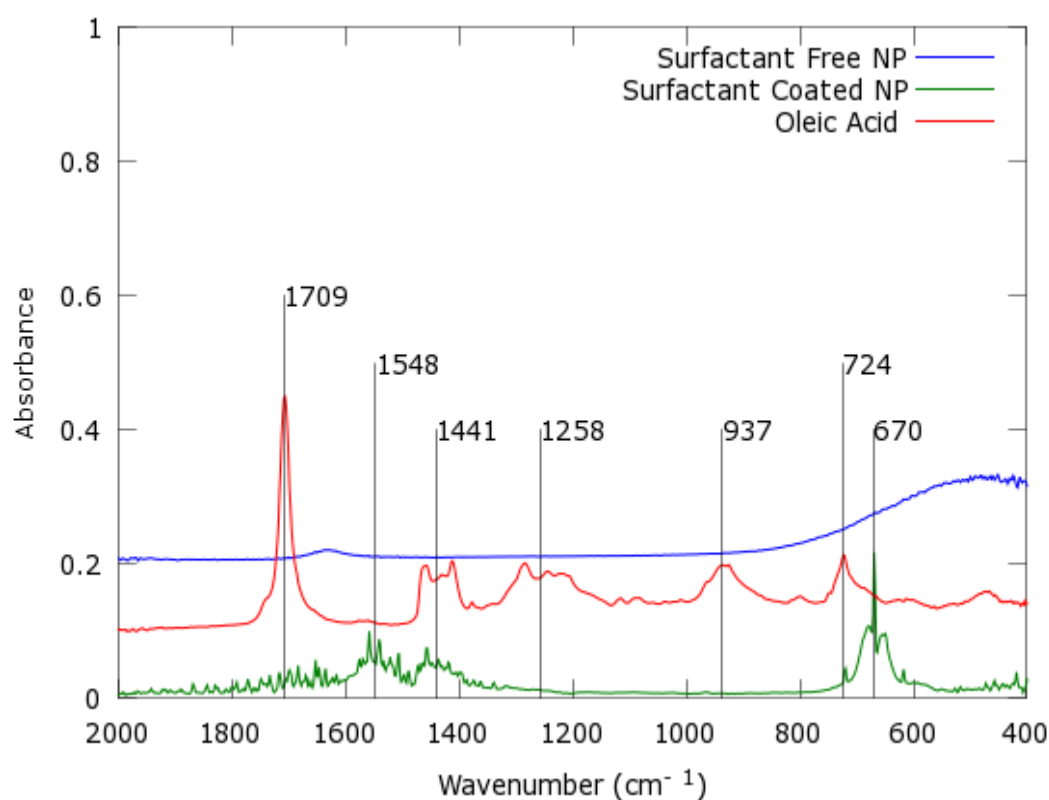


Figure 3.17 [B] 600 cm^{-1} – 1800 cm^{-1} region of FT-IR spectra of oleic acid, surfactant coated nanoparticles, and surfactant free nanoparticles.

In the 1800 cm^{-1} – 4000 cm^{-1} region of the FT-IR spectra there is a strong peak at 2347 cm^{-1} due to carbon dioxide (CO_2) in the atmosphere seen for the surfactant coated nanoparticles. Free oleic acid and surfactant coated nanoparticles show peak splitting at

2922 cm^{-1} and 2850 cm^{-1} . This is due to the methyl group (CH_3) of the surfactant with a downfield peak due to asymmetrical stretching and an up field peak at symmetrical stretching. For surfactant free nanoparticles there is a broad OH peak at 3300 cm^{-1} due to the nanoparticles being suspended in water. There is also weak peaks at 3664 cm^{-1} which comes from OH from residual water remaining from the $\text{Eu}(\text{btfa})_3(\text{H}_2\text{O})_2$. (Figure 3.17C)

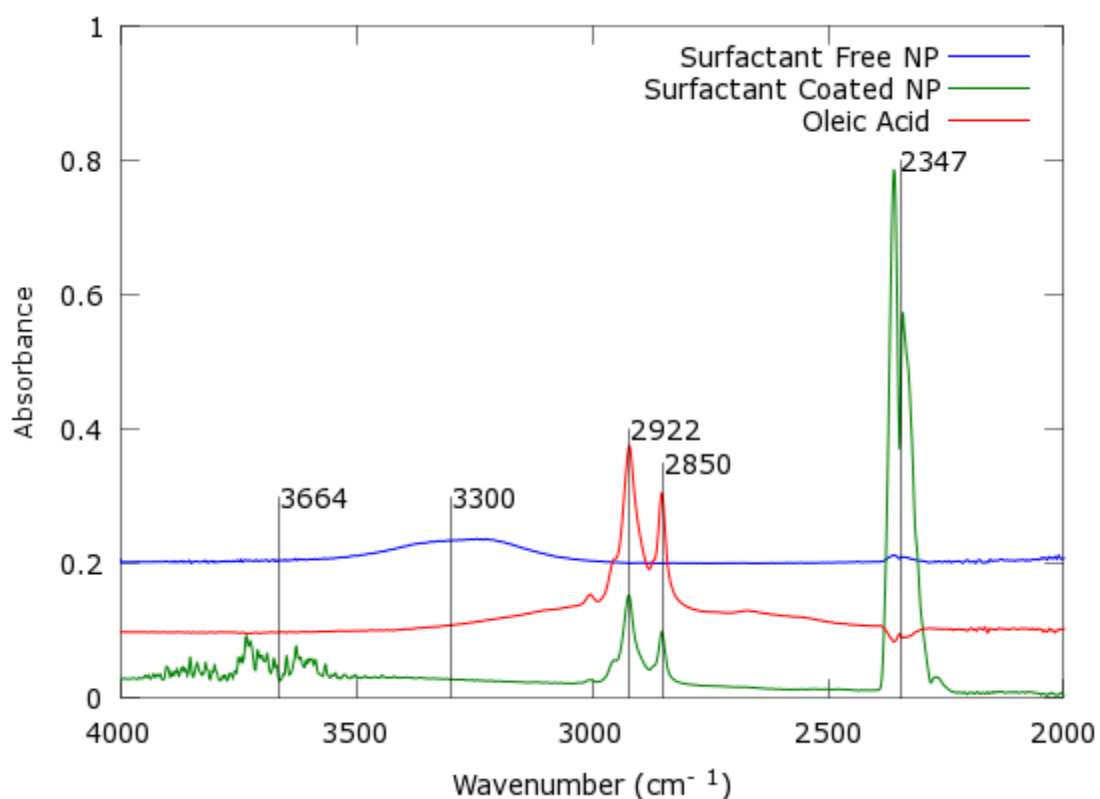


Figure 3.17 [C] 1800 cm^{-1} – 4000 cm^{-1} region of FT-IR spectra of oleic acid, surfactant coated nanoparticles, and surfactant free nanoparticles.

To confirm the trifluoro group peak present in the surfactant coated nanoparticles a FT-IR spectrum of $\text{Eu}(\text{btfa})_3(\text{H}_2\text{O})_2$ was performed. (Figure 3.18A) This confirms the presence of the trifluoro groups (CF_3). The groups have not been thermally decomposed

and their FT-IR absorption frequency is shifted from that found in the surfactant coated nanoparticles.

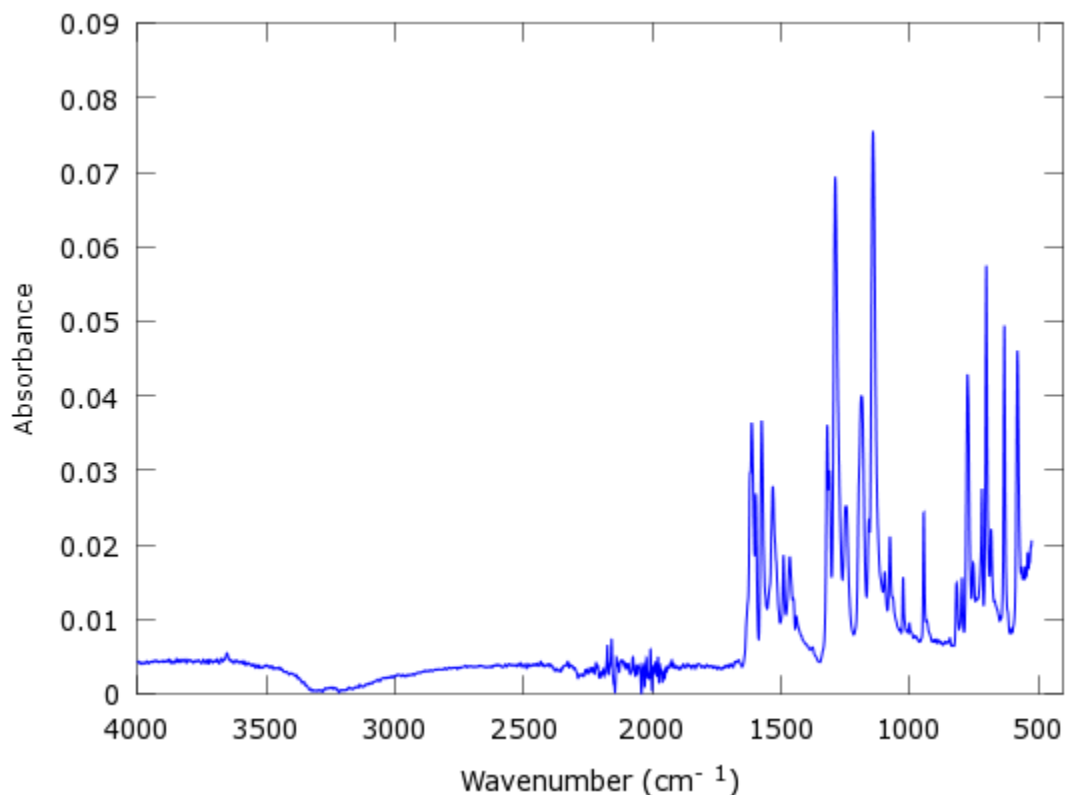


Figure 3.18 [A] FT-IR spectra of $\text{Eu}(\text{btfa})_3(\text{H}_2\text{O})_2$

In the $600\text{ cm}^{-1} - 1800\text{ cm}^{-1}$ region of the FT-IR spectrum for $\text{Eu}(\text{btfa})_3(\text{H}_2\text{O})_2$ a split carbonyl peak ($\text{C}=\text{O}$) at 1593 cm^{-1} due to coordination with the europium metal ion is seen. C-C-O-C stretching mode of the carboxylic acid in the Hbtfa coordinated with europium is seen at 1289 cm^{-1} . At 1142 cm^{-1} there is a peak due to the monosubstituted benzene ring. The trifluorene group (CF_3) is seen at 698 cm^{-1} , shifted to a lower wavenumber due to coordination with europium. (Figure 3.18 B)

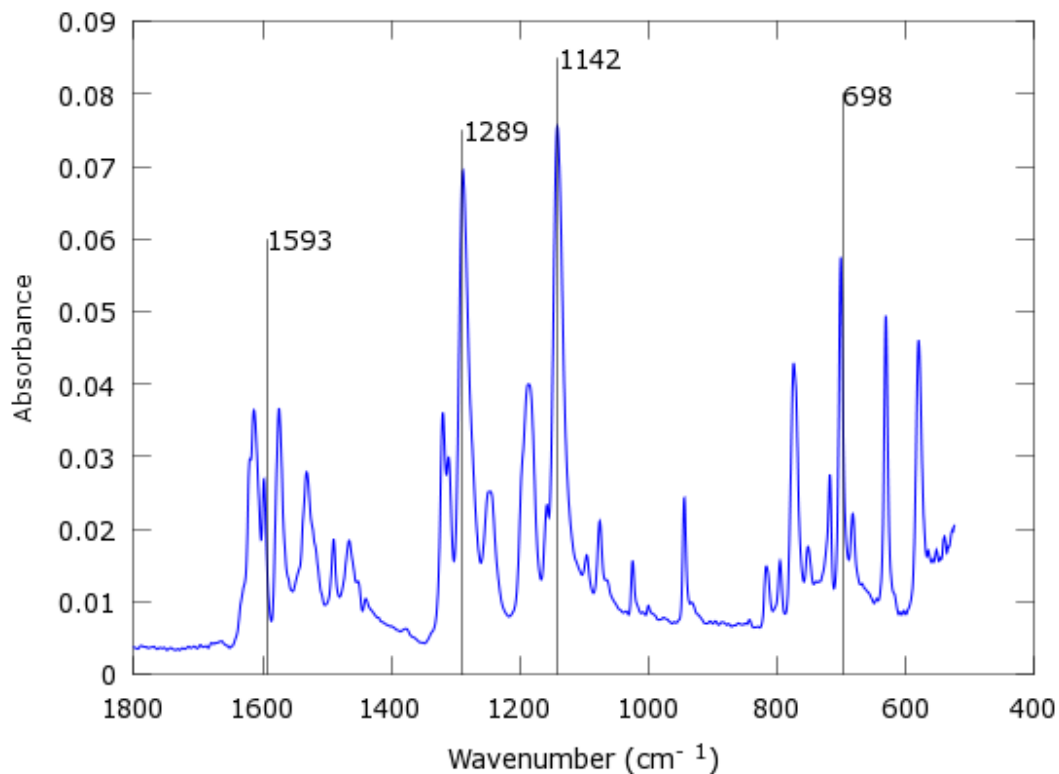


Figure 3.18 [B] 600 cm⁻¹ – 1800 cm⁻¹ region of FT-IR spectra of Eu(btfa)₃(H₂O)₂

The surfactants chosen for high temperature thermal decomposition was oleic acid and oleylamine. These had to be removed before coordination with TTA. Removing the surfactants from the nanoparticles proved to be difficult. Following a literature source the nanoparticles were first treated with an HCl solution of pH 3.5²⁴. This created water dispersible nanoparticles, but in small quantities. Using a Vernier caliber probe the pH was observed to increase from pH 3.5 to a higher pH value of 4.4. This proved the protonation process but the acidity was not remaining constant enough to continue surfactant removal.

A new method was developed using a citric acid buffer solution of pH 3.5 to continue protonation for a sustained period of time without an increase in pH. The citric acid buffer solution created a substantial amount of water dispersible nanoparticles. Coordination with the chromophore TTA proved unsuccessful. The TTA did not coordinate with the citric acid buffer treated nanoparticles alone. In both FTIR spectra of HCl treated and citric acid buffer treated the peaks associated with the surfactant are gone.

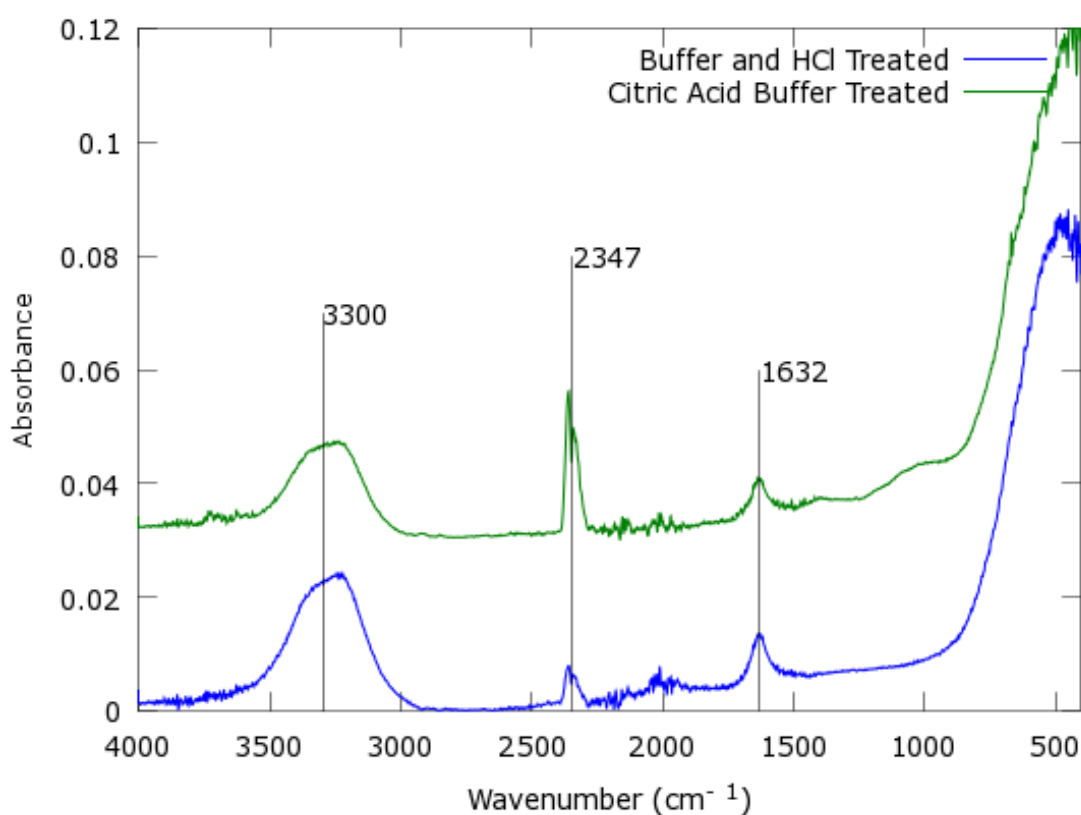


Figure 3.19 [A] FT-IR spectra of surfactant removal during acidic solution treatments.

Treating the nanoparticles in both a citric acid buffer and an HCl solution made nanoparticles available for coordination with TTA. (Figure 3.19A)

There is a broad OH peak due to nanoparticles being suspended in water at 3300 cm^{-1} . There is also a carbonyl stretch ($\text{C}=\text{O}$) at 1600 cm^{-1} due to citric acid coordinating to the surface of the nanoparticle. A carbon dioxide peak at 2342 cm^{-1} is seen again due to atmosphere. There are shoulders present in the spectra that contain hidden information as to why the coordination of TTA was unsuccessful.

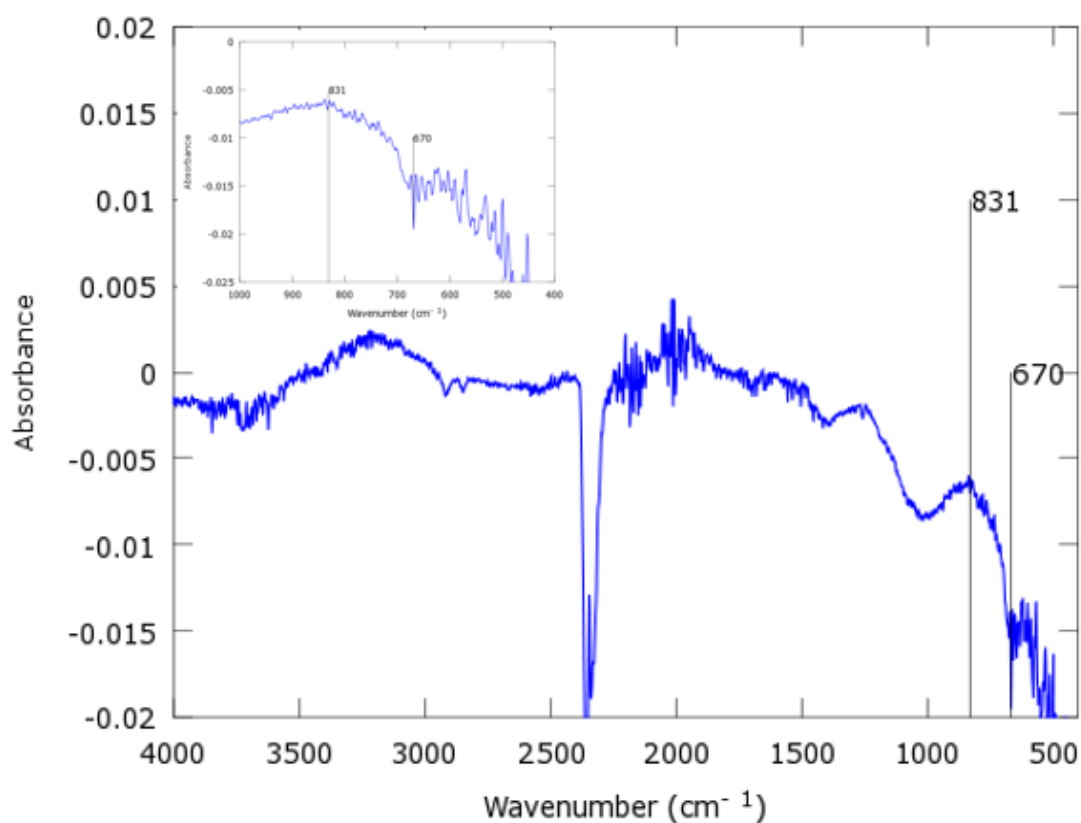


Figure 3.19 [B] FT-IR subtracted spectra of surfactant removal during acidic solution treatments

The two spectra were subtracted from one another with the carbonyl peak chosen to be the zero point when the two spectra were subtracted from one another. (Figure 3.19 B) The subtracted spectra shows trifluoro groups ($\text{O}-\text{C}-\text{CF}_3$) and ($-\text{CF}_3$) at peaks 831 cm^{-1} ,

and 670 cm^{-1} respectively. Published results using a similar trifluoro containing complex, coordinated with zinc shows a down field shift from 723 cm^{-1} to 712 cm^{-1} . Similar down field shifting is occurring here with the coordination to europium. During thermal decomposition the $\text{Eu}(\text{btfa})_3(\text{H}_2\text{O})_2$ complex decomposes and breaks into smaller molecules. Normally trifluoro containing molecules escape the reaction vessel in the form as a gas, this is why the reaction is performed under a fume hood. It is possible however that some of these thermally decomposed pieces are re-coordinating back to the surface of the nanoparticle and preventing the coordination with TTA.

A two part removal of oleic acid and oleylamine was done through a citric acid buffer solution and an HCl solution. The citric acid buffer acted to maintain an acidic condition during the entire treatment of the nanoparticles sustaining free H^+ ions to protonate the coordination site. After a treatment with the citric acid buffer solution a second treatment involving HCl facilitated the complete removal of any remaining surfactant and produced hydrophilic nanoparticles ready for coordination with TTA.

FT-IR was also performed to confirm the coordination of the organic chromophore TTA. Free TTA and TTA coordinated nanoparticles were compared to ensure the surface coating of the nanoparticles with TTA had occurred. (Figure 3.20 A)

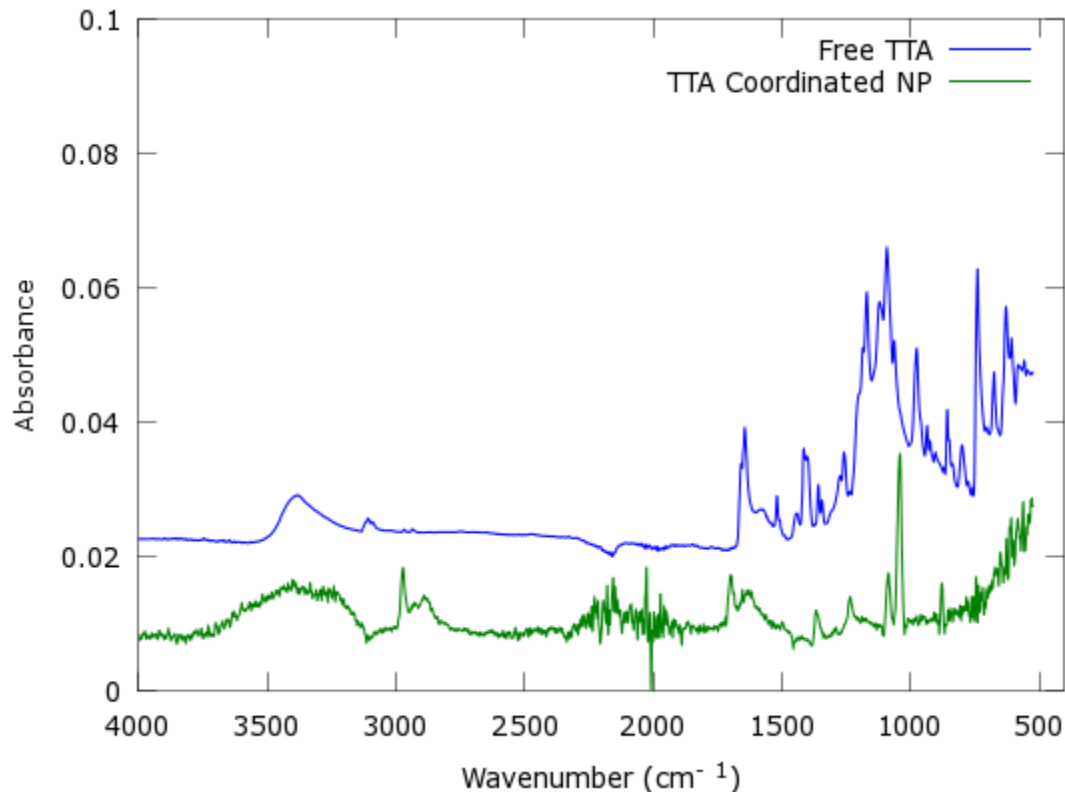


Figure 3.20 [A] FT-IR spectra of TTA and TTA coated high temperature nanoparticles.

The nanoparticle solution was very dilute but peaks can still be seen for C-H stretching at 3310 cm^{-1} for the sulfur containing ring. There is also a broad OH peak for TTA coated nanoparticles at 3381 cm^{-1} due to being suspended in ethanol/water. The trifluorene (CF_3) in free TTA is at 1091 cm^{-1} , and 1041 cm^{-1} when coordinated with the nanoparticle surface. There are carbonyl peaks ($\text{C}=\text{O}$) at 1639 cm^{-1} for free TTA and 1701 cm^{-1} for TTA coordinated with the nanoparticles. These peaks confirm the surface coordination with TTA. (Figure 3.20 B)

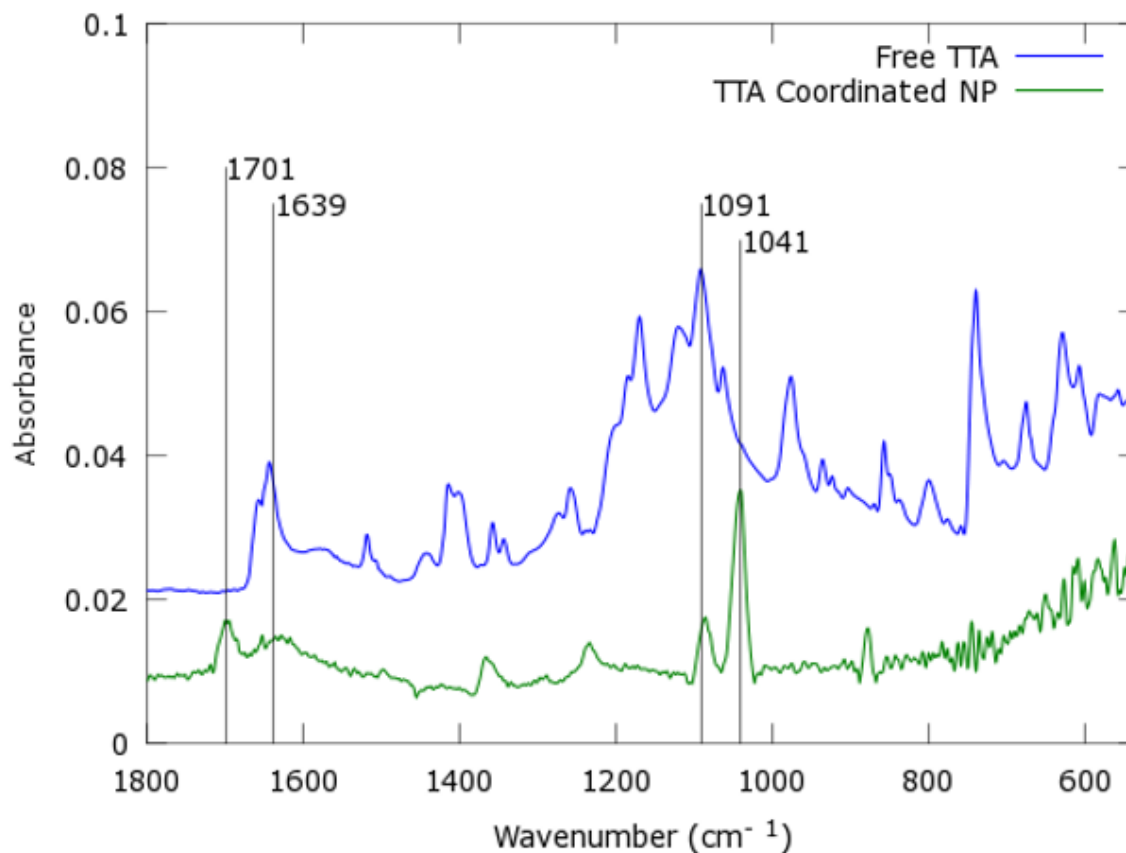


Figure 3.20 [B] $400\text{ cm}^{-1} - 1800\text{ cm}^{-1}$ region FT-IR spectra of TTA and TTA coated high temperature nanoparticles

3.2.5 Determining Actual Concentrations of Europium Doping for Thermal Decomposition

ICP-OES was performed on the two doping levels for nanoparticles synthesized by the high temperature thermally decomposed method. Identical standards were used for calibration curves, as well as wavelengths for iron and europium. Concentrations of europium were found to be very close to theoretical doping levels. (Table 3.2)

Table 3.2. Actual concentrations of iron to europium in high temperature nanoparticles.

Theoretical Doping	Actual Europium Conc. (%)	Actual Iron Conc. (%)
16:84	12.03 ± 0.62	87.97 ± 0.62
40:60	39.56 ± 0.21	60.44 ± 0.21

The results show actual doping percentages only slightly lower than the expected theoretical amounts. This shows the high efficiency of the reaction to dope europium into the magnetite crystal structure. With the low temperature co-precipitation method the actual doping levels of europium were calculated to be approximately half of theoretical doping. The co-precipitation method did not produce a crystalline product however, and this may be the reason for lowered europium doping levels. The defined crystal lattice of the high temperature nanoparticles facilitates doping more efficiently through replacing the iron more easily or by trapping europium into the crystal lattice.

3.3 CORE-SHELL NANOPARTICLES STRUCTURE AND SYNTHESIS

3.3.1 Core and Shell Synthesis

The magnetite cores for the core-shell nanoparticles formed in the same manner as the thermally decomposed nanoparticles. During synthesis a lanthanide source was removed to prevent doping the nanoparticle with europium. While synthesizing the shells,

an excess of europium was required to coordinate to the O^{2-} sites of the magnetite cores, as europium will also coordinate with oleic acid and oleylamine after it is protonated. This was seen during the purification as the collected nanoparticles got darker as more europium coordinated with surfactant was removed.

3.3.2 XRD Characterization of Cores

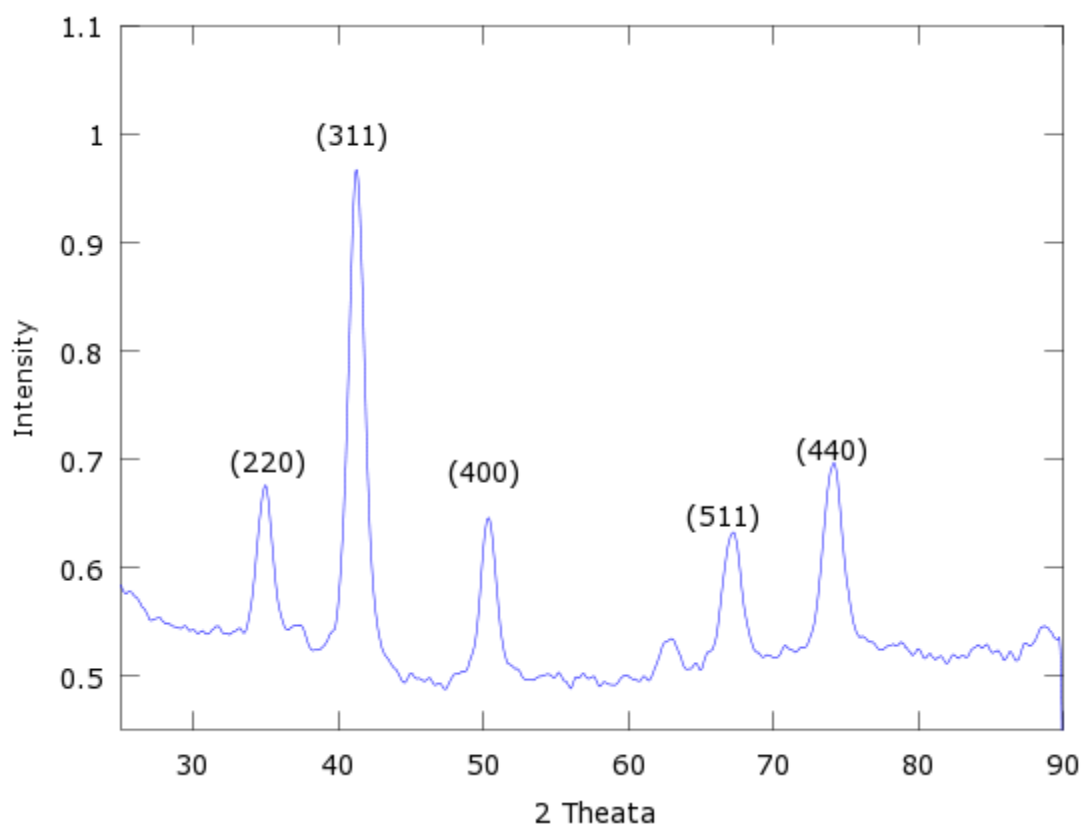


Figure 3.21. XRD diffraction pattern of magnetite cores.

Two batches of cores were synthesized for experiments to produce core-shell nanoparticles. XRD spectra show diffraction patterns expected of magnetite without shifting due to europium incorporation⁴. (Figure 3.21) The Scherrer equation was again

used to calculate average nanoparticle size with both batches producing an average size of 18 nm. This showed good reproducibility in synthesizing cores.

3.3.3 ICP-OES Measurement of Cores

Further characterization using ICP-OES was done to determine the amount of europium coating the cores. ICP-OES measurements show that even with an excess of europium to coat the shell, little europium actually formed the shell. (Table 3.3)

Table 3.3 ICP-OES measurements on cores and core-shell nanoparticles.

	Actual Europium Conc. (%)	Actual Iron Conc. (%)
Cores	0.0001 ± 0.0003	99.999 ± 0.0003
Core-Shell	1.86 ± 0.75	98.14 ± 0.75

The cores show a small amount of europium. This may either be from overlapping bands with iron wavelengths showing a false europium concentration, or background noise. The amount of europium that does form the shell for the nanoparticles is approximately 2%. This method for producing core-shell nanoparticles is not efficient due to the initial high concentration of europium needed to overcome coordination with surfactant, and the low amount of europium coating the core.

3.4 LUMINESCENCE IMPROVEMENT MEASUREMENTS OF ALL SYNTHESIZED NANOPARTICLES

Improving luminescent properties of the magnetite nanoparticles while still retaining their paramagnetic properties was the overall goal of this research. All synthesized nanoparticles were compared using UV-Vis and fluorescence spectroscopy, and quantum yields were calculated to determine the luminescent property improvements.

3.4.1 UV-Vis Absorption for all Synthesized Nanoparticles

UV-Vis absorption spectroscopy was another method to determine if iron oxide nanoparticles formed during synthesis, and further proved surface coating with TTA. Iron oxide nanoparticles typically scatter light due to their size. Iron oxide nanoparticles do

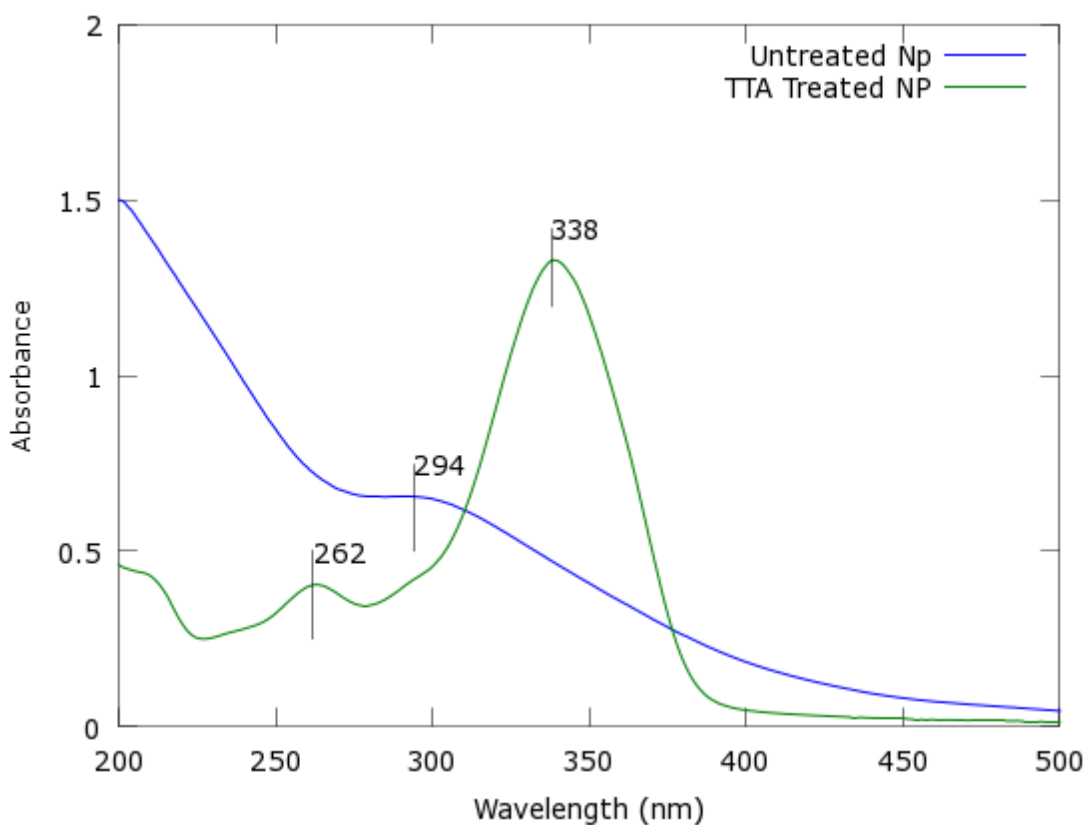


Figure 3.22. UV-Vis absorption for citric acid and TTA coated co-precipitation nanoparticles.

absorb light in the ranges of 240 nm to 290 nm according to their size and the surfactant used as a capping ligand²⁵. Comparing surfactant and TTA coated nanoparticles the different absorptions can be seen. (Figure 3.22) The co-precipitation nanoparticles coated in citric acid absorbed light at 294 nm. This same value was seen for all co-precipitation nanoparticles regardless of europium doping amounts.

There are two absorption bands for the TTA coated nanoparticles. A low energy band at 266 nm, and a high energy band at 338 nm both of which is from the $\pi - \pi^*$ of the organic chromophore. UV-Vis absorption spectroscopy was also performed on TTA to ensure these peaks were associated only with TTA. (Figure 3.23)

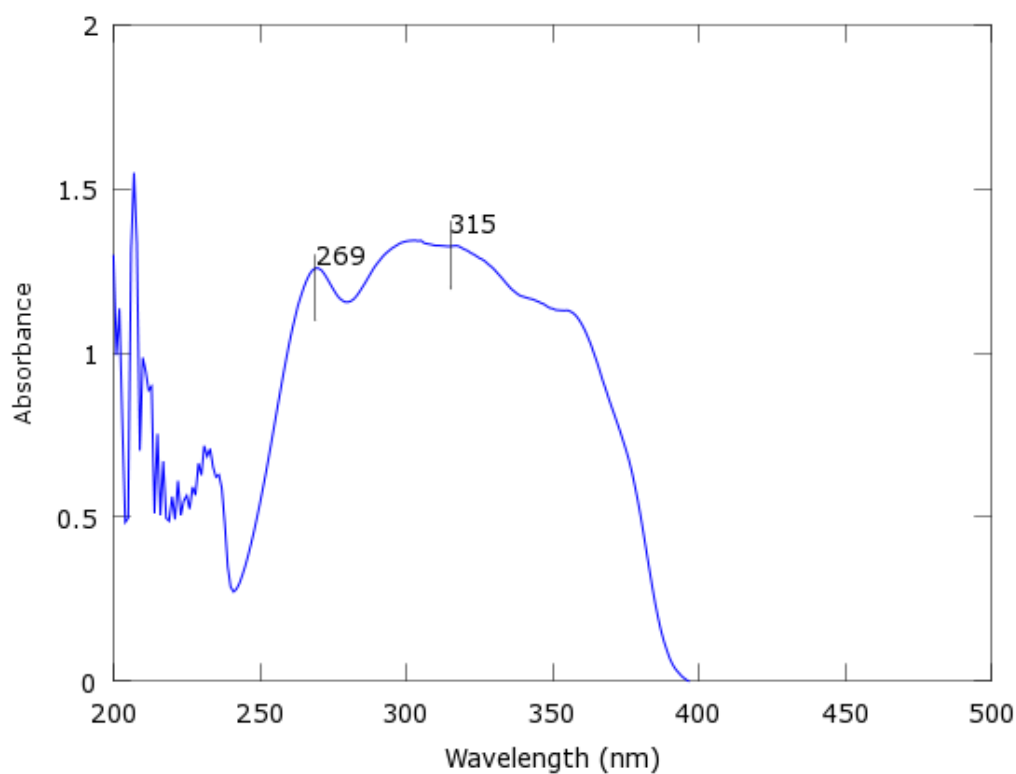


Figure 3.23. UV-Vis absorption spectrum of TTA.

The peak for 266 nm shifts slightly to 269 nm, and there is a broad absorption centered at 315 nm. It is this broad band in which the electronic energy is absorbed and transferred to the europium metal ion for luminescence.

For the high temperature nanoparticles the absorption due to iron oxide is lower than that of citric acid coated nanoparticles, approximately 268 nm instead of 294 nm. This was seen for both doping percentages. The surfactants and size of the nanoparticles are different and explains the different absorption band. (Figure 3.24)

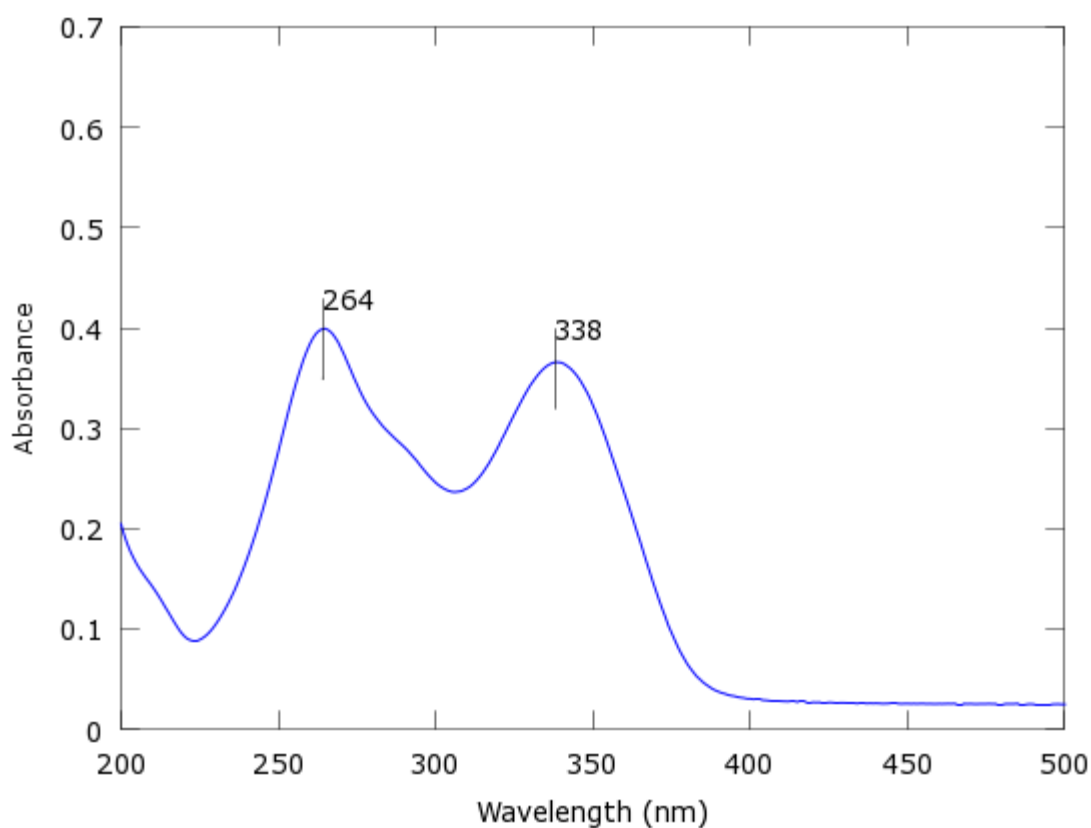


Figure 3.24. UV-Vis absorption of oleic acid and TTA coated high temperature

For the TTA coated nanoparticles the two absorption bands present. The high energy band remains at 338 nm, while the low energy band shifts slightly to 264 nm. For the core-shell nanoparticles the two TTA absorption bands for $\pi - \pi^*$ of the β -diketone are at the same wavelengths, 266 nm and 338 nm. (Figure 3.25) All synthesized nanoparticles surface coordinated with TTA had the same two absorption bands regardless of synthesis method.

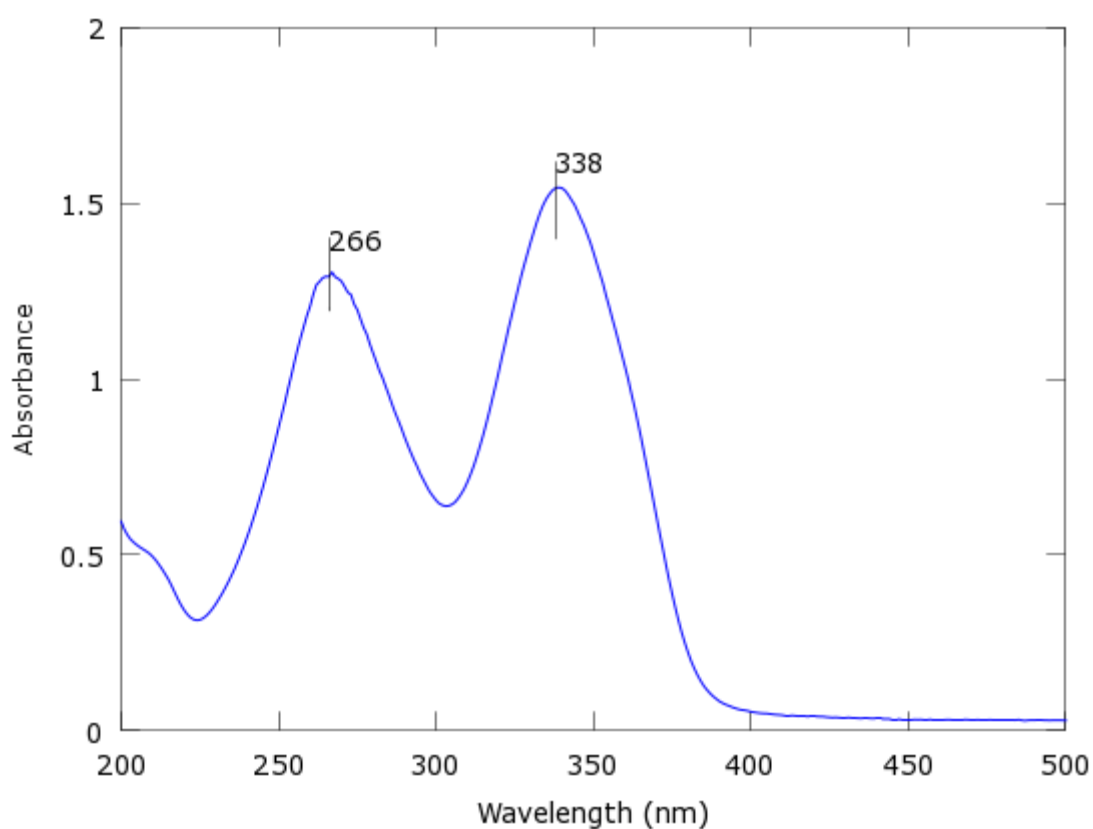


Figure 3.25. UV-Vis absorption spectrum of core-shell nanoparticles coordinated with TTA.

3.4.2 Fluorescence Spectroscopy for Co-precipitation Nanoparticles

Low temperature thermally decomposed co-precipitation nanoparticles were used for testing variables such as europium doping percentage and TTA surface coordination

amounts. Europium has four luminescence peaks typically seen in a fluorescence spectrum. These peaks correspond to f orbital relaxations through luminescence to the ground state of the europium metal ion. For europium the most intense peak is found at 614 nm, corresponding to the 5D_0 - 7F_2 electronic transition. (Figure 3.26) Remaining peaks are at 580 nm, 593 nm, and 652 nm, corresponding to 5D_0 - 7F_0 , 5D_0 - 7F_1 , and 5D_0 - 7F_3 respectively.

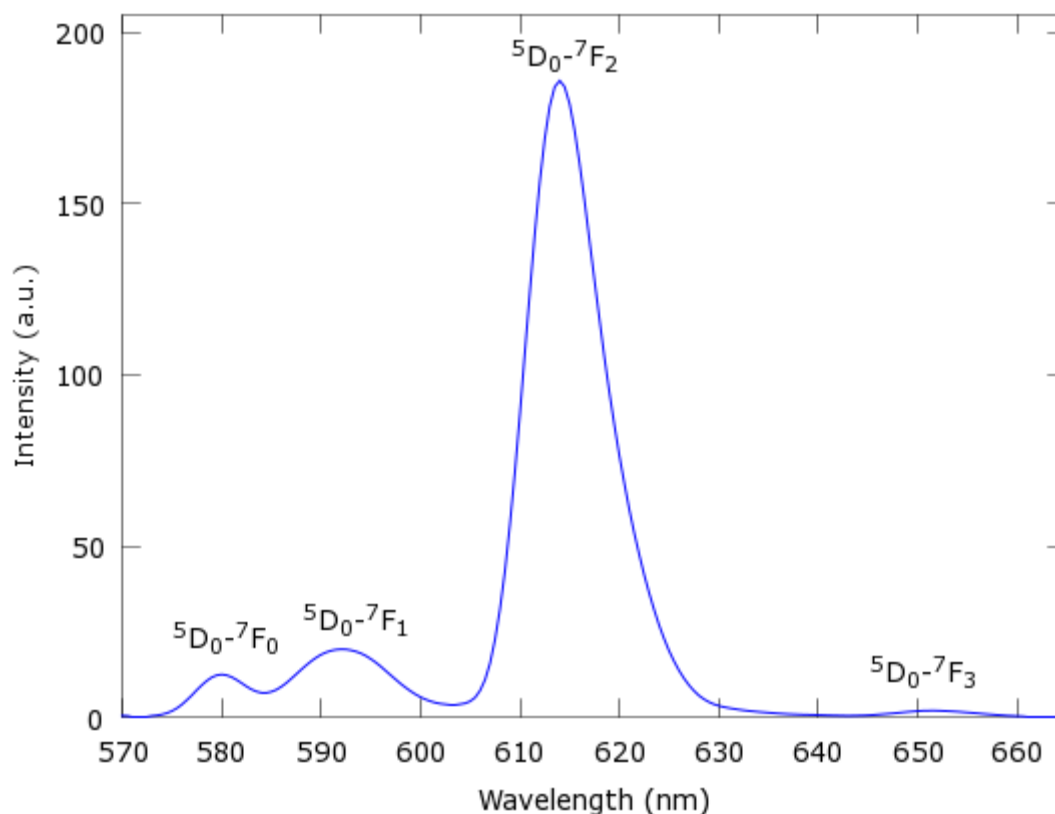


Figure 3.26. Luminescence spectrum of 40:60 co-precipitation nanoparticles.

The europium doping percentages were done in a linear scale up from 16:84 europium to iron oxide, to 20:80, 30:70, and 40:60. The luminescent intensities showed a linear progression as the linear scale up of europium doping increased. A maximum average intensity of 185 for 40:60 doped nanoparticles, and a minimum average intensity

of 93 for 16:84 doped nanoparticles is seen. This follows our hypothesis in that more europium doped into the nanoparticle should increase luminescence. (Figure 3.27)

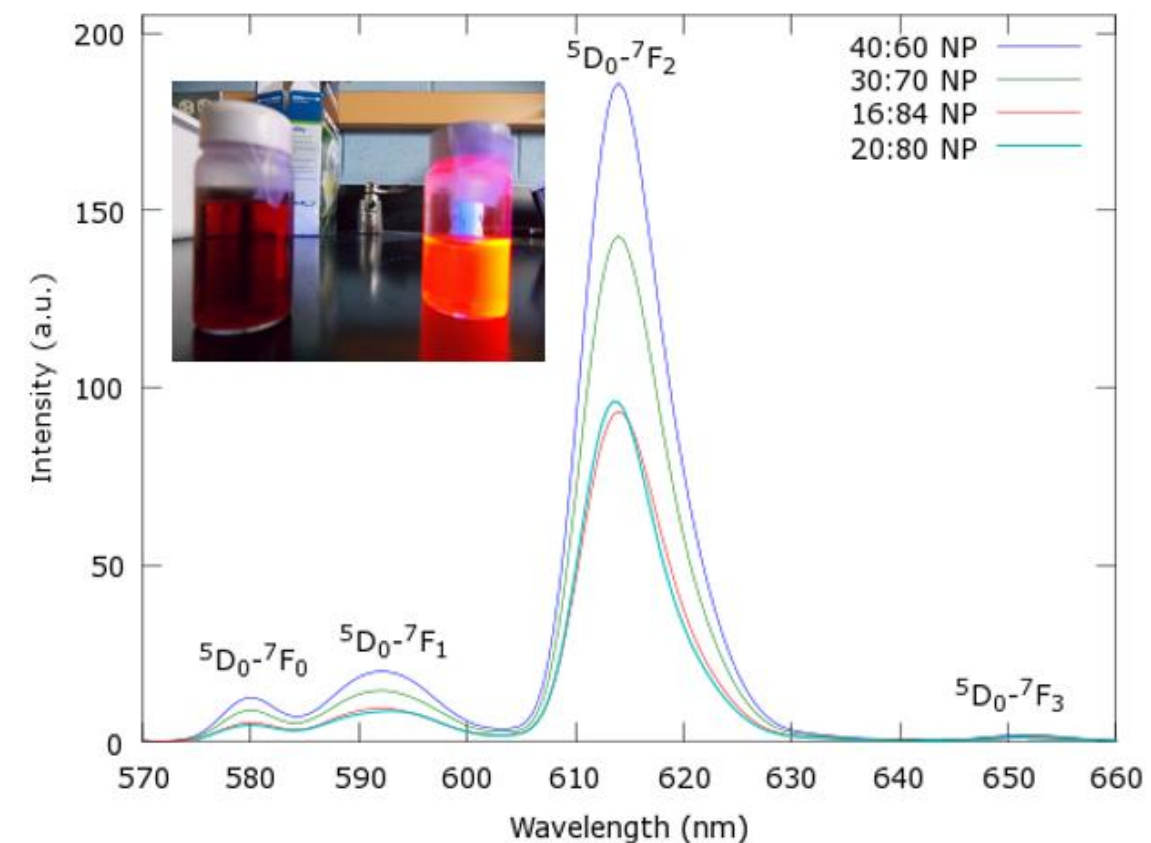


Figure 3.27. Luminescence spectra of all co-precipitation nanoparticles.

Testing the variance of TTA surface coating the nanoparticle came next. This was done through a series of surface coating amounts for each doping level, starting with 8 mg/75 mg to 90 mg/ 75 mg TTA to nanoparticle weight respectively. The initial results of the TTA surface coating amounts showed that additional TTA was required as more europium was doped into the iron oxide nanoparticle. For low europium doped

nanoparticles such as 16:84 and 20:80, the amount of TTA required was 16 mg TTA/ 75 mg nanoparticles. For higher doping levels such as 30:70 and 40:60 TTA amounts increased to 40 mg TTA/ 75 mg NP and 48 mg/ 75 mg NP respectively. (Figure 3.28) Quantum yield measurements were calculated to confirm this initial finding.

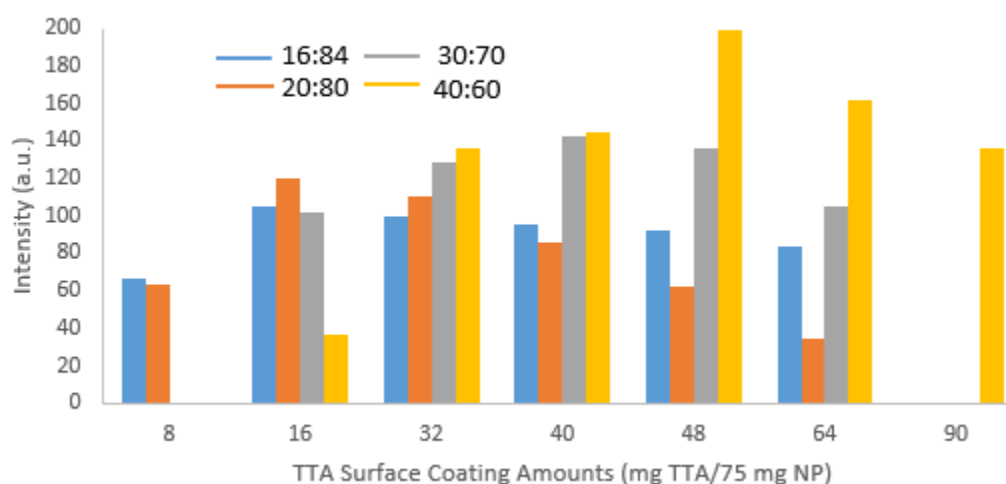


Figure 3.28. Luminescent intensities as a comparison of TTA coating amounts and europium doping.

3.4.3 Quantum Yield Measurements of Co-precipitation Nanoparticles

Luminescence quantum yields (Φ) of the nanoparticles were calculated using cresyl violet acetate as the reference ($\Phi_R = 54\%$ in methanol)¹⁴ as shown in Equation (1.3) where Abs, A and n denote the absorbance (at highest absorption maxima), integrated area of the emission spectrum, and the refractive index of the solvent, respectively. Subscripts R and S refer to the reference and the sample, respectively.

$$\Phi_S = \Phi_R (Abs_R) / (Abs_S) (A_S / A_R) (n^2_S / n^2_R) \quad \text{Eqn 1.3}$$

Area under the luminescent curve was calculated using FLWinlab graphing and arithmetic calculation program available with the instrument software.

The results of the quantum yield measurements show that regardless of the amount of europium doped into the Eu(III)-doped magnetite nanoparticle, the same amount of TTA organic chromophore is required. (Table 3.4) This optimal ratio of TTA to dry nanoparticle mass was calculated to be 32 mg TTA/ 75 mg nanoparticle.

Table 3.4. Quantum yields of co-precipitation nanoparticles with various TTA coatings.

TTA Coating	8.32:91.68 NP Φ (%)	8.92:91.18 NP Φ (%)	13.97:86.03 NP Φ (%)	18.32:81.98 NP Φ (%)
16 mg	0.27 \pm 0.016	0.36 \pm 0.018	1.3 \pm 0.016	1.5 \pm 0.016
32 mg	0.40 \pm 0.014	0.43 \pm 0.012	1.5 \pm 0.019	1.8 \pm 0.013
40 mg			1.3 \pm 0.016	1.5 \pm 0.015
64 mg	0.30 \pm 0.015	0.31 \pm 0.016		

3.4.4 Fluorescence Spectroscopy for High Temperature and Core-Shell Nanoparticles

Once the quantum yield of the low temperature based co-precipitation nanoparticles was determined, the information could then be transferred to the high temperature thermal decomposition, and core-shell nanoparticles. The luminescence spectra of high

temperature nanoparticles displayed the same luminescence bands as co-precipitation nanoparticles, with much weaker intensities. (Figure 3.29)

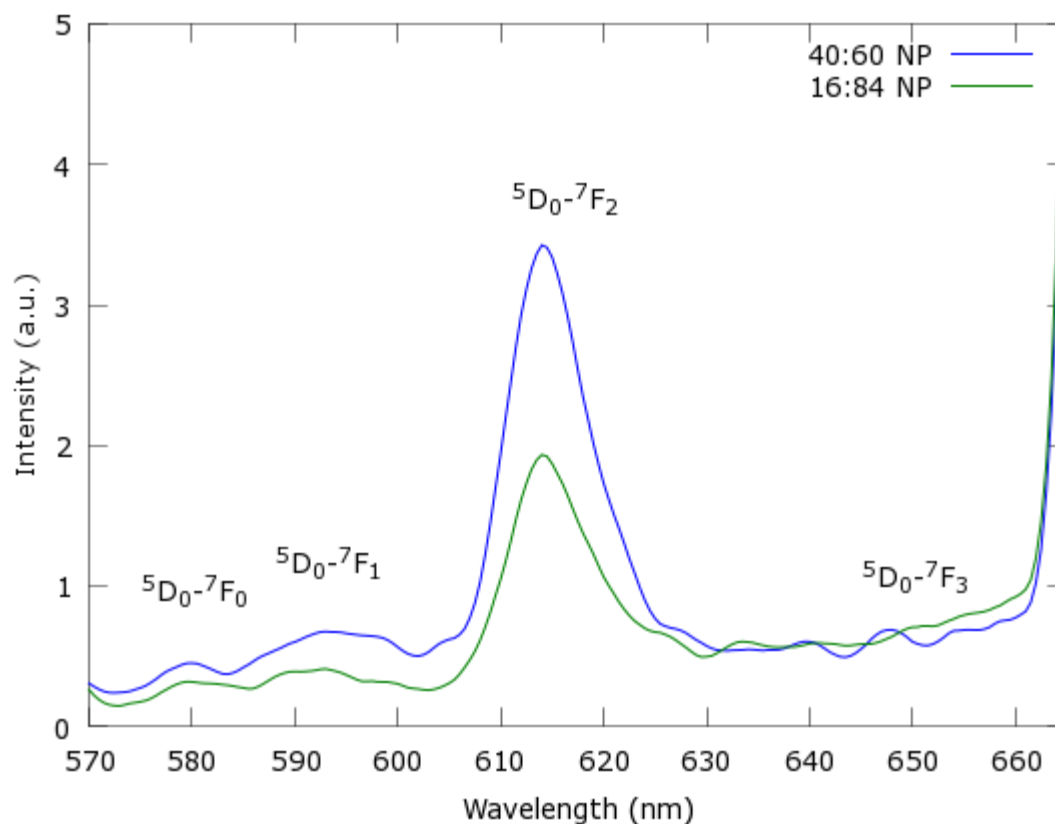


Figure 3.29. Luminescent intensities of 16:84 and 40:60 high temperature nanoparticles.

The high temperature nanoparticles had a maximum intensity of 3.4 for 40:60 nanoparticles. This same intensity value was seen for both batches of 40:60 europium doped high temperature nanoparticles with a surface coordination of 32 mg TTA/ 75 mg nanoparticle. For the 16:84 europium doped nanoparticles a maximum intensity value of 1.9 for both batches of nanoparticles with 32 mg TTA/ 75 mg nanoparticle. These values are low but do show a linear increase in luminescence intensities as expected for increased europium doping.

Core-shell nanoparticles displayed greater intensities than that of the high temperature thermally decomposed nanoparticles, but still much weaker than those of the co-precipitation method. Again the same luminescence peaks were observed for the core-shell nanoparticles. (Figure 3.30)

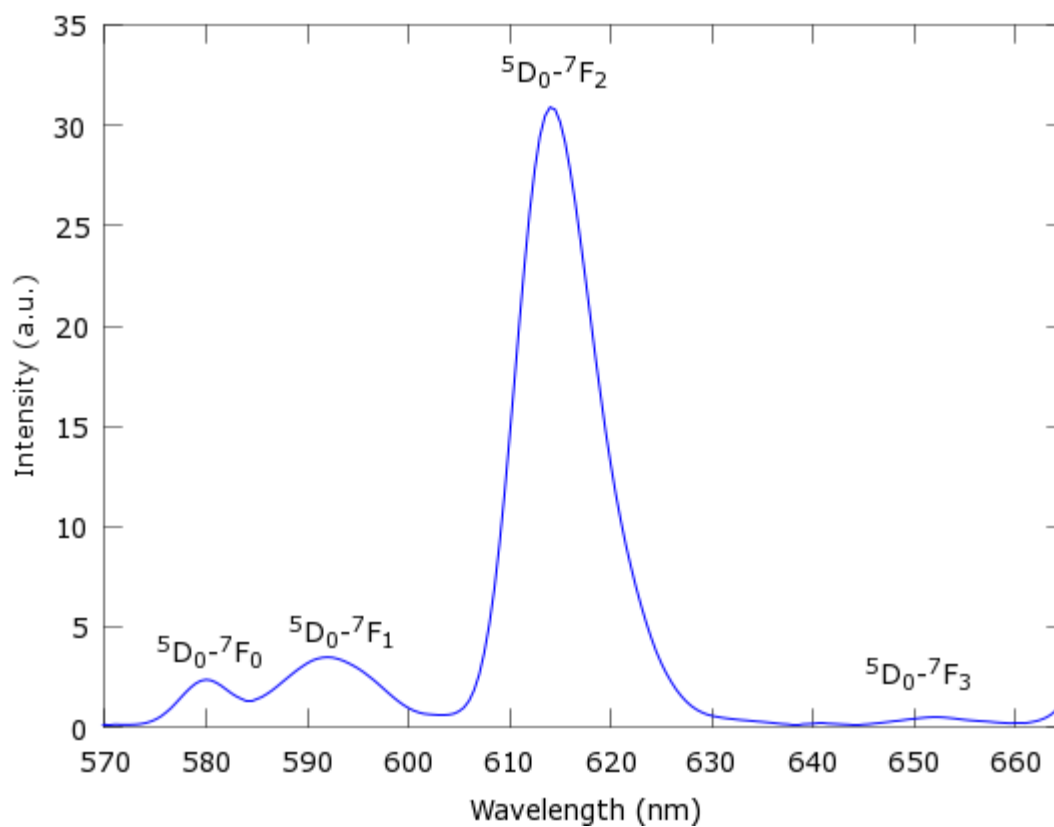


Figure 3.30. Luminescent intensity of core-shell nanoparticles.

The average maximum intensity for core-shell nanoparticles is 30. This is low but ICP-OES data shows the amount of europium coating the shell is approximately 2%. This is the lowest amount of europium by mass for any of the synthesized nanoparticles.

3.4.5 Quantum Yield Measurements for High Temperature and Core-Shell Nanoparticles

The quantum yields were calculated in the same manner as those performed for the co-precipitation nanoparticles. The quantum yield data shows that the high temperature nanoparticles were not efficient at luminescence. (Table 3.5)

Table 3.5. Quantum yield results for high temperature and core-shell nanoparticles.

Nanoparticle	Quantum Yield (Φ) %
40:60	0.027 ± 0.0047
16:84	0.019 ± 0.0067
Core-shell	0.17 ± 0.069

3.5 CONCLUSION

The results show that the nanoparticles which had the most significant luminescence improvement were the co-precipitation nanoparticles. Based on mass of europium in the nanoparticle these were the most efficient nanoparticles as a ratio of quantum yield/ mass of europium. A close second was the core-shell nanoparticles. The high temperature nanoparticles were not efficient based on quantum yield and mass of europium. The high temperature thermal decomposition method did synthesize nanoparticles with a strong paramagnetic property, and was the most efficient method for doping europium into the nanoparticle. Thermal decomposition synthesis created very crystalline magnetite, even when doped with europium. The co-precipitation method did not crystallize, and did not dope as high of values as the high temperature thermal

decomposition. This indicated that the crystal lattice of europium is highly effective at trapping europium within its unit cells.

This high crystallinity is possibly a hindrance as well. While the co-precipitation method did not dope as much europium, it had higher quantum yields. This indicates that the crystal lattice of magnetite is quenching the europium. This could either be occurring as a result of doping the europium too close to each other, causing a europium to europium quench, or by the iron oxide matrix the europium is incorporated into. When europium is too concentrated, triplet to triplet annihilation can occur. This annihilation prevents the sensitization effect from the chromophore and results in lower quantum yields than expected²⁶. For the high temperature nanoparticles, it appears that the crystal that forms the nanoparticle may be concentrating the europium and causing triplet to triplet annihilation. In the co-precipitation nanoparticles an amorphous structure formed. This may have caused the europium to be more evenly distributed throughout the nanoparticle.

Iron oxide nanoparticles, hematite, are four orders of magnitude higher as quenchers than Fe^{3+} ions. Small magnetite nanoparticles have a greater surface area when compared to bulk atom ratio. The quenching occurs through static quenching in which the excited molecule is in close proximity to the quencher and is immediately quenched before electronic energy transitions can occur²⁷. Combining the high concentration of europium per mass within the crystal lattice in conjunction with iron oxide being an efficient quencher of fluorescent molecules, explains why the high temperature nanoparticles had such low quantum yields. This also explains why, even with the co-precipitation method low quantum yields were observed. The co-precipitation nanoparticles were weakly magnetic confirming paramagnetic properties associated with iron oxide, although the

XRD measurements showed them to be amorphous. This iron oxide matrix was still created and was responsible for quenching of the europium metal ion.

For the core-shell nanoparticles, the surface area of the magnetite cores were quenching the europium metal ions coordinated to the surface. If the amount of europium that had coordinated to the surface had been doped instead, total quenching would have been likely to occur. If core shell nanoparticles of this nature are to be synthesized in the future, a second layer between the core and the shell will be needed to remove the quenching properties of iron oxide.

For doping europium into iron oxide nanoparticles, this method does not seem effective. A method to remove the quenching capabilities of iron oxide will have to be employed. Doping europium into iron oxide nanoparticles may not even be possible without extensive quenching. A core-shell-shell nanoparticle may be the only method to separate the surface of iron oxide and the lanthanide to create dual modality nanoparticles of iron oxide and europium with high quantum yields. This shell between the europium and iron oxide will have to be of a nature that prevents quenching of europium. Although quenching did occur for all nanoparticles, this research has shown that even high doping of europium into the crystal lattice of magnetite does not greatly affect its paramagnetic properties. All synthesized nanoparticles did show luminescence improvements from iron oxide nanoparticles, although possibly not enough to be effective biomedical imaging agents.

REFERENCES

1. Scherer, C.; Figueiredo Neto, A.M. Ferrofluids: Properties and Applications. *Brazilian J. Phys.* **2005**, 35, vol 3A, 718-727.
2. Willis, A. L.; Chen Z.; He, J.; Zhu, Y.; Turro, N.J.; O'Brian, S. Metal Acetylacetonates as General Precursors for the Synthesis of Early Transition Metal Oxide Nanomaterials. *J. Nanomaterials.* **2007**, 14858, 7.
3. Ehlers, E. G. *The Interpretation of Geological Phase Diagrams*. San Francisco: W.H. Freeman, 1972. Print.
4. The Mineral Magnetite. <http://www.galleries.com/magnetite.html>. (March 04 2014)
5. Xuea, F.; Liangb, M.; Wanga, Z.; Luana, L.; Lia, F.; Chenga, Y.; Shaoc, G. The Preparation and Performance of Visible-Light-Sensitized Luminescent Nanoparticles Based on Europium Complex. *Chinese Chemical Letters.* **2014**, 25, vol 2, 247-252.
6. Tang, R.; Xuli, F. Highly Luminescent Conjugated Polymer Nanoparticles for Imaging and Therapy. *Canadian Chemical Transactions.* **2013**, 1, 78-84.
7. Xi, P.; Cheng, K.; Sun, X.; Zeng, Z.; Sun, S. Magnetic Fe₃O₄ Nanoparticles Coupled with a Fluorescent Eu Complex for Dual Imaging Application. *Chem. Commun.* **2012**, 48, 2952-2954.
8. Wang, B.W.; Hai, J.; Wang, Q.; Li, T.; Yang, Z. Coupling of Luminescent Terbium Complexes to Fe₃O₄ Nanoparticles for Imaging Applications. *Agnew. Chem. Int. Ed.* **2011**, 50, 3063-3066.
9. Li, Z.; Zhang, Y. Facile Synthesis of Lanthanide Nanoparticles With Paramagnetic, Down- and Up-Conversion Properties. *Nanoscale.* **2010**, 2, 1240-1243.

10. Zhong, C.; Yang, P.; Li, X.; Li, C.; Wang, D.; Gai, S.; Lin, J. Monodisperse Bifunctional $\text{Fe}_3\text{O}_4@\text{NaGdF}_4:\text{Yb/Er}@\text{NaGdF}_4:\text{Yb/Er}$ Core-shell Nanoparticles. *RSC Adv.* **2012**, 2, 3194-3197.
11. Saini, S.; Singh, H.; Bagchi, B. Fluorescence Resonance Energy Transfer (FRET) in Chemistry and Biology: Non-Förster Distance Dependence of the FRET Rate. *J. Chem. Sci.* **2006**, 118, 23-35.
12. Klink, S.I.; Hebbink, G.; Grave, L.; Alink, P.; Van Veggel, F.; Werts, M. Synergistic Complexation of Eu^{+3} by a Polydentate Ligand and a Bidentate Antenna to Obtain Ternary Complexes With High Luminescence Quantum Yields. *J. Phys. Chem.* **2002**, 106, 3681.
13. Racuciu, M.; Creanga, D.E.; Airinei, A. Citric-Acid-Coated Magnetite Nanoparticles for Biological Applications. *Eur. Phys. J.* **2006**, 21, 117-121.
14. DeSilva, C. R.; Maeyer, J.R.; Wang, R.; Nichol, G.S.; Zheng, Z. Adducts of Europium B-Diketonates with Nitrogen *p,p'*-Disubstituted Bypyridine and Phenanthroline Ligands: Synthesis, Structural Characterization, and Luminescence Studies. *Inorg. Chim. Act.* **2007**, 360, 3543-3552.
15. DeSilva C.R.; Smith, S.; Shim, I.; Pyun, J.; Gutu, T.; Jiao, J.; Zheng, Z. Lanthanide(III)-Doped Magnetite Nanoparticles. *J. Am. Chem.* **2009**, 131, 6336-6337.
16. Lipson, H.; Steeple, H. Interpretation of X-ray Powder Diffraction Patterns. London and Basingstoke. W.H. MacMillian and Co Ltd, 1970. Print.
17. Thanh, N. T. K. Magnetic nanoparticles: from fabrication to clinical applications: theory to therapy, chemistry to clinic, bench to bedside. Boca Raton, FL: CRC Press, 2012. Print.

18. Mascolo, M. R.; Pei, Y.; Ring, T. A. Room Temperature Co-Precipitation Synthesis of Magnetite Nanoparticles in a Large pH Window with Different Bases. *Materials*. **2013**, 6, 5549-5567.
19. Silverstein, R. M.; Webster, F. X.; Kiemel, D. J. Spectrometric Identification of Organic Compounds. 7th ed. Hoboken NJ: John Wiley and Sons, 2005. Print.
20. Zhao, F.; Zhang, B.; Feng, L. Preparation and Magnetic Properties of Magnetite Nanoparticles. *Materials Letters*. **2012**, 68, 112-114.
21. Angermann, A.; Töpfer, J. Synthesis of Magnetite Nanoparticles by Thermal Decomposition of Ferrous Oxalate Dihydrate. *J. Mater. Sci.* **2008**, 43, 5123-5130.
22. Florez, J.M.; Mazo-Zuluaga, J.; Restrepo. Ferrimagnetic to Paramagnetic Transition in Magnetite: Mössbauer Versus Monte Carlo. *Hyperfine Interactions*. **2005**, 161, 161-169.
23. Monshi, A.; Foroughi, M.R.; Monshi, M. R. Modified Scherrer Equation to Estimate More Accurately Nano-Crystallite Size Using XRD. *W. J. Nano Sci. Eng.* **2012**, 2, 154-160.
24. Al-Anber, M. A. Synthesis and Characterization of Zinc β -Diketonate Complex extended to the Macromolecular Polymers. *Oriental Journal of Chemistry*. **2013**, 29, 1437-1441.
25. Srivastava, S. Synthesis and Characterization of Iron Oxide Nanoparticles from FeCl_3 by Using Polyvinyl Alcohol. *IJPSS*. **2012**, 2, 161-184.
26. Yong, Z.; Lei, W.; Chun, Li.; Zeng, W.; Shi, H.; Cao, Y. Enhanced Electroluminescent Efficiency Based on Functionalized Europium Complexes in Polymer Light-Emitting Diodes. *Chin. Phys. Lett.* **2007**, 24, 1376-1380.

27. Al-Kady, A.; Gaber, M.; Hussein, M.; Ebeid, E. Structural and Fluorescent Quenching Characterization of Hematite Nanoparticles. *Spectrochimica Acta*. **2011**, 83, 398-405.

SUPPLEMENTAL INFORMATION

CHAPTER 2

OCTAVE PROGRAM FOR CALCULATING AVERAGE CRYSTALLINE LENGTH

```
%%%%%%%%%%%% filename = scherrereqn
%%%%%%%%%%%% date created 12/02/13
%%%%%%%%%%%% Purpose = to find the crystalline length of a nanoparticle or crystal
with XRD spectra and a modified scherrer equataion

clear

clf

%%%%%%%%%%%% ifile saved as Filename

ifile = 'EuFe3O4-oleic coated-Co#1.txt';

%%%%%%%%%%%% load data ifile

data = load(ifile);

datax = data';

x = datax(1,:);

y = datax(2,:);

%%%%%%%%%%%% Normalize the data to max value of one

v = y;

tmp = v - min(v);

vn = tmp/max(tmp);

plot(x,vn)

%%%%%%%%%%%% Smooth data

%smooth the data using Savitzky and Golay's smoothing techniques
```

```

U = vn;
gap= [ 1 2 3 4 5 6 7 6 5 4 3 2 1 ];
gapsize= length(gap);
gap= gap/sum(gap);
Us= conv(U,gap);
npts= length(Us);
wd= (gapsize - 1)/2;
Us([1:wd npts-wd+1:npts]) = [];
plot(x,Us,'LineWidth', 2)
xlabel '2Theata'
ylabel 'Intensity'
%return
%% Select whether to crop the data set to possibly get rid of "grease" present
from surfactant used
choice = menu('Do you want to crop the data set or not?','Yes','No')
switch choice
case{1}
[jnk,npts]=size(Us);
crop=[1:1000];
Us = Us(1,1000:npts);
x = x(1,1000:npts);
case{2}
end

```

```

%%%%%% Baseline fit data to baseline near zero

cr = [247 1061 1740 1865 2386 2960 3680 4740];

p = polyfit(x(cr),Us(cr),6);

fity = polyval(p,x);

Usub = Us - fity;

plot(x,Usub,'Linewidth',2)

%%%%%% Select peaks using GUI

%%%%%% Peaks were selected from XRD spectrum

rngb = [1286 1436 1549 1674 1824 2450 2550 3064 3465];

rnge = [1386 1524 1670 1774 2062 2526 2638 3152 3690];

for i = 1:length(rngb)

rng = rngb(i):rngb(i);

tmp = datax(1,rng);

tmp = tmp/sum(tmp);

[sigma(i),xc(i)] = gaussfit(x(rng'),tmp');

end

theata = xc;

B = sigma;

%%%%%%%%%% Calculation to find the maximum hieght of the peak selected from

the data set

for i = 1:length(rngb);

rngy = rngb(i):rngb(i);

```

```

peakmax(i) = max(U(rngy));
end

%%%%%%%%%%%%%%%%%%%%%%%%%%%%%%%%%%%%%%%%%%%%%%%%%%%%%%%%%%%%%%%%%%%%%%%% Taking the maximum hieght from the peak and dividing by two
for the full width half muximum

H = (peakmax(1,+)/2);

%%%%%%%%%%%%%%%%%%%%%%%%%%%%%%%%%%%%%%%%%%%%%%%%%%%%%%%%%%%%%%%%%%%%%%%% Calculating the theata values from the 2theata. Diving 2theata by 2

[junk,npts] = size(theata);

for i = (1:npts)

theata2(1,i) = (theata(1,i)/2);

end

%%%%%%%%%%%%%%%%%%%%%%%%%%%%%%%%%%%%%%%%%%%%%%%%%%%%%%%%%%%%%%%%%%%%%%%%Calculating the ln(1/(cos(theata))) for plotting the scatter plot x
axis

[junk,npts]=size(theata);

for i =(1:npts)

theata3(1,i)= (log(1/sind(theata(1,i)/2)));

end

%%%%%%%%%%%%%%%%%%%%%%%%%%%%%%%%%%%%%%%%%%%%%%%%%%%%%%%%%%%%%%%%%%%%%%%% Calculating the FWHM from the sigma calculated from the
gaussfit and the maximum hieght found earlier

[junk,npts] = size(B)

for i = (1:npts)

B2(1,i) = (exp((-H(1,i))^2)/(2*(B(1,i)^2)));

end

%%%%%%%%%%%%%%%%%%%%%%%%%%%%%%%%%%%%%%%%%%%%%%%%%%%%%%%%%%%%%%%%%%%%%%%% Calculating the ln(FWHM) for the scatter plot y axis

```

```

[junk,npts] = size(B);

for i = (1:npts)

B3(1,i) = (log(B2(1,i)*(pi/180)));

end

%%%%%%%%%% Calculating the linear fit of the data and the Y-INT.

%%%%%%%%%% Plotting the scatter plot of the ln(FWHM) and ln(1/(cos(theata)))

p = polyfit(theata3,B3,1);

yp = polyval(p,theata3);

plot(yp)

hold on

scatter(theata3(1,:),B3(1,:),15)

%axis([0 2 -5 -3])

xlabel 'ln(1/cos(theata))'

ylabel 'ln(B)'

hold off

%%%%%%%%%% Variables used to calculate the cyrstalline length. K is the
spherical constant of nanoparticles. Co is the K alpha one of wavelength of Cobalt

%%%%%%%%%K = 0.89;

%%%%%%%%Co = 0.17889;

%%%%%%%%%% Choosing the X-ray source used when calibrating your XRD spectrum

choice = menu('Choose the X-ray source used in spectrum','Cu','Co')

switch choice

case{1}

```

```

Co = 0.154050

case{2}

Co = 0.17889

end

%%%%%%%%%%%%%%%%%%%%%%%%%%%%%%%%%%%%%%%%%%%%%%%%%%%%%%%%%%%%%%%%%%%%%%%%Choosing the K constant used when calculating the crystalline size

choice = menu('Choose the K constant for calculations','Spherical','General')

switch choice

case{1}

K = 0.89

case{2}

K = 1.0747

end

%%%%%%%%%%%%%%%%%%%%%%%%%%%%%%%%%%%%%%%%%%%%%%%%%%%%%%%%%%%%%%%%%%%%%%%% Y-INT calculations. B4 is the mean of the scatter points. B5 is
the linear fit Y-INT

B4 = mean(B3);

B5 = p;

%%%%%%%%%%%%%%%%%%%%%%%%%%%%%%%%%%%%%%%%%%%%%%%%%%%%%%%%%%%%%%%%%%%%%%%% Calculations of the exponential of the two Y-INT

Y1 = (exp(B4(1,:)));

Y2 = (exp(B5(:,2)));

%%%%%%%%%%%%%%%%%%%%%%%%%%%%%%%%%%%%%%%%%%%%%%%%%%%%%%%%%%%%%%%%%%%%%%%% Calculations of crystalline length using the two different Y-INT

L1 = ((K)*(Co))/(Y1);

L2 = ((K)*(Co))/(Y2);

disp(L1)

```

```
disp(L2)

%%%%%%%%%%Displaying message stating crystalline lengths

msg1 = sprintf('The average crystalline length of the sample with mean data was
calculated as %3.f nm',L1);

msg2 = sprintf('The average crystalline length of the sample with linear fit data was
calculated as %3.f nm',L2);

%%%%%%%%%%The linear fit data seems to be the more accurate of the two calculations
based off two different data sets

msg3 = sprintf('Crystalline Length program brought to you courtesy of Mickey Clark, Dr.
Huffman, and Dr. De Silva.');
```

```
disp(msg1)

disp(msg2)

disp(msg3)
```

CHAPTER 3

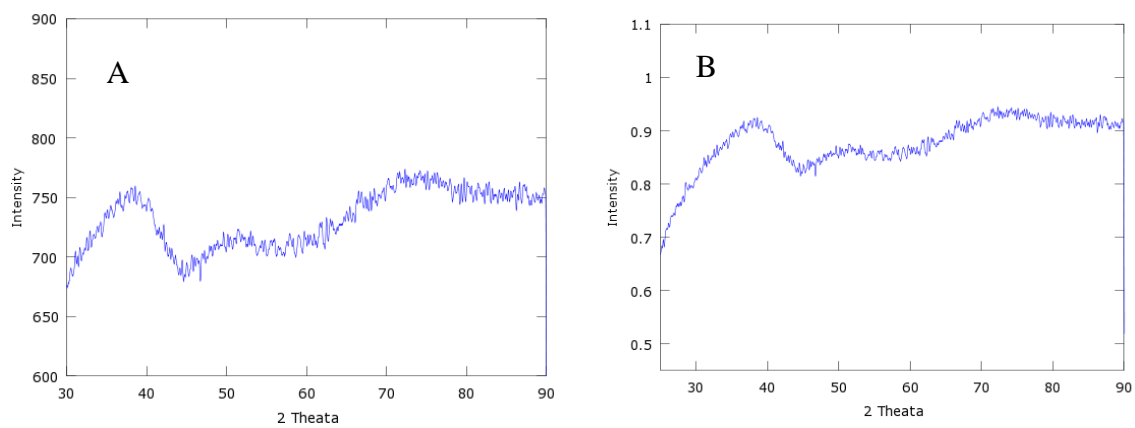


Figure S1 A-B. XRD spectra of co-precipitation nanoparticles [A] 40:60 [B] 20:80

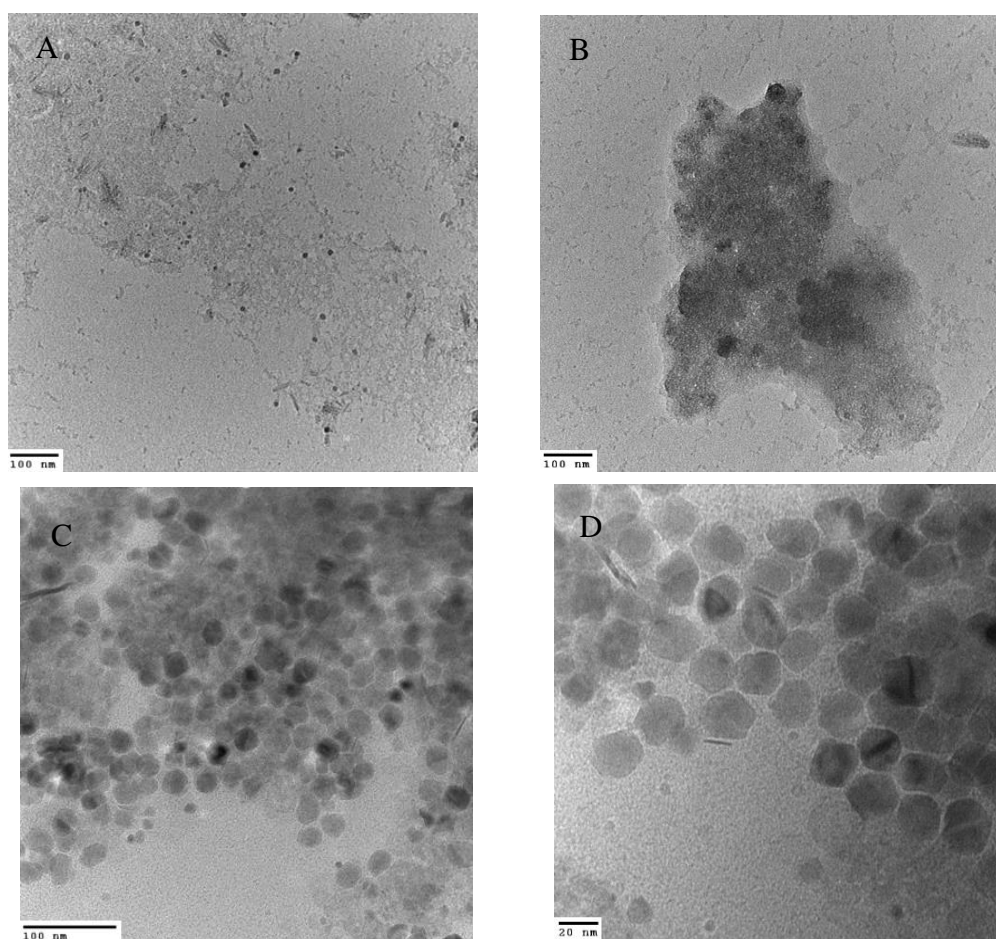


Figure S2 A-D. TEM image of co-precipitation nanoparticles 20:80 [A] [B] and 20:80 [C] [D].

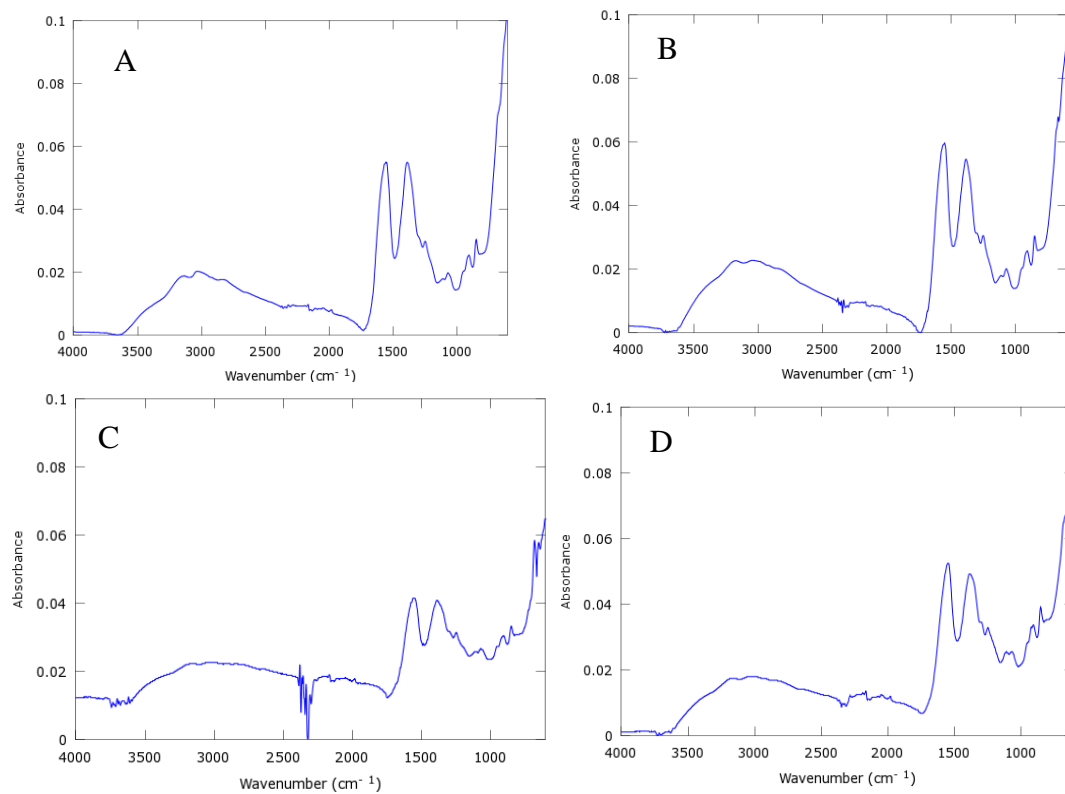


Figure S3 A-D. FT-IR spectra of co-precipitation nanoparticles coated with citric acid [A] 16:84 [B] 20:80 [C] 30:70 [D] 40:60.

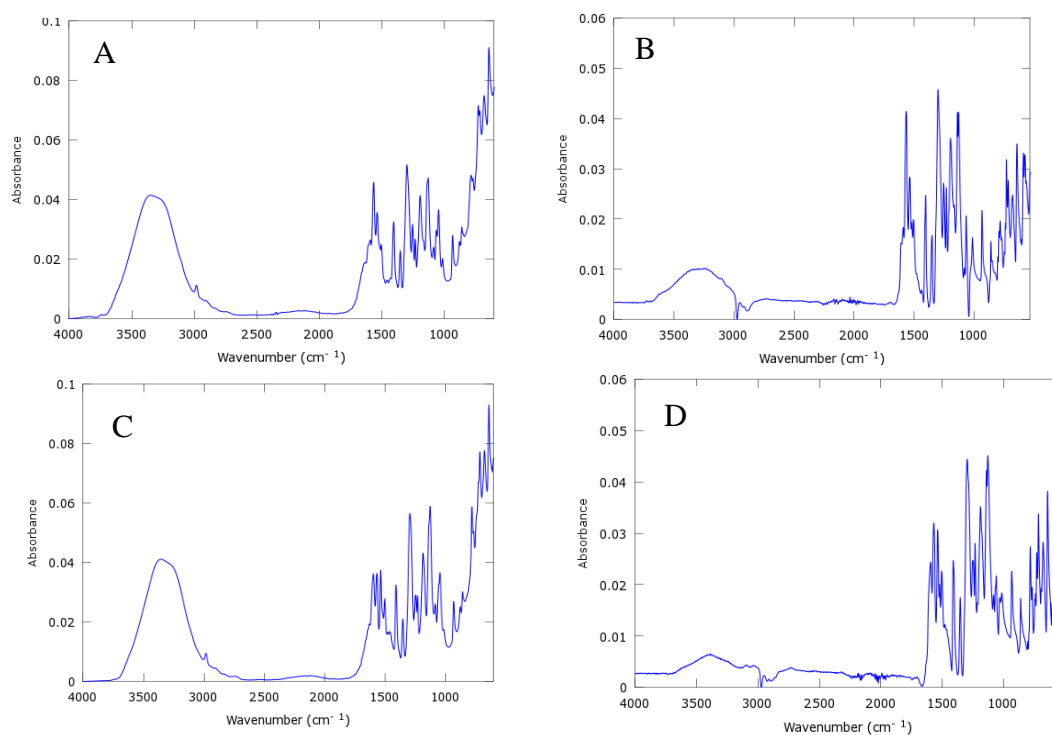


Figure S4 A-C. FT-IR spectra of TTA coated co-precipitation nanoparticles [A] 16:84 [B] 20:80 [C] 30:70 [D] 40:60.

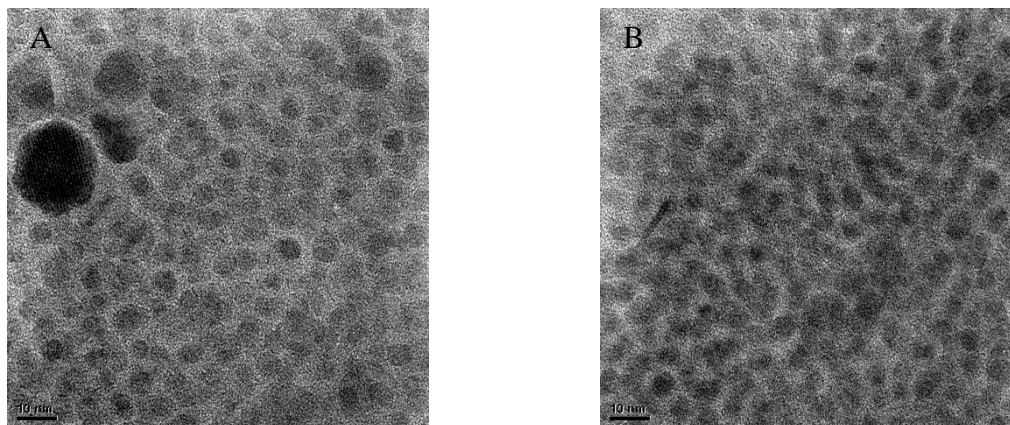


Figure S5 A-B. TEM images of high temperature 16:84 nanoparticles.

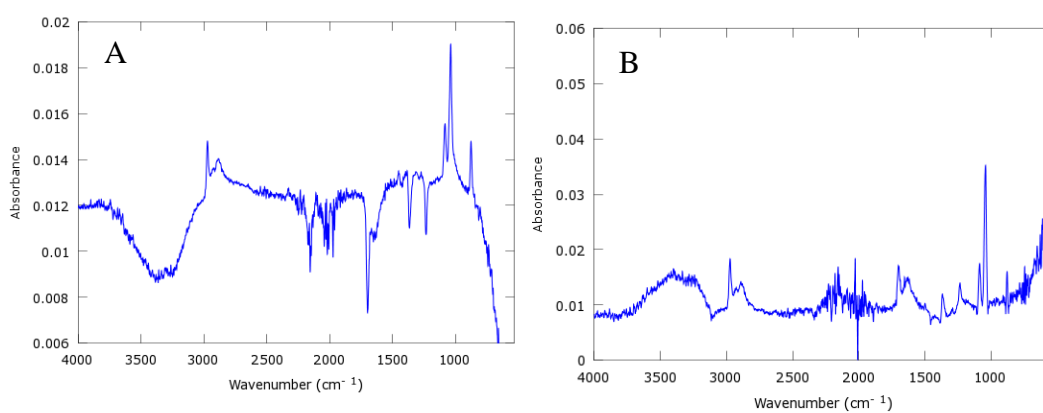


Figure S6 A-B. FT-IR spectra of TTA coated high temperature nanoparticles [A] 16:84 [B] 40:60.

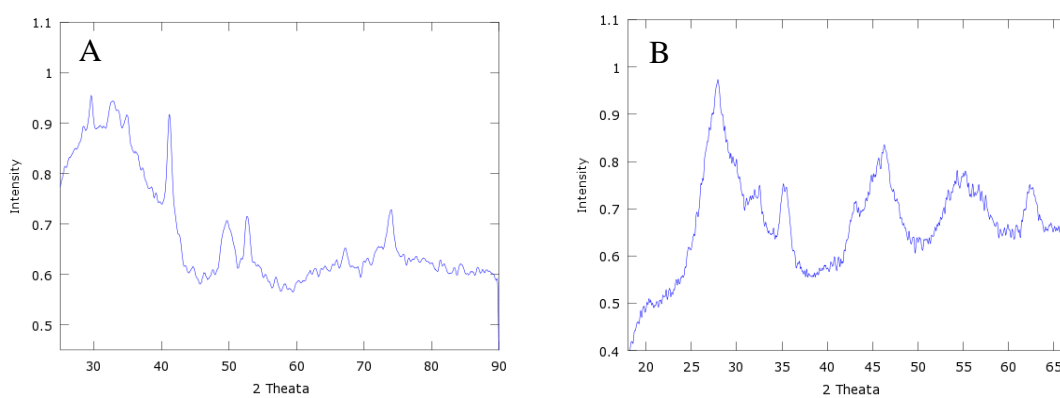


Figure S7 A-B. XRD spectra of high temperature nanoparticles [A] 16:84 [B] 40:60.

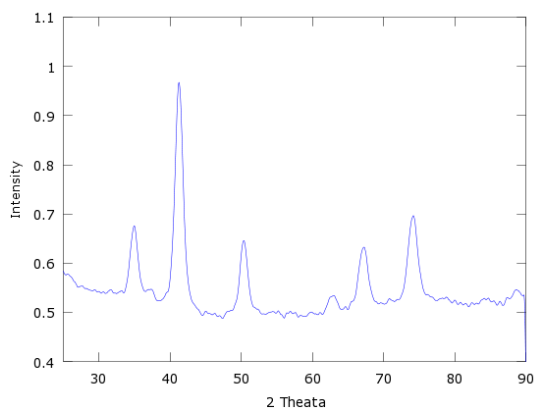


Figure S8. XRD spectra of second magnetite cores.

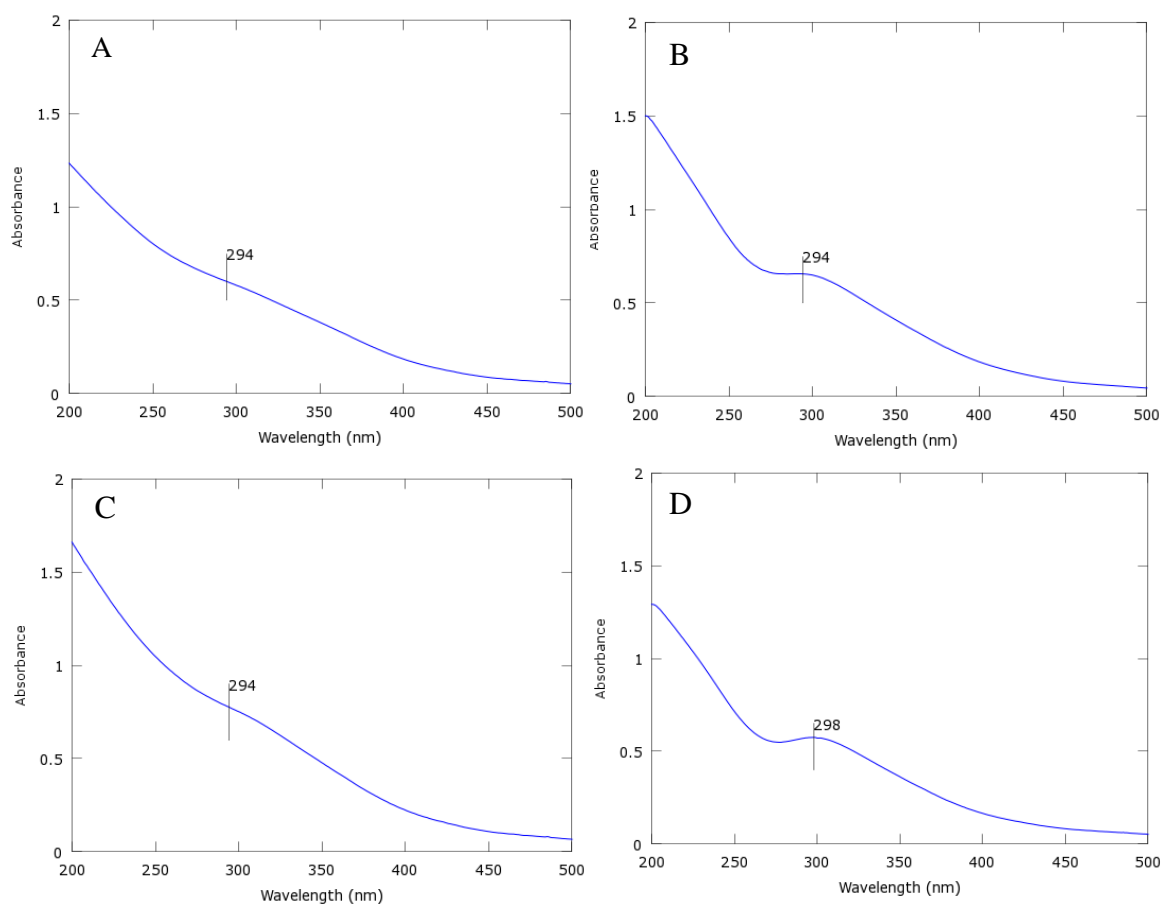


Figure S9 A-D. UV-Vis absorption spectra of co-precipitation nanoparticles [A] 16:84 [B] 20:80 [C] 30:70 [D] 40:60.

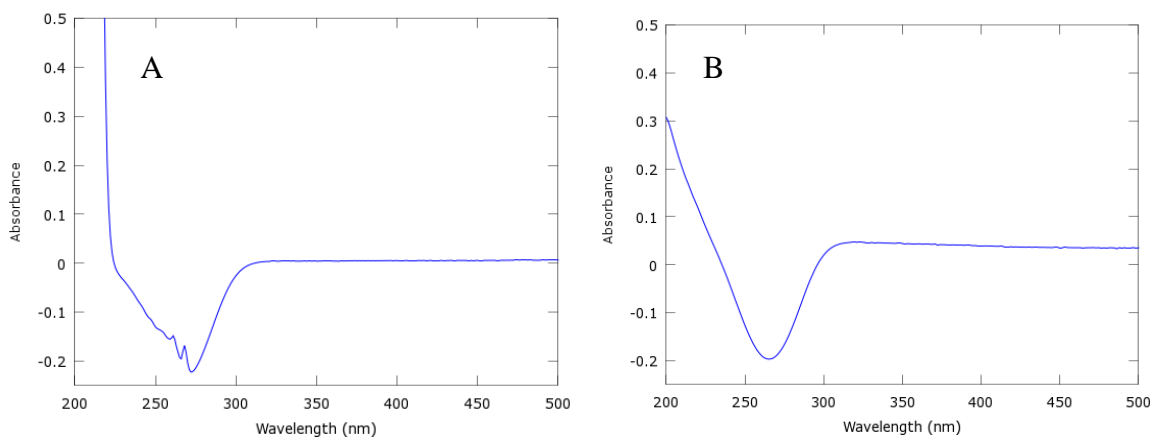


Figure S10 A-B. UV-Vis absorption spectra of high temperature nanoparticles [A] 16:84 [B] 40:60.

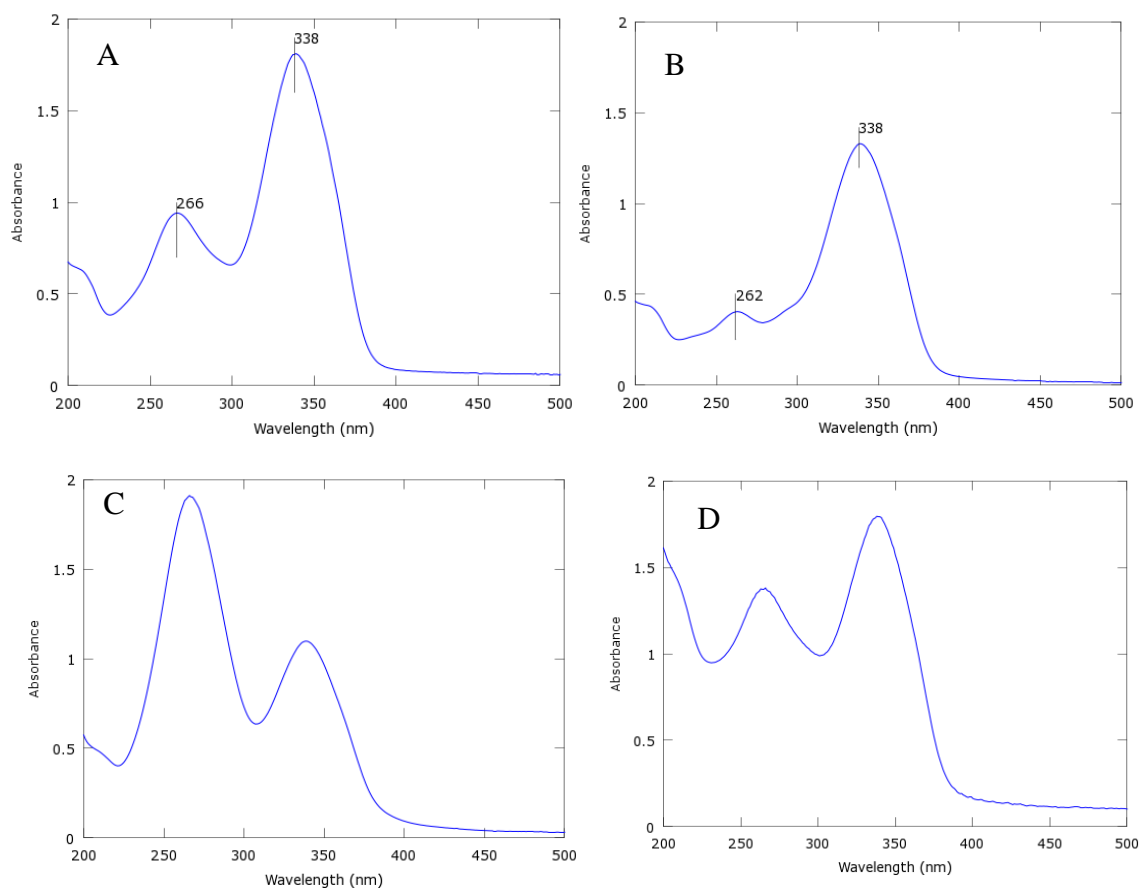


Figure S11 A-D. UV-Vis absorption spectra of co-precipitation nanoparticles [A] 16:84 [B] 20:80 [C] 30:70 [D] 40:60.

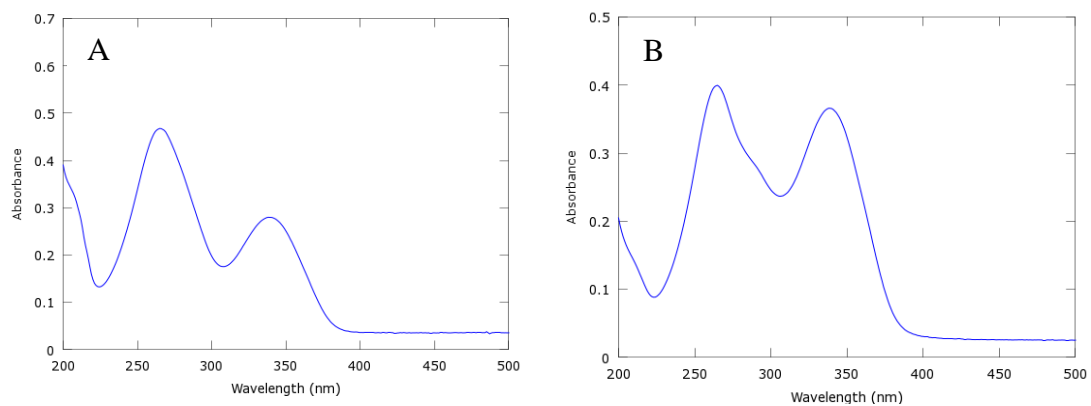


Figure S12 A-B. UV-Vis absorption spectra of high temperature nanoparticles [A] 16:84 [B] 40:60.

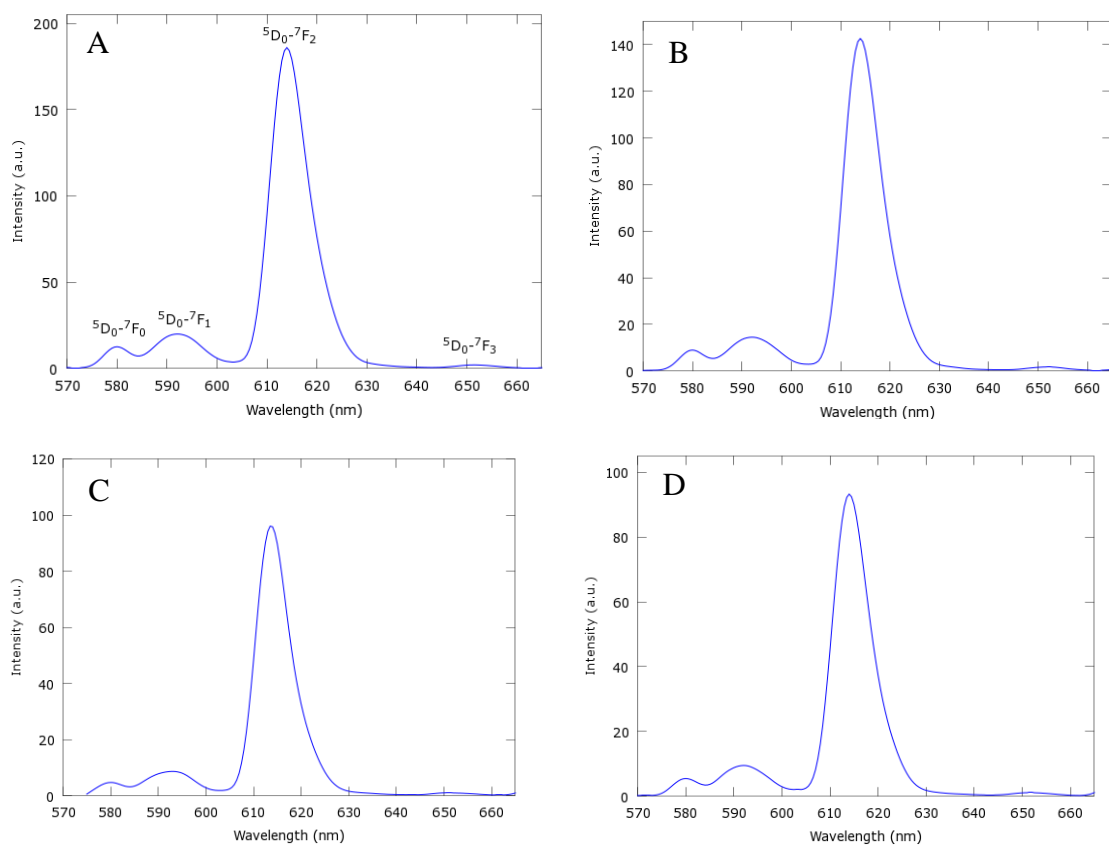


Figure S13 A-D. Luminescence spectra of co-precipitation nanoparticles [A] 40:60 [B] 30:70 [C] 20:80 [D] 16:84.